



**HAL**  
open science

# Design, fabrication and control of a microrobot for laser phonosurgery

Sergio Andrée Lescano

► **To cite this version:**

Sergio Andrée Lescano. Design, fabrication and control of a microrobot for laser phonosurgery. Automatic. Université de Franche-Comté, 2015. English. NNT : 2015BESA2002 . tel-01652112

**HAL Id: tel-01652112**

**<https://theses.hal.science/tel-01652112v1>**

Submitted on 29 Nov 2017

**HAL** is a multi-disciplinary open access archive for the deposit and dissemination of scientific research documents, whether they are published or not. The documents may come from teaching and research institutions in France or abroad, or from public or private research centers.

L'archive ouverte pluridisciplinaire **HAL**, est destinée au dépôt et à la diffusion de documents scientifiques de niveau recherche, publiés ou non, émanant des établissements d'enseignement et de recherche français ou étrangers, des laboratoires publics ou privés.



SPIM

Thèse de Doctorat



UFC

école doctorale **sciences pour l'ingénieur et microtechniques**  
UNIVERSITÉ DE FRANCHE-COMTÉ

# Design, Fabrication and Control of a Microrobot for Laser Phonomicrosurgery

■ SERGIO LESCANO

Thèse soutenue le 23/06/2015



# SPIM

## Thèse de Doctorat

UFC

école doctorale **sciences pour l'ingénieur et microtechniques**

UNIVERSITÉ DE FRANCHE-COMTÉ

N° X X X - X X X X - X

THÈSE présentée par

**SERGIO LESCANO**

pour obtenir le

Grade de Docteur de  
l'Université de Franche-Comté

Spécialité : **Automatique et Robotique**

## Design, Fabrication and Control of a Microrobot for Laser Phonomicrosurgery

Unité de Recherche :  
FEMTO-ST, UMR CNRS 6174

Soutenu le 23 June 2015 devant le Jury :

FRANÇOIS PIERROT	Rapporteur	Directeur de Recherche, CNRS, LIRMM, Montpellier
JÉRÔME SZEWCZYK	Rapporteur	Professeur, UPMC, Paris
JOCELYNE TROCCAZ	Examinatrice	Directrice de Recherche, CNRS, TIMC-IMAG, Grenoble
NICOLAS CHAILLET	Examineur	Professeur, UFC, Besançon
NICOLAS ANDREFF	Directeur de thèse	Professeur, UFC, Besançon
MICKY RAKOTONDRABE	Co-Directeur de thèse	Maître de Conférences HDR, UFC, Besançon





*To my loving mother Laura, for everything I am now.*



# Acknowledgements

Firstly, I would like to express my sincere gratitude to my thesis director Prof. Nicolas Andreff for the continuous support on my PhD study and related research, for his patience, motivation, and immense knowledge. His guidance helped me in all the time of research and writing of this thesis. I could no have imagined having a better advisor and mentor for my PhD study. In parallel I would like to thank to my co-director of thesis Assoc Prof. Micky Rakotondrabe for his enthusiasm and desire to put at the time od the experiments.

Beside my advisors, I would like to thank the rest of my thesis committee: Josseline Trocaz for presiding the jury evaluator pending the defense, Prof. Jerome Szewczyw and Prof. Francois Pierrot for report my manuscript, Prof. Nicolas Chaillet for his comments and remarks. All toughether for their insighful comments and encouragement, but also for the hard question which incented me to widen my research from various perspectives.

My sincere thanks also goes to Dr. Michael Gauthier, who is director of the departement AS2M, who gave access to the laboratory and research facilities.

I thank my fellow labmates in for the stimulating discussions and the time that we spend together: Naresh, Margot, Mouloud, Benoit, Bilal, Marcelo, Didace, Hussein, Nandish, Taha, Cyrine, Vincent's, Clement, Erwann, Ismael, Patrick's, Joel's, Soun, Ronald, Kamram, Juan A. E., Adrian, Mohamed, Guillaume's, Christopher, Brahim, Kanty, Tom, Cedric, etc. etc.

Last but not the least, I would like to thank my family in special my mother and my girlfriend for supporting me spiritually throughout this period developing and writing this thesis and my life in general.



# Contents

<b>Abstract</b>	<b>1</b>
<b>1 Introduction</b>	<b>3</b>
1.1 Context . . . . .	4
1.1.1 The larynx and vocal fold diseases . . . . .	4
1.1.2 Laser technologies in medical applications . . . . .	6
1.1.3 Laser phonomicrosurgery . . . . .	7
1.2 The $\mu$ RALP project . . . . .	8
1.2.1 Concept . . . . .	9
1.2.2 Design, fabrication and control of a microrobotic system . . . . .	10
1.3 This thesis . . . . .	11
1.3.1 Objectives and contributions of the thesis . . . . .	11
1.3.2 Specifications for the microrobot . . . . .	11
1.3.3 Outline of the thesis . . . . .	14
<b>2 State of the Art</b>	<b>17</b>
2.1 Introduction . . . . .	18
2.2 Medical robotics . . . . .	18
2.2.1 General aspects . . . . .	18
2.2.2 Robot-assited phonomicrosurgery . . . . .	21
2.3 Miniaturized positioning devices and their fabrication . . . . .	26
2.3.1 Microfabrication techniques . . . . .	26
2.3.2 Microplatforms and microsystems for precise positioning . . . . .	33
2.4 Actuators for high resolution positioning . . . . .	37
2.4.1 Thermomechanical Conversion . . . . .	38
2.4.2 Magnetomechanical Conversion . . . . .	39
2.4.3 Electromechanical Conversion . . . . .	40
2.4.4 Fluid Mechanic Conversion . . . . .	41
2.4.5 Multiple Conversion . . . . .	41
2.4.6 Summary on microactuators . . . . .	41

2.5	Compliant mechanisms . . . . .	43
2.6	Parallel Kinematic Mechanisms (PKM) . . . . .	44
2.6.1	Kinematics of robots . . . . .	46
2.6.2	Singularity analysis . . . . .	48
2.6.3	Performance evaluation . . . . .	49
2.6.4	Robot vision control . . . . .	50
2.7	Laser systems . . . . .	52
2.7.1	Definitions . . . . .	52
2.7.2	CO2 laser . . . . .	52
2.7.3	Thulium YAG laser . . . . .	53
2.7.4	Femto-second laser . . . . .	53
2.7.5	Safety and classes of lasers . . . . .	53
2.8	Synthesis and our proposition . . . . .	54
<b>3</b>	<b>Kinematic Analysis</b> . . . . .	<b>55</b>
3.1	Introduction . . . . .	56
3.2	Proposals for microrobot structure . . . . .	56
3.3	Theoretical background . . . . .	57
3.3.1	Screw Theory . . . . .	57
3.4	Modeling the Micro Agile-Eye . . . . .	62
3.4.1	Amplifier based on lever-principle . . . . .	62
3.4.2	Agile Eye: Spherical 2-DoF 5R PKM . . . . .	64
3.4.3	Docking mechanism . . . . .	66
3.4.4	Complete Micro Agile Eye . . . . .	67
3.5	Modeling the PiBot . . . . .	67
3.5.1	Inverse kinematics . . . . .	68
3.5.2	Instantaneous kinematics . . . . .	69
3.6	Optical model . . . . .	71
3.6.1	Basic background on reflective optics . . . . .	71
3.6.2	Kinematics . . . . .	74
3.6.3	Instantaneous Kinematics . . . . .	75
3.7	Conclusion . . . . .	76
<b>4</b>	<b>Fabrication</b> . . . . .	<b>77</b>
4.1	Introduction . . . . .	78
4.2	Proposed fabrication process . . . . .	78
4.2.1	Materials . . . . .	78
4.2.2	Process of fabrication . . . . .	78
4.2.3	Parallel robots and the SCM technique . . . . .	80
4.2.4	Important parameters for designing hinges in SCM . . . . .	81
4.3	Fabricated prototypes . . . . .	82
4.3.1	Fabrication of a single hinge . . . . .	82
4.3.2	Fabrication of the Micro Agile-Eye microrobot . . . . .	83
4.3.3	Fabrication of the PiBot microrobot . . . . .	88

4.4	Precision evaluation . . . . .	90
4.4.1	Interval analysis . . . . .	91
4.4.2	Spatial rigid motion tools . . . . .	93
4.4.3	Interval representation of uncertainties . . . . .	94
4.4.4	Transferring the uncertainties . . . . .	94
4.4.5	Methodology to evaluate uncertainties in parallel robots . . . . .	95
4.4.6	Implementation of the method on the proposed PiBot microrobot . . . . .	96
4.5	Conclusions . . . . .	101
<b>5</b>	<b>Control</b>	<b>103</b>
5.1	Introduction . . . . .	104
5.2	Classical visual servoing control . . . . .	104
5.2.1	Experimental setup . . . . .	105
5.2.2	Experimental results . . . . .	107
5.3	Feedforward compensation of vibrations and hysteresis . . . . .	110
5.3.1	General principle of feedforward control . . . . .	113
5.3.2	Experimental Setup: Interferometer . . . . .	120
5.3.3	Experimental results . . . . .	121
5.4	Visual servoing and feedforward compensation combined . . . . .	127
5.4.1	Experimental results . . . . .	127
5.4.2	Step response . . . . .	128
5.5	Conclusion . . . . .	133
<b>6</b>	<b>Conclusions and perspectives</b>	<b>135</b>
6.1	Conclusions . . . . .	135
6.2	Perspectives . . . . .	136
<b>A</b>	<b>Piezoelectric beams</b>	<b>139</b>
A.1	Introduction . . . . .	139
A.2	Piezoelectric materials . . . . .	139
A.2.1	Modeling piezoelectric actuators . . . . .	140
A.2.2	Piezoelectric cantilever actuators . . . . .	141
	<b>Bibliography</b>	<b>147</b>





# List of Figures

1.1	Localization of the larynx in the human body and its connection with the digestive and respiratory tracts. . . . .	4
1.2	Front and back view of the larynx. Vocal folds are shown as “V”-shaped structure. . . . .	4
1.3	Tools to diagnose and to treat diseases in the larynx cavity [151]. . . . .	5
1.4	Healthy vocal folds [177]. . . . .	6
1.5	Unhealthy vocal folds [177]. . . . .	6
1.6	Classical laser phonomicrosurgery being carried out by an experienced surgeon at the ORL Department of University of Genoa. . . . .	8
1.7	Concept of $\mu$ RALP. . . . .	9
1.8	Surgeon Tavernier drawing on a tactile tablet the laser path using the new concept of $\mu$ RALP. . . . .	10
1.9	Use of the microrobot to position/orient a micromirror to reflect the laser beams. . . . .	12
1.10	The two rotations ( $\theta_1$ and $\theta_2$ ) required to scan the entire vocal fold. . . . .	12
1.11	(a) The angle to be developed by the laser beam to scan the entire vocal folds. (b) Calculus of the scanning angle of the laser beam. The microrobot should rotate half this angle ( $\pm 12.5^\circ$ ) because any angle developed by the mirror is the half of the angle developed by the laser beam. (c) Calculus of the angle developed by the mirror. . . . .	13
1.12	Approximate calculation of the laser spot diameter based on a standard laser phonosurgery image provided by the CHRU of Besançon. . . . .	13
1.13	Principle scheme of the focus and optical system for the reflection of the laser beam onto the vocal folds. . . . .	14
2.1	Medical applications of robots. . . . .	19
2.2	Classification of surgical robots given by P. Dario [41]. . . . .	20
2.3	Systems proposed by Lumenis. . . . .	21
2.4	Use of the Da Vinci robot for transoral surgery using a gripper and a laser scalpel. . . . .	22
2.5	(a) Whole system holding the flexible endoscope. (b) Set of tools at the end of the endoscope. . . . .	23
2.6	(a) Distal tip of the endoscope. (b) Lenses and motors inside of the endoscope. . . . .	23
2.7	Endoscope using a femto-second laser. . . . .	24

2.8	Different fabrication processes of microdevices. . . . .	26
2.9	General schematic of the steps in a lithography process by using positive and negative resist (image from Henderson Research Group [64]). . . . .	27
2.10	General schematic of the doping process. . . . .	29
2.11	General schematic of the laser micromachining process using a laser beam focused on a point of the workpiece (image from [50]). . . . .	30
2.12	3D printing process (image from [2]). . . . .	31
2.13	Construction of four-bars and five-bar structures from links and flexure elements [157] by using SCM technology. . . . .	32
2.14	Example of Micro-Air-Vehicle (MAV) using SCM [186]. . . . .	32
2.15	Platform based on the electrothermal principle [188]. . . . .	34
2.16	Platform using electrothermal and piezoelectric actuators [193]. . . . .	34
2.17	Platform with high range and bandwidth but with a very high heating temperature [86]. . . . .	35
2.18	Platform with electrothermal actuation [146]. . . . .	36
2.19	Platform actuated by comb-drive electrostatic (capacitive) actuators [51]. . . . .	36
2.20	Platform with electrostatic actuation [100]. . . . .	37
2.21	Actuators Classification . . . . .	39
2.22	Compliant mechanical part. . . . .	44
2.23	(a) Flexure hinge manufacture with SCM technology. (b) Flexure hinge with rotation about the x-axis. . . . .	44
2.24	A 6 DoF parallel robot [136]. . . . .	45
2.25	Challenging research issues in PKMs . . . . .	46
2.26	Two fundamental configurations based on the relative localization of the camera and the robot end-effector. . . . .	50
2.27	Model-based Cartesian control of parallel robots. . . . .	51
2.28	Vision based control of parallel robots. . . . .	52
3.1	Proposed microrobots placed at the head of the adjustable laryngoscope driving a laser beam. (a) Micro Agile-Eye: a microrobot using amplification system made of three cantilevers per leg and a standard kinematic structure. (b) PiBot: a microrobot using a unique piezoelectric cantilever per leg and amplification made by appropriate connection onto the platform. . . . .	57
3.2	A Screw. . . . .	58
3.3	Reciprocal product of two screws. . . . .	59
3.4	(a) Revolute joint and its twist and wrenches. (b) Prismatic joint and its twist and wrenches. . . . .	61
3.5	(a) A Serial Kinematic Chain. (b) A Parallel Kinematic Chain. . . . .	62
3.6	Kinematic representation of the piezoelectric cantilever actuators and amplification mechanisms by lever effect of the two active legs in the PKM. . . . .	63
3.7	The system without actuation is shown in black while in red the system is shown after actuation. . . . .	63
3.8	Kinematic representation of the Agile Eye 2-DoF [63]. . . . .	65
3.9	Micro Agile Eye complete. . . . .	67

3.10	Platform operated in parallel by two active legs and constrained by an unactuated U-joint leg. . . . .	68
3.11	Laser beam trajectory reflected by a planar mirror. . . . .	72
3.12	Snell law. . . . .	73
3.13	Optical triangle. . . . .	74
4.1	Parts of a flexure hinge which results from the SCM fabrication technique. . . .	79
4.2	Process of fabrication of single flexible joints. . . . .	79
4.3	Main parameters for designing hinges in SCM. (a) Unfolded hinge where the gap $e$ is the space between the two links, $L_{cf}$ is the thickness of the carbon fiber. (b) Folded hinge where the maximum reachable $\theta$ angle is in accordance with $e$ and $L_{cf}$ . . . . .	82
4.4	Pseudocolored SEM image depicting the carbon fiber along with the flexible polyimide. . . . .	83
4.5	Amplifier system. . . . .	83
4.6	Fabrication result of the amplifier system. (a) Flexible elements which are a constituent part of the joints in the mechanical amplifier. (b) A flexible element and a piezoelectric cantilever actuators before they are assembled. (c) Support and elements before they are assembled. (d) Piezoelectric cantilever actuators assembled with the flexible elements. . . . .	84
4.7	(a) Amplifier mechanism assembled with its electrical connections. (b) Other view of the amplifier system compared with one cent euro coin. . . . .	85
4.8	(a) CAD design of the orientable platform before the folding process. (b) Other view of the structure. . . . .	85
4.9	Fabricated orientable platform in 2D. . . . .	86
4.10	(a) CAD design of the assembled microrobot. (b) A micromirror layer device is placed on the platform. (c) CAD design of the complete assembled microrobot including its support. (d) Other view of the microrobot Micro Agile-Eye. . . . .	87
4.11	(a) Fabricated and assembled Micro Agile-Eye microrobot. (b) Other view of the Micro Agile-Eye. . . . .	88
4.12	CAD design of the planar stage of the PiBot. . . . .	88
4.13	Realization of the planar structure corresponding to the PiBot. . . . .	89
4.14	CAD design of the folded structure. . . . .	89
4.15	Realization of the PiBot compared with one cent euro coin. . . . .	90
4.16	(a) A hinge based on the flexibility of a polyimide material. (b) Sprained kink dislocating the position and the direction of the rotation axis in position and direction. . . . .	90
4.17	Two links and a flexible hinge at B with uncertainties due to the SCM fabrication technique. . . . .	94
4.18	Result of the components of (4.24) by SIVIA algorithm (a) of the first component. (b) of the second component. (c) of the third component. . . . .	99
4.19	Outcome of the intersection of all the three solutions shown above. . . . .	100
4.20	Algorithm performed to several angles (A) $(\theta_1, \theta_2) = (15^\circ, 15^\circ)$ (B) $(\theta_1, \theta_2) = (-15^\circ, 15^\circ)$ (C) $(\theta_1, \theta_2) = (-15^\circ, -15^\circ)$ (D) $(\theta_1, \theta_2) = (0^\circ, 0^\circ)$ . . . . .	101

5.1	Control using visual feedback. . . . .	105
5.2	Experimental setup. . . . .	106
5.3	Step response of the controlled microrobot along the $x$ -axis. . . . .	107
5.4	Step response of the controlled microrobot along the $y$ -axis. . . . .	108
5.5	Complex trajectory tracking using visual servoing. . . . .	109
5.6	Hysteresis of the controlled microrobot using visual servoing. . . . .	110
5.7	Hysteresis obtained from a piezoelectric cantilever actuator from [145]. . . . .	111
5.8	Creep obtained from a piezoelectric cantilever actuator from [145]. . . . .	112
5.9	Oscillation obtained when applying a step excitation to a piezoelectric cantilever actuator from [145]. . . . .	112
5.10	Feedforward control of one actuated leg of the micro-robot. . . . .	113
5.11	Vibration compensation methods. . . . .	114
5.12	Two impulses applied to a badly damped system. . . . .	115
5.13	Block diagram of the Zero-Vibration-Input-Shaping technique. . . . .	115
5.14	Complete block diagram of the Zero-Vibration-Input-Shaping with “ $m$ ” impulses. . . . .	116
5.15	Hysteresis models. . . . .	117
5.16	Block diagram of a feedforward control to cancel the hysteresis behavior. . . . .	118
5.17	Generalized Bouc-Wen hysteresis compensator. . . . .	119
5.18	Compensation of vibration and hysteresis of a robot leg. . . . .	119
5.19	Interferometer for the measurement of the displacement of each leg of the microrobot. . . . .	120
5.20	Diagram of the experimental setup for the characterization of fast dynamics of the microrobot legs. . . . .	121
5.21	Feedforward compensation of badly damped oscillation in the left leg. . . . .	122
5.22	Feedforward compensation of badly damped oscillations in the right leg. . . . .	124
5.23	Feedforward compensation of the hysteresis of the system composed by the vibrations compensator and the left leg. . . . .	125
5.24	Feedforward compensation of the hysteresis of the system composed by the vibrations compensator and the right leg. . . . .	126
5.25	Diagram of the classical visual servoing and the feedforward control combined. . . . .	127
5.26	Step response along $x$ -axis of the system controlled by visual servoing and feedforward techniques combined. . . . .	128
5.27	Step response along $y$ -axis of the system controlled by visual servoing and feedforward techniques combined. . . . .	129
5.28	Complex trajectory tracking using visual servoing coupled with feedforward compensation. . . . .	130
5.29	Hysteresis of the controlled microrobot using visual servoing coupled with feedforward compensation. . . . .	132
A.1	Interaction processes between the electrical, mechanical and thermal systems [80]. . . . .	140
A.2	Piezoelectric Structures: (A) two-layers unimorph, (B) two-layer bimorph, (C) three-layer bimorph. . . . .	141
A.3	A two-layers bimorph piezoelectric cantilever with parallel polarization. . . . .	142
A.4	A two-layers bimorph piezoelectric cantilever with anti-parallel polarization. . . . .	142

# List of Tables

- 2.1 Medical devices for vocal folds treatment. . . . . 25
- 2.2 Comparison of microactuators. . . . . 42
  
- 4.1 Conventional joints and their equivalences made with SCM process. . . . . 81
- 4.2 The SIVIA algorithm [93]. . . . . 93
  
- 5.1 Table of errors . . . . . 131
  
- A.1 Solution for the characteristic equation of A.7 . . . . . 143



# Abstract

This thesis reports the design, fabrication and control of a parallel microrobot with two degrees of freedom in rotation, that is destined to perform laser microsurgery on vocal folds. This work has been developed in the frame and in the context of the European project Micro-Technologies and Systems for Robot-Assisted Laser Phonomicrosurgery entitled  $\mu$ RALP.

On the one hand, needs and limits of medical aspects have been abstracted to create the microrobot specifications. On the other hand, the state-of-the-art has identified the technological stumbling blocks and has allowed to led to our proposition to satisfy the specifications. This work has envisaged the fabrication of two independent parallel microrobotic structures. Each proposed microrobot has a different kinematic structure, however they have the same objective that is to guide a laser beam onto the vocal folds. To this purpose, a mirror is placed on the end-effector of both microrobots in order to reflect and guide the laser beam. Smart Composite Microstructures fabrication technique was used to fabricate the two microrobots. Moreover, piezoelectric cantilever actuators have been used to generate the required rotations. Finally, the expected precision for laser microsurgery of the vocal folds was reached by coupling the feedforward compensation of nonlinearities and vibrations of the actuators with visual feedback control of the parallel kinematic mechanism.





# Introduction

*This chapter describes the context in which this thesis lies. First, a brief anatomic description of the larynx and the vocal folds is detailed as well as their localization in the human body and their functions. Then, a general description of phonomicrosurgery along with a procedure to improve human voice via a delicate action on the vocal folds are presented. Afterwards, laser technologies and their utilization in medical procedures are outlined. A section is dedicated to the description of the  $\mu$ RALP project, in particular regarding the workpackage dedicated to this thesis. Finally, objectives, contributions, specifications and an overview of the thesis are outlined.*

## Chapter contents

---

<b>1.1</b>	<b>Context</b> . . . . .	<b>4</b>
1.1.1	The larynx and vocal fold diseases . . . . .	4
1.1.2	Laser technologies in medical applications . . . . .	6
1.1.3	Laser phonomicrosurgery . . . . .	7
<b>1.2</b>	<b>The <math>\mu</math>RALP project</b> . . . . .	<b>8</b>
1.2.1	Concept . . . . .	9
1.2.2	Design, fabrication and control of a microrobotic system . . . . .	10
<b>1.3</b>	<b>This thesis</b> . . . . .	<b>11</b>
1.3.1	Objectives and contributions of the thesis . . . . .	11
1.3.2	Specifications for the microrobot . . . . .	11
1.3.3	Outline of the thesis . . . . .	14

---

## 1.1 Context

### 1.1.1 The larynx and vocal fold diseases

The larynx is positioned in the anterior neck, below the division point between respiratory and digestive tracts, as shown in Figure 1.1. The vocal folds are an integral part of the larynx, located at the center of the larynx framework in an anterior-posterior orientation, as shown in Figure 1.2. When viewed from above, the right and left folds appear as a “V”-shaped structure with the aperture between the “V” forming the entrance to the respiratory tract (called “trachea”), as shown in Figure 1.2. Vocal folds are suspended at the entrance of the respiratory tract, attached to a small arytenoid cartilage on the back side of the larynx [57].

In normal function of the larynx, its muscles contract or relax during the various stages of breathing, swallowing, and speaking. Thus, deglutition, respiration and phonation process are involved with the larynx. As a result of its multi-functional nature, the larynx is exposed to a broad spectrum of disorders. Disorders of the larynx can result in interference of any or all of the associated processes. Thus, a vast array of surgical interventions and methods are devoted to heal these disorders.

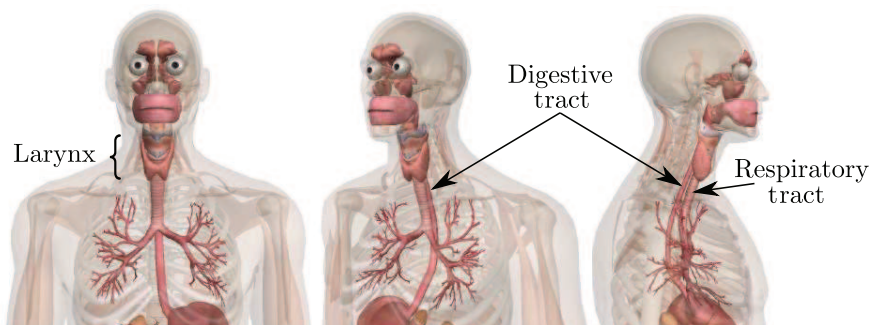


FIGURE 1.1: Localization of the larynx in the human body and its connection with the digestive and respiratory tracts.

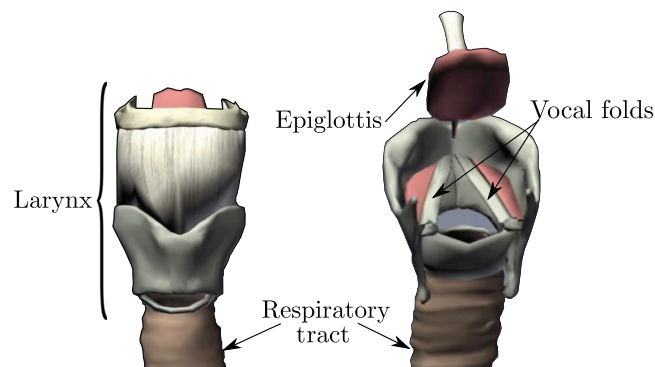


FIGURE 1.2: Front and back view of the larynx. Vocal folds are shown as “V”-shaped structure.

The term “*phonosurgery*” was coined in the early 1960s. Phonosurgery is defined as: “all the surgical procedures that maintain, restore, or enhance the human voice”. Or again “the science of manipulating the vibratory elements of the larynx in order to restore voice function” [71]. Phonosurgery includes:

- *laryngoplastic* phonosurgery, which is an open-neck surgery that restructures the cartilaginous framework of the larynx and the soft tissues,
- *laryngeal injection*, that involve the injection of medication as well as of synthetic and organic biologic substances into the larynx,
- *reinnervation of the larynx*, which consists in restoring the nerve supply,
- and *phonomicrosurgery*, which is a microsurgery of the vocal folds.

Notice that microsurgery is a surgery that is performed on very small structures, such as blood vessels and nerves, with specialized instruments under a microscope [171]. Regarding the phonomicrosurgery, there are two main tools used to diagnose and to treat the vocal folds: endoscopes and laryngoscopes. On the one hand, endoscopes, usually flexible, are used to inspect the larynx with tiny cameras placed at their end, as shown in Fig. 1.3a. On the other hand, laryngoscopes which are rigid, as shown in Fig. 1.3b, are used to insert other tools like scalpels, grippers and allow to place microscopes, out of the patient’s body, focusing on the vocal folds. However, the obtained images with laryngoscopes do not show the entire vocal folds as is the case with endoscopes.

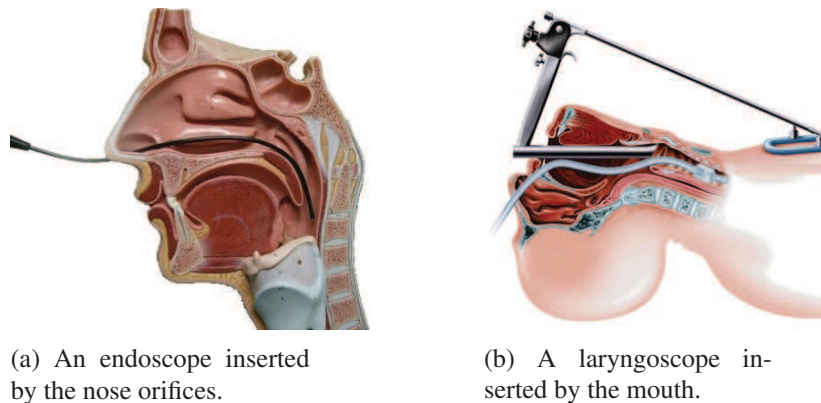


FIGURE 1.3: Tools to diagnose and to treat diseases in the larynx cavity [151].

Figure 1.4 and Figure 1.5 show healthy and unhealthy vocal folds, respectively. Pictures in Figure 1.4a and Figure 1.5a were taken with a camera at the extremity of an endoscope. These images were taken very near to the vocal folds and clearly show 100% of them. In Figure 1.4b and Figure 1.5b only a part of the vocal folds can be observed. Those images were taken using a laryngoscope with a microscope located at the exterior of the human body.

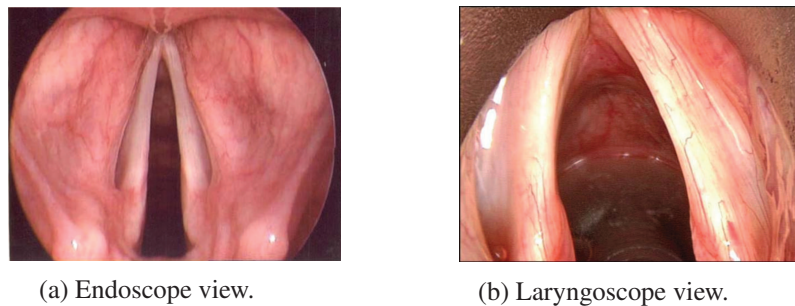


FIGURE 1.4: Healthy vocal folds [177].

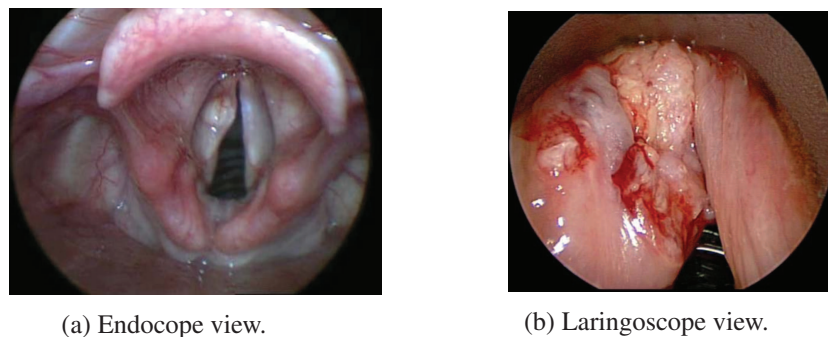


FIGURE 1.5: Unhealthy vocal folds [177].

Structural abnormalities of the vocal fold include a wide spectrum of pathologies such as nodules, polyps, cysts, and cancer. An unhealthy vocal fold with a benign vocal fold cyst and another one with a cancerous lesion of the vocal fold are shown in Figure 1.5a and Figure 1.5b respectively.

### 1.1.2 Laser technologies in medical applications

Since the invention of the first visible laser light based upon a ruby crystal [53] by Theodore Maiman in 1960, variations of this technology have been adapted to engineering and medical applications.

The use of laser in medicine has developed along with other technologies and techniques like automatic control [159], robotics [167], optics [172]; covering many application areas. Surgical lasers are employed to cut and/or to ablate tissue. Each kind of laser has a varying degree of coagulation and clean cutting performances. The principal types of lasers in medical applications are quickly reminded below.

- a) **Nd:YAG** (Neodymium-doped: Yttrium Aluminum Garnet) laser is employed in tissue cutting and ablative applications.
- b) **Tm:YAG** (Thulium-doped: Yttrium Aluminum Garnet) laser is efficient for superficial ablation of tissue, with minimal coagulation depth in air or in water.

- c) **Argon** laser is better accommodated for tissue coagulation.
- d) **CO<sub>2</sub>** laser is better suited for both tissue cutting/ablative and tissue coagulation.

Nowadays, these surgical lasers are used in many areas of medicine. Some of the widespread medical applications of lasers are described below according to the specialization.

- a) **Dermatology:** this is the area in which the laser was first used for medical application. In 1962 the dermatologist Leon Goldman used laser technology to rub out an unwanted tattoo [175].
- b) **Ophthalmology:** lasers are used in a variety of treatments in ophthalmology. The classical system uses a laser source coupled with a microscope [111].
- c) **Gynecology:** application of laser in gynecology has began in 1979. The typical system employs laparoscopy instruments controlling the laser source from the exterior of the patient's body [124].
- d) **Laryngology:** laser technologies have been used with laryngoscopes to treat diseases in the laryngeal cavity. Significant applications have been found within the phonomicrosurgery, as described in next Section.

### 1.1.3 Laser phonomicrosurgery

Phonomicrosurgery describes a set of medical procedures used to treat abnormalities on the vibratory elements of the vocal folds in order to restore or to improve voice function. It involves the excision of tissue mass which could be a benign mass or a cancerous lesion. In laser phonomicrosurgery the utilization of scalpel is being replaced by the use of laser technologies.

Phonomicrosurgery with laser as scalpel was introduced by Jako [90, 91] in the 1970's. Since then, a number of different laser technologies have been customized and employed in phonomicrosurgeries: CO<sub>2</sub>, Thulium-doped: Yttrium Aluminum Garnet (Tm:YAG) and Neodymium-doped: Yttrium Aluminum Garnet (Nd:YAG). Currently, within phonomicrosurgery, laser applications are mainly either ablation or cutting techniques. Examples of vocal fold abnormalities treated with laser include vascular abnormalities, epithelial lesions, cysts, cancers, etc. [57], as shown in Figure 1.5.

Even though there exists a variety of laser technologies, the prevalent traditional methodology for remote control of the surgical laser is mechanical manipulator [57]<sup>1</sup>. This mechanical manipulator as well as the laser source are located at about 400mm from the vocal folds, as shown in Figure 1.6. However, many of the difficulties associated in using this classical mechanical manipulator are rooted in the ergonomics of the device. As a result, the clinician has no convenient way of steadying his/her hand while making precise and delicate movements necessary to accurately and consistently aim the surgical laser. Thus, there is a considerable high risk to burn healthy tissues. Furthermore, there are parts of the vocal folds that are not reachable

---

<sup>1</sup>Note that laser-based Tm-YAG lasers were introduced recently on the market [107], which allow to bring manually the laser in contact with the vocal folds. However, this technique, being manual, does not guarantee accuracy of the surgery.

due to the fact that the laser source is placed out of the patient's body and that the narrow space that the laser beam should pass through the laryngoscope is very limited. Additionally, due to the extreme neck extension of the patient during the surgery, side effects (like neck pain) may appear and stay for a couple of days.

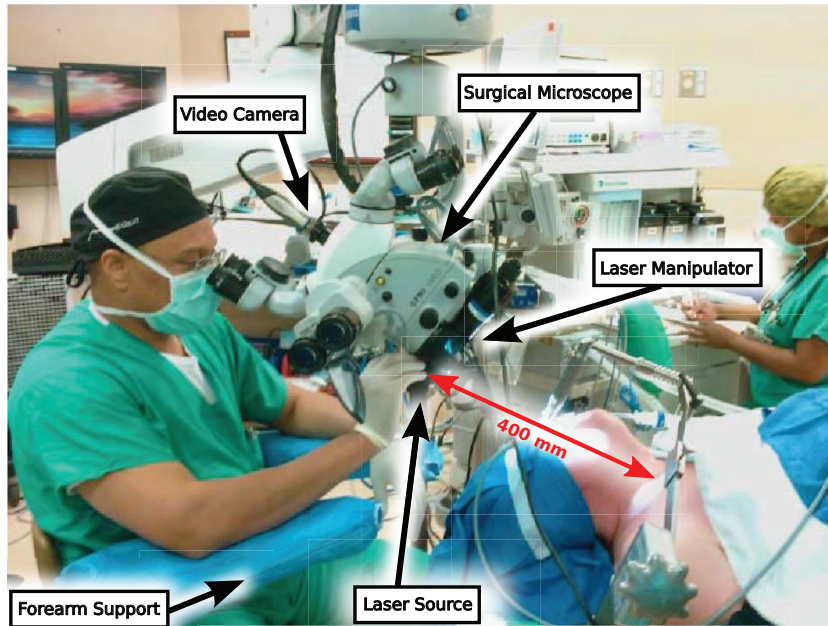


FIGURE 1.6: Classical laser phonomicrosurgery being carried out by an experienced surgeon at the ORL Department of University of Genoa.

## 1.2 The $\mu$ RALP project

The  $\mu$ RALP project was a three-year (2012-2015) Specific Targeted Research Project (STReP) project funded under the European Commission 7th Framework Programme. The consortium of  $\mu$ RALP was composed of five institutions from three different European countries: France, Italy and Germany. There are three technical partners, each one consecrated to build one functional part within the project. They are:

- the Franche-Comté **E**lectronique **M**écanique **T**hermique et **O**ptique - **S**ciences et **T**echnologies (FEMTO-ST) Institute which is a public research laboratory affiliated with the French National Centre of Scientific Research (CNRS), the University of Franche-Comté (UFC), the National School of Mechanical Engineering and Microtechnology (ENSMM), and the Belfort-Montbéliard University of Technology (UTBM),
- the Istituto Italiano di Tecnologia (IIT) in Genoa,
- and the Leibniz Universität Hannover (LUH).



The project also involved two hospitals that were directly in charge of the medical and clinical information as well as with the facilities to the preclinical trials in cadavers. They are:

- the Centre Hospitalier Régional Universitaire (CHRU) in Besançon,
- and the Otorhinolaryngology Department of the University of Genoa (UNIGE).

### 1.2.1 Concept

The  $\mu$ RALP project focused on advancing the state of the art in laser phonosurgery, which currently relies completely on the dexterity of surgeons who must operate through a microscope, control the laser directly by hand, and deal with the associated poor ergonomics of the operating setup.

This project has gone beyond the contemporary experimental systems, which have limited application range due to the dependency on an external microscope with direct line of sight to the operating area. This progress relative to the existing technology was possible thanks to the creation of a teleoperated surgical system based on a **microrobot as an end-effector** and an adjustable laryngoscope to insert the microrobot and cameras inside of the patient's body, eliminating the need for the surgical microscope and its associated requirement for direct line of sight to the vocal folds, as shown in Figure 1.7. This new system provides better accessibility and precision to laser microsurgeries than current systems.

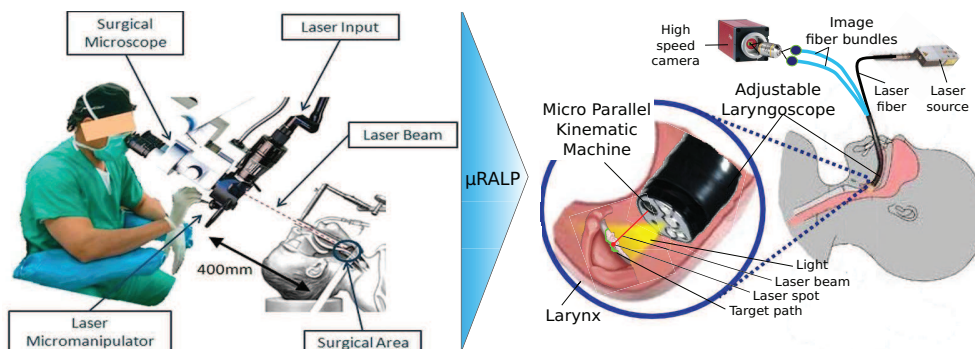


FIGURE 1.7: Concept of  $\mu$ RALP.

The central idea of the project was (and remains) to augment the surgeon's dexterity, manipulation skills and efficiency through advanced surgeon-robot interfaces, sensors, actuators and supervisory safety. Contributions of  $\mu$ RALP are:

- a) design, fabrication and control of a set of solutions to steer the laser,
- b) vision-based control of the laser,
- c) close installation of cameras near the vocal folds for: surgeon stereo-vision, auto-fluorescence imaging and vision-based control,
- d) design and fabrication of a flexible laryngoscope to relieve the neck,



- e) creation of a intuitive surgeon-robot interface, as shown in Figure 1.8,
- f) and cadaver trials,



FIGURE 1.8: Surgeon Tavernier drawing on a tactile tablet the laser path using the new concept of  $\mu$ RALP.

### 1.2.2 Design, fabrication and control of a microrobotic system

The aim here consisted in developing a new microrobot able to precisely orient the laser beam. A parallel structure was proposed for the microrobot mainly due to the offered accuracy and rapidity and also because of the safety and mechanical robustness. Its end-effector (or, rather, its mobile platform) must orient and actuate a micromirror to reflect the laser beam. The actuation of the microrobot was chosen to be based on smart materials locally embedded instead of deported DC-motors and traditional hinges in order to minimize mechanical clearances and therefore to minimize imprecision risk. Another advantage is the theoretically infinite resolution that smart materials can offer. It was expected that piezoelectric materials would be combined with silicon material because of the batch fabrication possible with the latter.

To improve the performance of the micromechatronic system, i.e. of the microrobot, a feedback control was planned to be further implemented. Standard mechatronic design would require the addition of sensors to the microrobot. However, a sensor that can provide the required submicrometric accuracy, several hundred Hertz of bandwidth, and at the same time packageable for the expected device does not currently exist. To overcome this limitation, this task also investigates the use of a high-speed visual feedback for the low-level microrobot controller. A particular challenge for that is the acquisition of information from the interaction of the laser with the environment (3D information) and its use as feedback for the microrobot control [173, 7].

To summarize, the objective is to obtain a precise platform orientation according to a reference orientation provided by a higher level supervision.

## 1.3 This thesis

The thesis deals with the design, development, modeling and control of the microrobot devoted to orient the laser beam over the whole vocal folds. The microrobot was designed to be placed at the end (distal-tip) of an adjustable laryngoscope. The microrobot dimensions must fit with the space available in the human larynx and with the space assigned in the laryngoscope. The specifications used for the design of the microrobot which were given in the early stage of the project are described below.

### 1.3.1 Objectives and contributions of the thesis

The objectives of this thesis were:

- design of one micro parallel structure to perform laser steering onto vocal folds,
- fabrication of the designed micromechanism,
- derivation of the control-oriented model(s),
- accurate control,
- and integration in the adjustable laryngoscope.

All these objectives (save the integration) were reached with no one but two micromechanisms, as will be described in this document. Before proceeding to the development of these contributions, let us remind the specifications of the microrobot.

### 1.3.2 Specifications for the microrobot

The initial specifications used to design the microrobot were the result of many discussions between the different partners of the project.

The design of the microrobot must be independent from the choice of the laser technologies used (CO<sub>2</sub>, Thulium, etc). For that, reflective optics (utilization of mirrors) was chosen, instead of diffractive optics (utilization of lenses). Another reason for this wavelength-independent design is that, contrary to lenses, it allows to easily collimate a visible aiming laser with the invisible surgical laser. Optical fibers must bring the laser beam from the external source to the laryngoscope tip, in front of the vocal folds. The microrobot will reflect and orient the laser beam towards the part to be treated, as shown in Figure 1.9.

**Number of degrees of freedom (DoF)-** To scan the entire vocal fold surface with the surgical laser, a microrobot that has at least 2-DoF (orientation about the  $x$  – axis and about the  $y$  – axis,  $z$  being the laser beam axis) is required as shown in Figure 1.10.

**Working distance-** The space between the end surface of the laryngoscope head and the vocal folds is approximatively 20 mm, as depicted in Figure 1.11a. This is a trade-off between the resolution and the microrobot range of motion (both increase as the distance to the vocal folds shrinks).

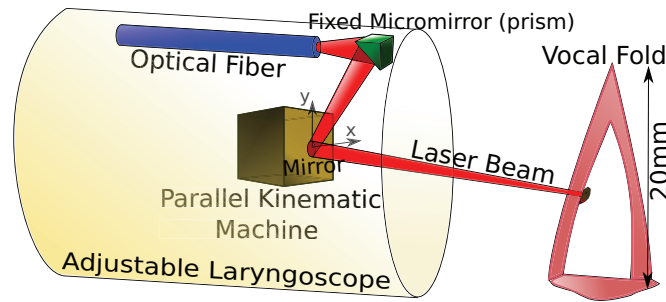


FIGURE 1.9: Use of the microrobot to position/orient a micromirror to reflect the laser beams.

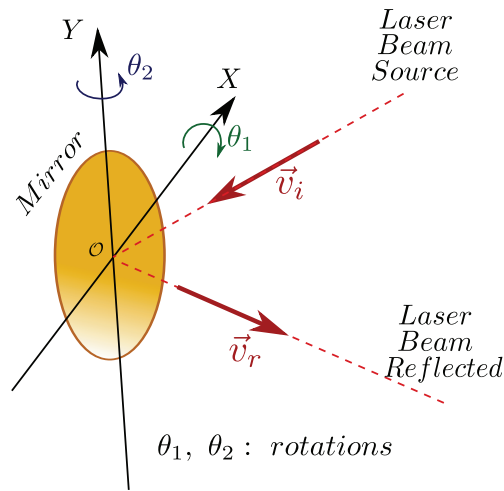


FIGURE 1.10: The two rotations ( $\theta_1$  and  $\theta_2$ ) required to scan the entire vocal fold.

**Range of orientation-** Based on the distance between the head of the flexible laryngoscope and the vocal folds, i.e., 20 mm, it is calculated that the minimal range to be developed by the laser beam is of  $\pm 25^\circ$  for each axis in order to cover their entire surface (roughly a circle of 20 mm diameter), as shown in Figure 1.11b. This corresponds to an angle range of  $\pm 12.5^\circ$  for each axis of the mirror orientation, as shown in Figure 1.11c.

**Scanning resolution-** The scanning resolution of the laser onto the vocal fold should be better than  $100 \mu\text{m}$ . This is equivalent to approx.  $0.15^\circ$  of resolution in each rotation angle of the micromirror at the reference 20 mm of distance.

**Biocompatibility-** As the flexible laryngoscope and the head which encloses the microrobot are aimed to work in-vivo spaces, the device should use biocompatible materials or sheltered to ensure that it does not come in contact with the human tissues.

**Bandwidth-** The bandwidth is defined as the first modal frequency. A calculation (made by the Italian team), based on the laser power, yields that a minimal bandwidth of 200Hz

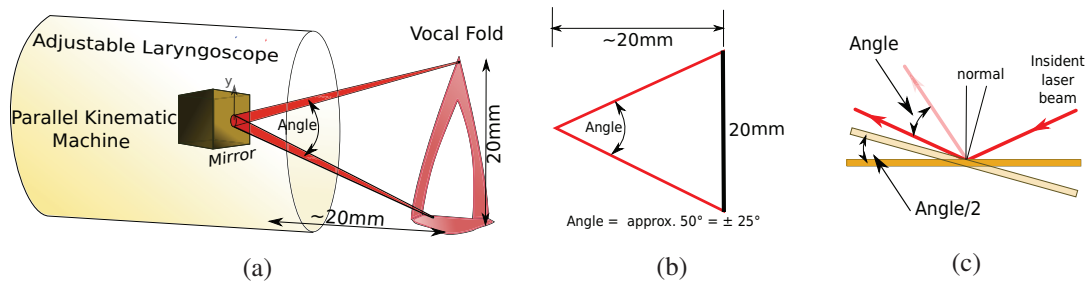


FIGURE 1.11: (a) The angle to be developed by the laser beam to scan the entire vocal folds. (b) Calculus of the scanning angle of the laser beam. The microrobot should rotate half this angle ( $\pm 12.5^\circ$ ) because any angle developed by the mirror is the half of the angle developed by the laser beam. (c) Calculus of the angle developed by the mirror.

from the microrobot is necessary to ensure a safety during the laser surgery. Indeed, if the platform is not fast enough, the laser may damage healthy tissues of vocal folds and its surrounding.

**Focus system-** To permit a good detection of the laser spot by the cameras and to permit a good resolution of it on the vocal folds, its specified diameter was  $200\ \mu\text{m}$  in accordance with the surgical image realized at the CHRU Besançon with the Aclublade system, as shown in Figure 1.12. That value was confirmed by comparison with the Aclublade datasheet ( $150\ \mu\text{m}$ ) and with the  $300\ \mu\text{m}$  achieved in [133]. To that purpose a system (focus system) using a prism and a plane mirror, as shown in Figure 1.13, was proposed.

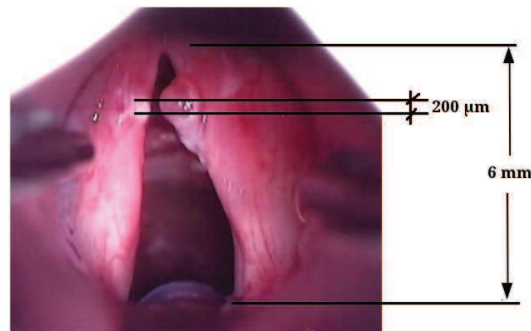


FIGURE 1.12: Approximate calculation of the laser spot diameter based on a standard laser phonosurgery image provided by the CHRU of Besançon.

**Size of the microrobot-** The negotiations with LUH in charge of packaging many components (cameras, light, tool channel, microrobot) in a limited diameter, yielded that the platform should be enclosed in a cube less than  $10 \times 10 \times 10\ \text{mm}^3$ .

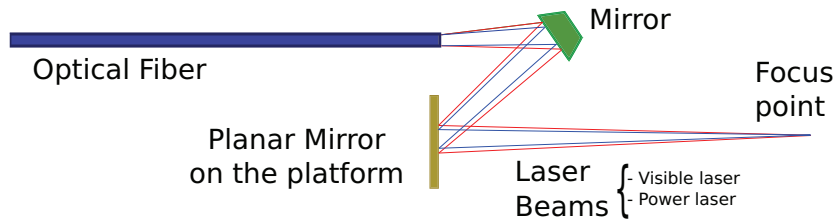


FIGURE 1.13: Principle scheme of the focus and optical system for the reflection of the laser beam onto the vocal folds.

In summary, the specifications of the microrobot are:

- i) 2-DoF (rotations about x-axis and y-axis),
- ii) a minimal scanning angle of  $\pm 12.5^\circ$ ,
- iii) a maximal space assigned within a cube of  $10 \times 10 \times 10 \text{ mm}^3$ ,
- iv) a minimal bandwidth of 200 Hz,
- v) and a scanning resolution<sup>2</sup> better than  $100 \mu\text{m}$ .

Remind that it was decided that a parallel structure would be used for the platform. Also the actuation of the microrobot must be based on smart materials locally embedded instead of deported DC-motors, conventional hinges and/or cables. Such a technique minimizes the mechanical clearances and therefore minimizes the loss of resolution and precision.

In this thesis two different microrobots are proposed. These two microrobots have different kinematic structures. Though, they are destined to accomplish the same specifications.

### 1.3.3 Outline of the thesis

The structure of the thesis is as follows:

**CHAPTER 2** gives the state-of-the-art of topics related to different domains involved in the design and development of the microrobot. They include *medical robotics*, *microdevices*, *microfabrication techniques*, *actuators* compatible with microfabrication, *parallel structures* and *laser technologies*. Finally, our proposition based on the state-of-the-art and the specifications of the project is outlined.

**CHAPTER 3** presents the kinematic structures of the two proposed microrobots: i) Micro Agile-Eye which is based on a conventional kinematic structure, ii) and PiBot which is a new parallel kinematic mechanism. Kinematic modeling is developed and screw theory is used for that. Moreover, an analysis of the singularities is also made in this chapter. Finally, an analysis

<sup>2</sup>By scanning resolution, we mean the diameter of the laser spot on the vocal fold.

of the laser beam kinematics is done. Contribution of this chapter deals mainly with: i) the proposition of two concepts to obtain microrobots with large amplitudes and high bandwidth and ii) the introduction of a new parallel kinematic mechanism (PiBot).

**CHAPTER 4** deals with the proposed fabrication process which is used for the first time to fabricate microrobots with parallel structure. The materials used and the microfabrication procedures are presented for that. Results are shown for the two proposed parallel structures. Then the analysis of the precision achieved with the structures proposed is performed using Interval Analysis. Contributions of this chapter are: i) fabrication of micro parallel kinematic mechanisms with a recent fabrication technique, ii) and the model of uncertainties due to the fabrication method using exponential representation of a homogeneous transformation in a parallel structure.

**CHAPTER 5** presents the last contribution of this thesis, namely the coupling of feedforward compensation of the nonlinearities and vibrations exhibited by the piezoelectric cantilever actuators with visual feedback of the parallel kinematic mechanisms. Thus, in this chapter two main control schemes are proposed: i) a control scheme for a microrobot parallel using visual servoing, ii) and a control scheme which combines classical visual servoing feedback with feedforward compensation. For that, a full characterization, modeling and compensation procedure of these phenomena is proposed.

Lastly, conclusions are given in **CHAPTER 6**. A brief discussion on scientific and technical perspectives is also laid out.



# Chapter 2

## State of the Art

*This chapter deals with the current state-of-the-art of the several topics which are related to our work in this thesis. Firstly, a survey of medical robotics is given, with a reminder of the position of our work relative to them. The second part deals with microdevices, where we quickly survey microplatforms and microfabrication techniques. Further, a survey and a comparison of actuators destined to high resolution positioning is given. Subsequently, a brief explanation on compliant mechanisms is provided. Later, a survey on parallel robots is proposed in relation to the micro-robotics issues. Afterwards laser technologies are detailed. Finally we conclude the chapter with our proposition regarding a novel 2-DoF microrobot, with high scanning resolution, high range, high bandwidth and high compactness devoted to phonomicrosurgery tasks.*

### Chapter contents

---

<b>2.1</b>	<b>Introduction</b>	<b>18</b>
<b>2.2</b>	<b>Medical robotics</b>	<b>18</b>
2.2.1	General aspects	18
2.2.2	Robot-assited phonomicrosurgery	21
<b>2.3</b>	<b>Miniaturized positioning devices and their fabrication</b>	<b>26</b>
2.3.1	Microfabrication techniques	26
2.3.2	Microplatforms and microsystems for precise positioning	33
<b>2.4</b>	<b>Actuators for high resolution positioning</b>	<b>37</b>
2.4.1	Thermomechanical Conversion	38
2.4.2	Magnetomechanical Conversion	39
2.4.3	Electromechanical Conversion	40
2.4.4	Fluid Mechanic Conversion	41
2.4.5	Multiple Conversion	41
2.4.6	Summary on microactuators	41



---

<b>2.5 Compliant mechanisms</b> . . . . .	<b>43</b>
<b>2.6 Parallel Kinematic Mechanisms (PKM)</b> . . . . .	<b>44</b>
2.6.1 Kinematics of robots . . . . .	46
2.6.2 Singularity analysis . . . . .	48
2.6.3 Performance evaluation . . . . .	49
2.6.4 Robot vision control . . . . .	50
<b>2.7 Laser systems</b> . . . . .	<b>52</b>
2.7.1 Definitions . . . . .	52
2.7.2 CO2 laser . . . . .	52
2.7.3 Thulium YAG laser . . . . .	53
2.7.4 Femto-second laser . . . . .	53
2.7.5 Safety and classes of lasers . . . . .	53
<b>2.8 Synthesis and our proposition</b> . . . . .	<b>54</b>

---

## 2.1 Introduction

The design, fabrication and control of a microrobot devoted to improve the level of knowledge and of development achieved in laser phonomicrosurgery involve several topics. Some of these topics are reviewed in this chapter.

- First, we review **medical robotics** in Section 2.2.
- As the robot that we will design should have small sizes (millimetric or submillimetric), **microdevices** are afterwards reviewed in Section 2.3.
- The performances specified for the application also lead us to do a survey on possible **actuators** for microdevices. This survey is presented in Section 2.4.
- Most devices used as laser steering have a closed loop architecture. Thus a review of **parallel robots** and their issues is treated in Section 2.6.
- Finally, we review **laser technologies** in Section 2.7.

## 2.2 Medical robotics

### 2.2.1 General aspects

The strong demand to improve health quality has expanded the horizons of medical treatments. The synergy between robotic technologies and medical knowledge (transfer of medical knowledge to robotic technologies and use of robots for medical applications) is increasing to answer that demand and results in the so-called *medical robotics*.

More formally, medical robotics consists in combining the medical practitioner knowledge and skills with a robotic system. The emerging medical applications of robots can be classified

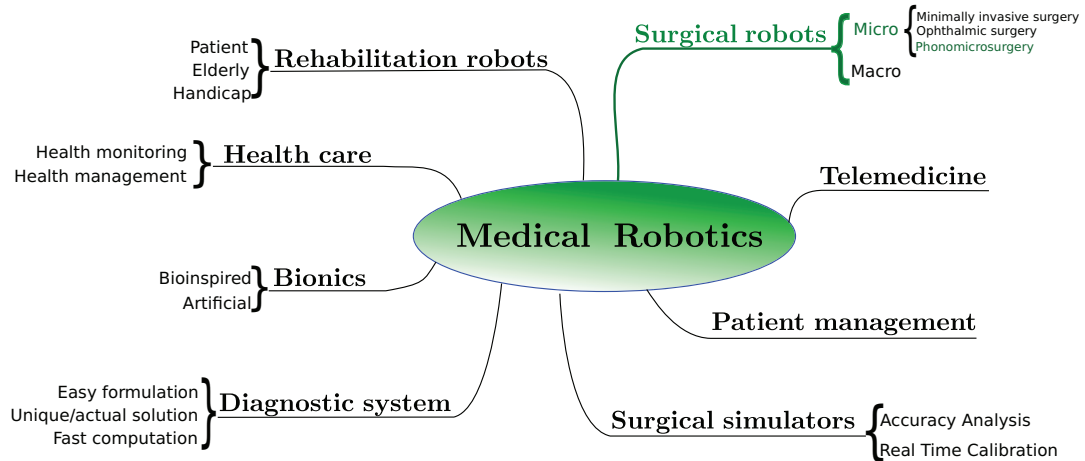


FIGURE 2.1: Medical applications of robots.

into: surgical<sup>1</sup> robots, rehabilitation robots, bionics, surgical simulators, telemedicine, health care, patient management and diagnostic system, as depicted in Figure 2.1.

Surgical robots are all the technological developments which use robotic systems to aid in surgical procedures or in surgical tasks. Surgical tasks employ robotic technologies in order to achieve better performances than conventional surgeries. Dario [40] claims that surgical robots would become a powerful surgical technique beneficial to the patients integrity, time of recovery and cost for assistance. Numerous researches in the field of surgical robots have been carried out during the last twenty years. However only few of them have been industrialized [42]. There are several similar terms to describe the surgical robots: robotic surgery systems, computer-assisted surgery, robotically-assisted surgery.

Surgical robots have therefore some characteristics that differ from other medical robots. These characteristics are listed below.

- They are generally in contact with the patient.
- They are usually designed to specific applications.
- They must be easily movable and manually controllable.
- They are able to perform non-repetitive tasks.
- They should be able to resist an optimal cleaning and sterilisation process.

Furthermore, surgical robot systems have potential benefits relative to the other medical robots. They are listed below.

<sup>1</sup>Surgical is the adjective relative to *surgery* which implies a physical intervention on tissues either for diagnosis or treatment.

- They can couple many sources of information (blood pressure, temperature, pulse, etc.) to generate one action.
- They can be used in hostile or space-constrained areas.
- Small targets (blood vessels, cysts, nodules among others at millimeter-scale) can be reached.
- The medical capabilities of the surgeon is highly augmented.

A classification of surgical robots was given by J. Troccaz [160] where four classes have been proposed: i) passive systems that only provide information to the surgeon, ii) active systems that performs (semi)automatic procedures under human supervision, iii) interactive systems (mechanical guides, haptic feedbacks), iv) and teleoperated systems. This classification was complemented by P. Dario [41] into a matrix classification. This matrix denotes the interaction type (passive, active, interactive or teleoperated) versus the type of access (traditional, minimally invasive or endocavitary/endoluminal access), as shown in Figure 2.2.

		Type of Access		
		Traditional Access	Minimally Invasive Access	Endocavitary/endoluminal access
Type of Interaction	Autonomous systems	Systems that execute a planned program or automatically define their path		
	Interactive systems	Semi-active systems (decoupled DOF) and synergistic systems (shared DOF)		
	Teleoperated systems	Master-slave systems and systems with direct drive/control		
	Passive systems	Systems with no actuation (not really robotics)		

FIGURE 2.2: Classification of surgical robots given by P. Dario [41].

Surgical robots can also be classified according to the sizes of the robot used for the intervention. Actually, microrobots for medical applications are the third-generation of medical robots according with [179]. Thus, macrorobots are usually used in open-body surgeries, while microrobots are usually used in minimal invasive surgeries (MIS). With  $\mu$ RALP, endoluminal laser surgeries (ELS) are aimed. ELS necessarily make use of tiny devices (microrobots) to perform such surgeries. In ELS the scalpel is often replaced by a medical laser to perform cutting or ablations of tissues, in order to avoid the tool/tissue contact that could be damageable to the microstructures of the vocal folds.

### 2.2.2 Robot-assisted phonosurgery

Currently, to perform surgeries of the vocal folds, the existing systems combine microgrippers, laser technologies, robotics guidance, and optical systems. Some of them are still at the research level and others are already industrialized and available on the market. They are listed below.

**Systems proposed by Lumenis** This company [107] proposes two systems described below:

- AcuBlade is a system which is placed out of the patient's body and the system focuses a laser spot onto the vocal folds using a laryngoscope, as shown in Figure 2.3a. The system is driven by a joystick and the CO<sub>2</sub> laser source is placed at 40 cm of the aim. Nevertheless, the system has some automated (open-loop) tasks. AcuBlade is the most extended commercialized system to perform phonosurgeries.
- AcuPulse is a system used manually to bring a surgical laser beam (Tm:YAG) into the larynx cavity using a laryngoscope and an optical fiber, as shown in Figure 2.3b. The system is limited in accuracy since this depends on the surgeon's hand. Nevertheless, the system has appropriated size to perform endoluminal treatment.



(a) AcuBlade system.



(b) AcuPulse system.

FIGURE 2.3: Systems proposed by Lumenis.

**System proposed by Johns Hopkins University** In [22] Blanco et al. proposed a system using two manipulators based on a mechanical gripper and on a laser scalpel as end-effector, as shown in Figure 2.4. The system is teleoperated and the accuracy, again, depends on the surgeon's hand. Nevertheless, the system performs endoluminal surgeries.



(a) Internal view.

(b) External view.

FIGURE 2.4: Use of the Da Vinci robot for transoral surgery using a gripper and a laser scalpel.

**System proposed by the University of Pittsburgh** The highly-flexible system is a snake-like mechanism introduced in the laryngeal cavity to perform retraction and cauterization [149]. The system was initially developed for cardiac surgery (under the name of CardioArm [130]). It was demonstrate to be insertable, without neck extension, in the larynx. Yet discussion between the  $\mu$ RALP coordinator and this group raised the impossible use of this system for phonosurgery as it is because the size constraint prevents from deploying the microarms. Moreover, the system is limited in accuracy due to the fact that it is teleoperated. In addition the system is bulky, it takes a lot of space in front of the patient's mouth and in the operating room, as shown in Figure 2.5. Nevertheless, complex maneuverability in three-dimensional space is performed with its teleoperated robotic arms.

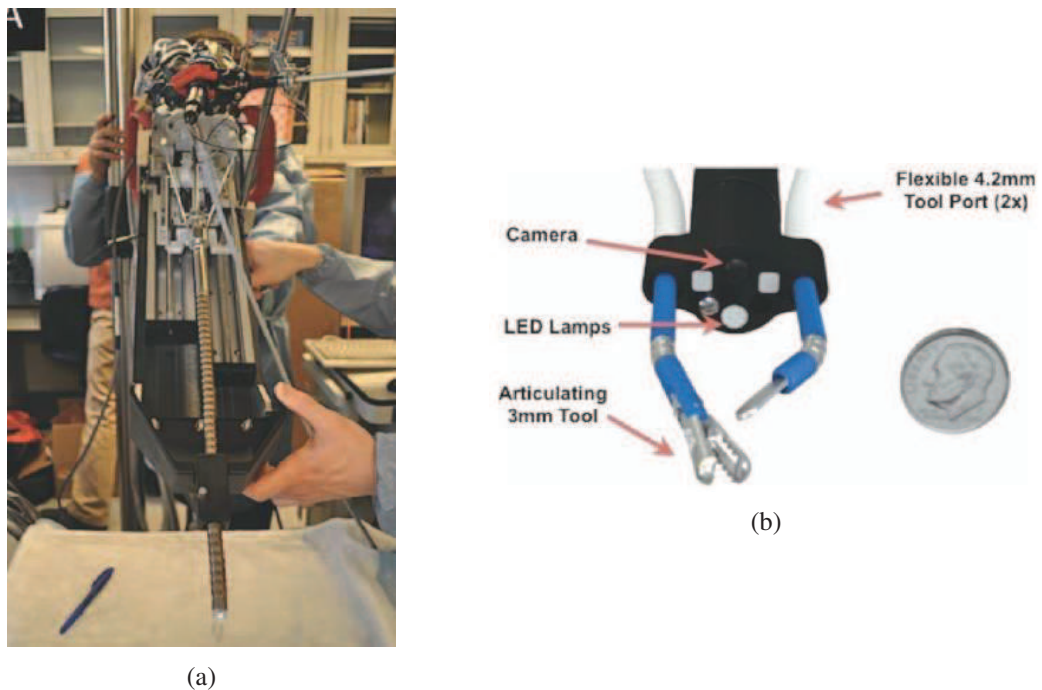


FIGURE 2.5: (a) Whole system holding the flexible endoscope. (b) Set of tools at the end of the endoscope.

**System proposed by the Memorial Sloan-Kettering Cancer Center** Their solution is based on the steering of a CO<sub>2</sub> laser beam onto the vocal folds using a specific adaptive refractive optical setup known as Risley prisms [133], as shown in Figure 2.6. The main limitations are: i) the small range of angles ( $3^\circ$ ) performed by the laser beam, ii) the lack of uniformity of the laser spot (size and power) onto the vocal folds tissue, iii) and the lack of informations about the current position of the laser sport since that only the CO<sub>2</sub> laser is steered without a collimate visible laser.

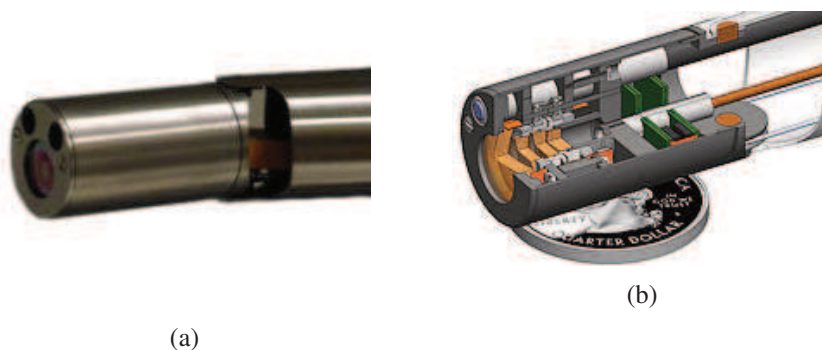


FIGURE 2.6: (a) Distal tip of the endoscope. (b) Lenses and motors inside of the endoscope.



**System proposed by the University of Texas at Austin** Ben-Yakar group proposes a solution for treatment of diseases of vocal folds using optical lenses adapted to modify the orientation of a femto-second laser beam [49], as shown in Figure 2.7. The system is limited, again, by: i) the small range of angles performed by the laser beam, ii) and the lack of uniformity of the laser spot (size and power) onto the vocal folds.

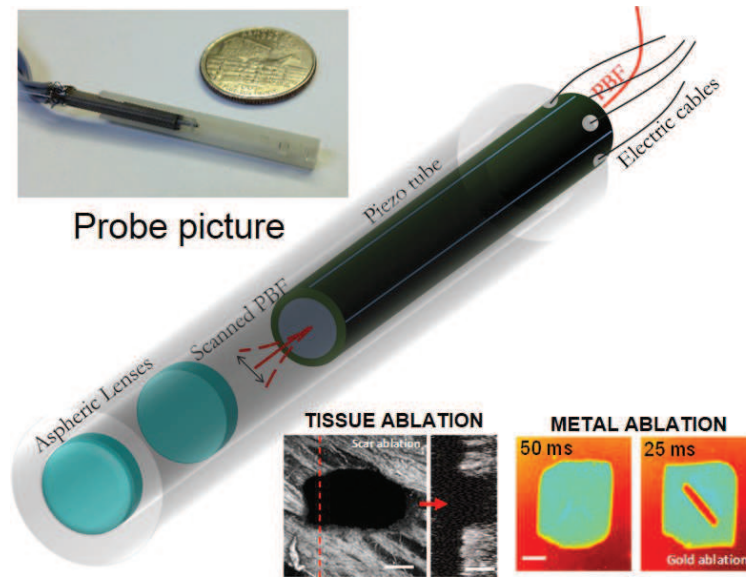


FIGURE 2.7: Endoscope using a femto-second laser.

Table 2.1 summarizes some characteristics of the existing systems for phonosurgery.


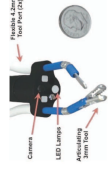

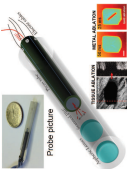

									Lumenis (AcuBlade) [107]	laryngoscope and a laser through an optical fiber	- lack of accuracy - low scanning frequency
									University of Pittsburgh [149]	flexible endoscope with grippers	- lack of accuracy - low scanning frequency
									University of Johns-Hopkins [22]	grippers and laser	- lack of accuracy - low scanning frequency
									University of Texas at Austin [49]	diffractive optics	- small angles - uneven spot diameter - irregular laser power
									Memorial Sloan-Kettering Cancer Center [133]	diffractive optics	- small angles - uneven spot diameter - irregular power laser
University or Company											
Characteristics											
Drawbacks											

TABLE 2.1: Medical devices for vocal folds treatment.



## 2.3 Miniaturized positioning devices and their fabrication

### 2.3.1 Microfabrication techniques

Diverse techniques exist to microfabricate miniaturized and actuated structures. The principal techniques can be summarized as follows and as presented in Figure 2.8, where approximative dimensions are also displayed:

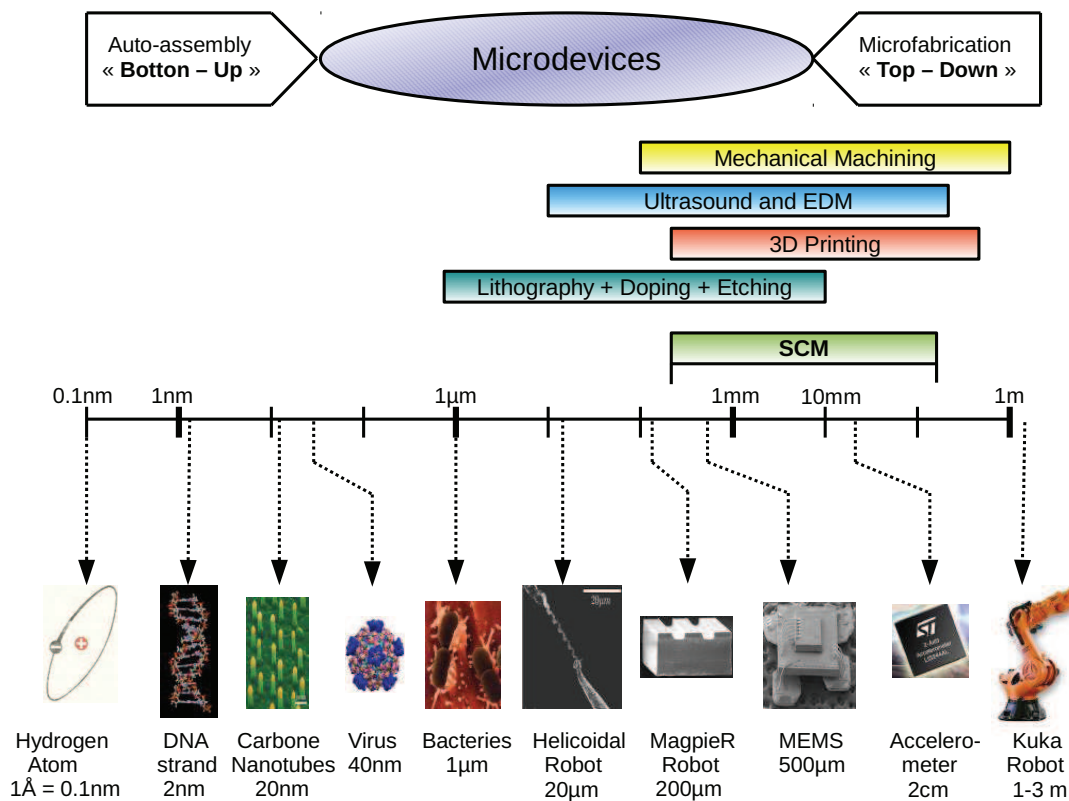


FIGURE 2.8: Different fabrication processes of microdevices.

- lithography,
- techniques by layers,
- doping,
- chemical attack or etching,
- lift-off,
- microfabrication by electrical discharge machining (EDM),

- microfabrication by laser,
- micromachining by ultrasound,
- micromechanical machining,
- 3D printing,
- and smart composite microstructures (SCM).

Each of them is briefly described below.

### 2.3.1.1 Lithography

This technique allows to remove or to add material in the form of a pattern. The lithography is also used to prepare substrates for subsequent processes, for instance for further and other microfabrication techniques [181, 108]. The most common form of lithography is photolithography. A photosensitive resin is placed onto the support previously prepared and heated. The thickness of the resin is approximately  $1 \mu\text{m}$ . Then a mask on which is drawn the desired pattern is placed above the resin and the whole is attacked by light. This latter can be a visible light, x-rays, electrons or ultraviolet rays (UV). After the light exposure, depending whether the resin is negatively or positively photosensitive, a part is thereof eliminated. A description of the process is shown in Figure 2.9.

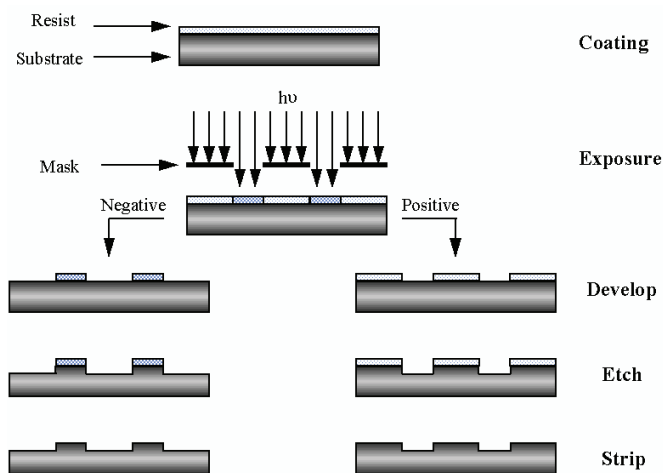


FIGURE 2.9: General schematic of the steps in a lithography process by using positive and negative resist (image from Henderson Research Group [64]).

### 2.3.1.2 Techniques by layers

This method consists in adding conductive or insulating layers on an initial substrate [33]. The thickness of the layers can be different. This technique can be performed in three different ways:

- deposition of thin layers: the thickness varies from a few nanometers to several micrometers. It was originally used to produce semiconductors. The layers have two functions: it serves as conductive circuit and as structure of the chip. To deposit these layers, there are three methods:
  - thermal deposition which is based on the oxidation of the silicon substrate by exposing it to oxygen at high temperature (1200° C). The resulting substrate is chemically resistant.
  - direct deposition which is based on direct spraying or PVD (Physical Vapor Deposition). With these two physical principles, layers of aluminum, chromium, nickel or platinum can be deposited on a substrate.
  - chemical deposition which is based on the deposition of materials as liquid, solid, gaseous or plasma state. The most used state is gas (CVD or Chemical Vapor Deposition). These depositions are placed in a reactor where happens one chemical reaction on the surface. Depending on the operational pressures and temperatures, there is the PECVD (plasma-enhanced), the APCVD (atmospheric pressure), the LPCVD (low pressure), the VLPCVD (very low pressure), the MOCVD (metallorganic chemical) and pyrolysis spray.
- deposition of thick layers which is standard in microelectronics to produce printed circuits. There are different methods of thick film deposition. For example, by screen printing in which one special adhesive is applied onto the substrate via a mask. The whole is then heated at high temperature. The maximum resolution of deposition obtained from this method is 50  $\mu\text{m}$ .
- deposition from a liquid phase in which there are three ways to deposit the material on a substrate:
  - by galvanic way: the substrate is immersed in an electrolysis solution containing the atoms of the material to be deposited. Then a voltage is applied. The atoms are then deposited onto the substrate.
  - by catalysis: the patterns are created by photolithography on an active catalytic metal substrate (for instance Platinum or Palladium). Then the whole is immersed in an electrolyte solution of metal atoms. Finally the patterns are filled by the deposited metal and the resin of the photolithography process is removed. This method is mainly used to deposit metals.
  - by spin coating: a layer of a material under liquid phase is placed on the substrate and turned at high speed with this latter. The liquid distributed over the surface is hardened via a drying process.

### 2.3.1.3 Doping

This method is the most known for manufacturing semiconductors in microelectronics. It is mainly used for silicon materials. This method consists in introducing doping atoms in a silicon substrate which permits to change its properties such as: electrical, corrosion, burning

temperature, hardness, etc. [154]. There are two doping sub-methods: by diffusion and by ion implantation.

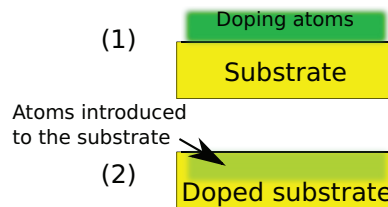


FIGURE 2.10: General schematic of the doping process.

#### 2.3.1.4 Chemical attack or etching

This method consists in burning and removing unprotected part of a substrate. A resistance layer with patterns (mask), is used to separate protected and unprotected parts [103]. There are two methods of chemical etching:

- wet chemical attack in which the entire substrate and mask are plunged in an etching bath or sprayed on with etching solutions (acid or alkaline). If the material is monocrystalline, the attack depends on the crystal direction. It is an anisotropic etching. If the material is polycrystalline or amorphous, the attack is the same in all directions. It is an isotropic etching.
- dry attack in which the substrate with the mask is exposed to an ionized gas (plasma). The pattern appears during chemical interactions between the gas and the atoms of the non-protected substrate.

#### 2.3.1.5 Lift-off

This method is generally used to fabricate pins of chips. After a process of photolithography, a material is sprayed to the substrate. The remaining resin is finally removed and the desired structure is obtained [83]. This technique is applied when a direct etching of the material has undesirable effects on the layers.

#### 2.3.1.6 Electrical discharge machining (EDM)

The electric discharge machining (EDM) consists in removing materials by using an electrical spark. In fact, the tool and the material to be machined serve as electrodes to which a voltage is applied. The material removal is caused by high local heating. The two electrodes are plunged in a dielectric fluid which is intended to clean the surface and to rapidly re-solidify it. The material to be machined is generally electrically conductive but semiconductors (as silicon) can also be treated. An advantage of this method is that it allows to machine extremely hard metals [5]. There are two EDM methods depending on the tool used: EDM by wire and EDM by sinking.

- EDM based on wire: the wire is generally made of copper or tungsten with a diameter of  $25\ \mu\text{m}$  to  $300\ \mu\text{m}$ .
- EDM based on sinking: the tool is a volume or a hole having the shape complementary to the desired final piece. The matrix (the tool) is made of copper or graphite, while the dielectric fluid is oil or gasoline.

### 2.3.1.7 Microfabrication by laser

Micromachining with laser allows to vaporize portions of a material in a selective mode to achieve the desired design [45]. Its main advantage is the ability to machine a wide variety of materials: most of metals, ceramics, plastics, carbon fiber, etc. There are two methods of laser micromachining as described below:

- by focusing the laser beam: the laser beam is focused in a point on the workpiece material. Then moving the laser spot in the axes  $x$ ,  $y$  or  $z$  permits to vaporize portions of this. This method is useful for drilling or cutting, as shown in Figure 2.11.
- by projection on a mask: a mask pattern is placed between the laser source and the workpiece. This method permits to only vaporize the non hidden parts. In general, it is used for superficial patterns. To get considerable depth the operation is repeated several times.

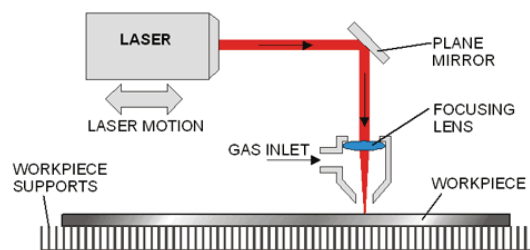


FIGURE 2.11: General schematic of the laser micromachining process using a laser beam focused on a point of the workpiece (image from [50]).

### 2.3.1.8 Micromachining by ultrasound

When materials are not conductors or semiconductors or when their surfaces are difficult to machine chemically, most of the processes mentioned above do not work. Ultrasound based methods are among the processes that treat virtually any material. They can machine hard materials as well as fragile materials, conductors and insulators. The principle is based on a tool with a vibratory movement perpendicular to the surface of the workpiece, and on the injection of an abrasive liquid between the workpiece and the tool [191]. The active surface of the tool reproduces the shape of the required machining. Fragile materials are easier to machine. The precision depends on the amplitude of the vibrations performed by the tool and by the class of the abrasive used. The speed of machining depends on the type of the abrasive, the amplitude and the frequency of the vibrations.

### 2.3.1.9 Micromechanical machining

Micromechanical machining meets all the classical mechanical machining (milling, drilling, turning ...) but with dimensions lower than the millimeter. Drilling was the first process to be downscaled and the resulting new process was called microdrilling. Most of the methods presented above do not involve measurements verification (metrology) during the manufacturing process, contrary to micromechanical machining. In micromechanical machining the relative tolerance can vary from 10% to 0.1% of the micro-object dimensions [140, 89, 77]. Micromechanical machining includes the following processes: microdrilling, microturning, micromilling, micropolishing, microgrinding, microsawing.

### 2.3.1.10 3D Printing

This technique is a particular case of fabrication by layers (see Section 2.3.1.2). 3D printing is based on the deposition of thick layers of a melted resin [19, 169] or melted metals [135]. The resolution of the obtained devices is about 50  $\mu\text{m}$ . This technique is mainly addressed to fabricate supports and basis and to rapidly make prototypes, as shown in Figure 2.12.

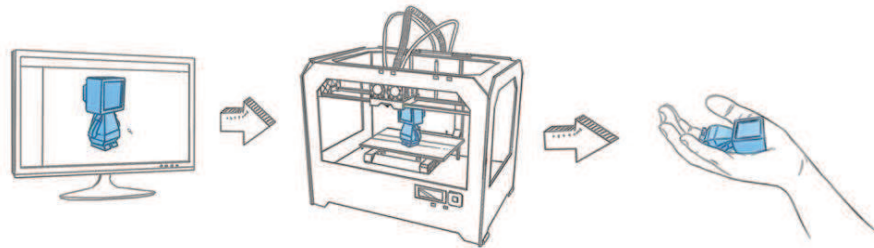


FIGURE 2.12: 3D printing process (image from [2]).

### 2.3.1.11 Smart composite microstructures (SCM)

As seen above, microfabrication in the fields of MEMS and microelectronics are based on planar technologies: constructing the devices on planar substrates. Microelectronics industry has made huge investments to develop wafer-based process technologies. Thereby, there is a correspondingly huge advantage for MEMS designers to exploit the same processes like lithography, doping, etching, etc. However, all the resultant devices made with these processes are constrained to be 2D-structures. These 2D-structures can reach very small rotations (out of the plane) and small translations i.e. the material of the structure are forced to be compliant. However, unfortunately and frequently, specifications are more demanding than what the material can afford without breaking or decreasing drastically its lifetime.

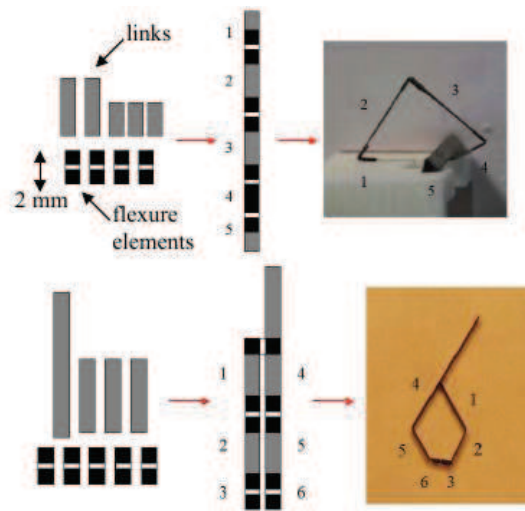


FIGURE 2.13: Construction of four-bars and five-bar structures from links and flexure elements [157] by using SCM technology.



FIGURE 2.14: Example of Micro-Air-Vehicle (MAV) using SCM [186].

The SCM fabrication process consists in building structures of 3D shapes from 2D initially fabricated patterns. These structures are made of high stiffness materials (as rigidified carbon fiber layers) combined with thin and flexible materials (as layers of polyimide). The patterns are first fabricated and micromachined by laser (see Section 2.3.1.7). Then, all the components are bonded into a flat structure on an oven. Later, these flat structures are folded in order to obtain 3D structures, as depicted in Figure 2.13.

The SCM technology has been developed and explained in [157, 186, 185, 72] and has been intensively used to fabricate mobile robots and micro-air-vehicles (MAVs), as depicted in Figure 2.14. SCM technology gives another option to scale down traditional mechanisms replacing conventional revolute joints by compliant joints.

Among the SCM benefits, we have:

- structures made by SCM are easy to assemble,
- the manufacturing cost is relatively low,
- SCM technique provides the possibility to scale mechanisms easily.

Hence the ease of assembly and the low cost can facilitate the serial production of microdevices using SCM. In addition, to be easy to scale, SCM allows the ease of customization of the products.

### 2.3.2 Microplatforms and microsystems for precise positioning

In this section, we provide some existing platforms and microsystems for precise positioning i.e. micro/nanopositioning. The survey is limited to systems which have dimensions less or equal to the specified dimensions ( $10 \times 10 \times 10 \text{ mm}^3$ ). It is worth to notice that in some cases the device alone can have very tiny dimensions but the whole package (including mechanical support and electrical connections) can exceed the specified dimensions. Among the variety of microplatforms, we can classify them into two categories according to the operation mode. They are listed below.

- Resonant or dynamic operation mode:** In general, the devices in this class have a high-speed with low power consumption. This kind of microdevice has the operation point at a resonance frequency. High frequencies are therefore used and large displacements are usually obtained. The limitation of these systems is the non-controllability of the path or of the trajectory. Today many commercial actuated micromirrors use such a resonant mode of operation. Some devices using this operation mode are described in [35] and one example is the DMD (Digital Micromirror Devices) from Texas Instruments [1]. They are mainly used in applications such as image projection, switch of optical fiber to optical fiber and OCT (optical coherence tomography).
- Static operation mode:** The devices in this class perform less angles than those of resonant mode. The advantage is the total controllability of the position and orientation of the platform. They have many applications such as optical target tracking [183]. Our objective lies more in this class.

Let us now review platforms working in static operation mode.

In [188], a 3-DOF platform able to position a MEMS mirror (two orientations and one linear motion) was developed, as shown in Figure 2.15. Based on the electrothermal principle, the platform is used in an endoscopic probe of diameter less than 5.3 mm and has chip dimensions of  $2 \times 2 \text{ mm}^2$ . Despite the compactness of the platform, its range ( $2.5^\circ$ ) is limited and is far less than the specifications in the  $\mu$ RALP project.



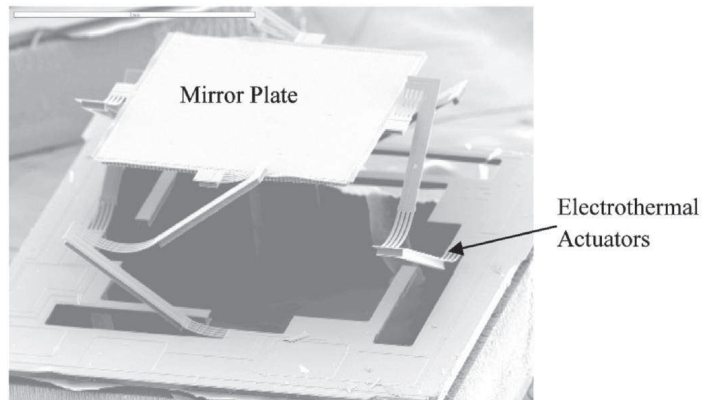


FIGURE 2.15: Platform based on the electrothermal principle [188].

In [193], the same platform as in [188] was developed, but instead of using electrothermal actuation, piezoelectric actuators were employed in order to increase the bandwidth, as shown in Figure 2.16. The device shows a first resonant frequency more than 250Hz, however its range of orientation is still limited to less than  $\pm 1^\circ$ .

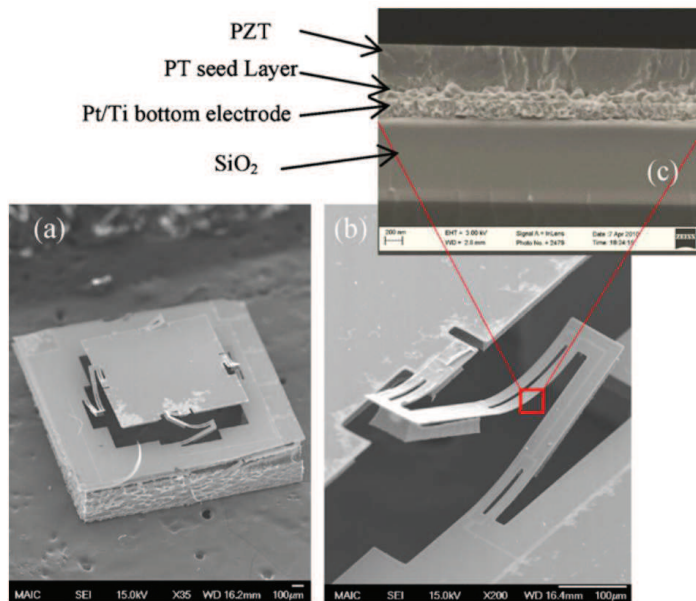


FIGURE 2.16: Platform using electrothermal and piezoelectric actuators [193].

A 2-DoF (one translation and one orientation) electrothermal platform with  $1 \times 1 \text{ mm}^2$  chip devoted to endoscopic optical coherence tomography (OCT) was also developed in [86], as shown in Figure 2.17. This platform possesses a high range and a high bandwidth. Indeed, its range of positioning is in excess of  $-20^\circ / +50^\circ$  for the orientation and the bandwidth is more than 250Hz. However, the heating temperature is high (more than  $100^\circ\text{C}$ ) and may not be

convenient for phonomicrosurgery applications. Moreover, its kinematics does not allow for a static center of rotation, which is required by our application.

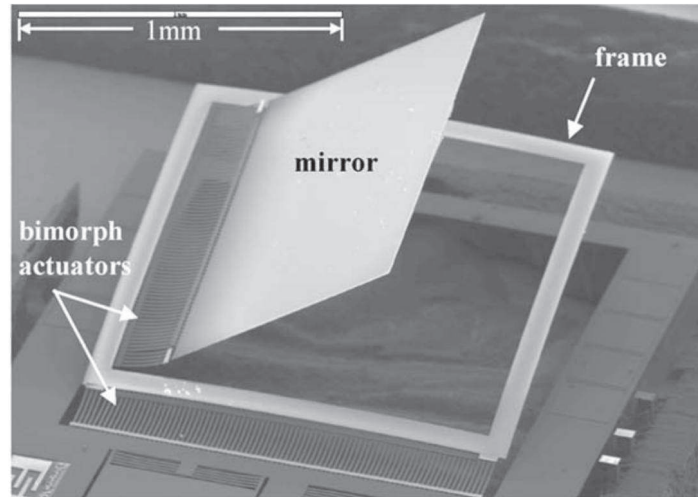


FIGURE 2.17: Platform with high range and bandwidth but with a very high heating temperature [86].

A modified version of the platform in [86] was proposed in [88] in order to increase the translation range. Despite the good performances, the working temperature range (about  $150^{\circ}\text{C}$ ) of the device is still not adapted to the applications considered in the  $\mu\text{RALP}$  project, in particular for biocompatibility reasons.

Another electrothermal 2-DoF platform was proposed in [146], as shown in Figure 2.18. Based on Z-shaped electrothermally actuated cantilevers allowing positive-and-negative movements, the platform includes sensing elements all in less than  $2 \times 2 \text{ mm}^2$  chip. Despite its high level of packageability, the offered type of DoF (1 orientation and 1 translation) is not congruent with our requirements and the developed angles are not enough.

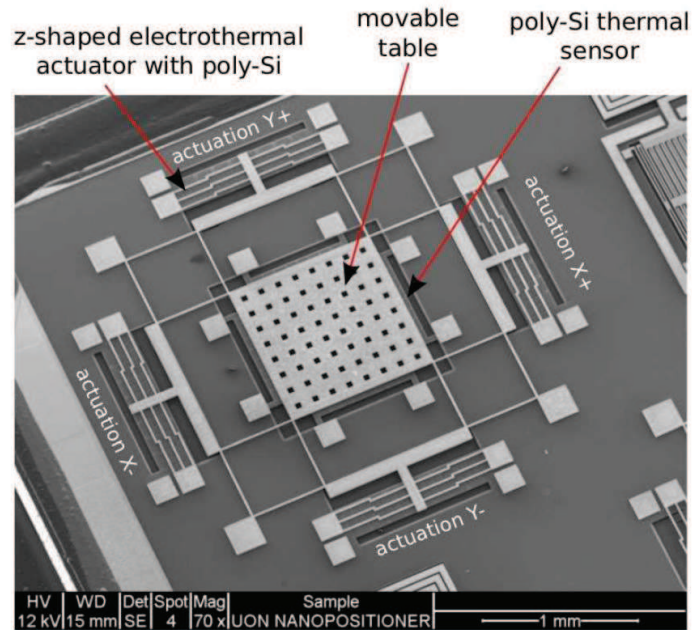


FIGURE 2.18: Platform with electrothermal actuation [146].

An electrostatic 2-DoF (translation-translation) actuated platform was proposed in [51], as shown in Figure 2.19. The platform possesses an important resonant frequency (more than 800Hz). However the movement is uni-directional and then can not satisfy applications that require positive and negative directions. In addition, once again the type of DoF (translation-translation) is not suitable for our application.

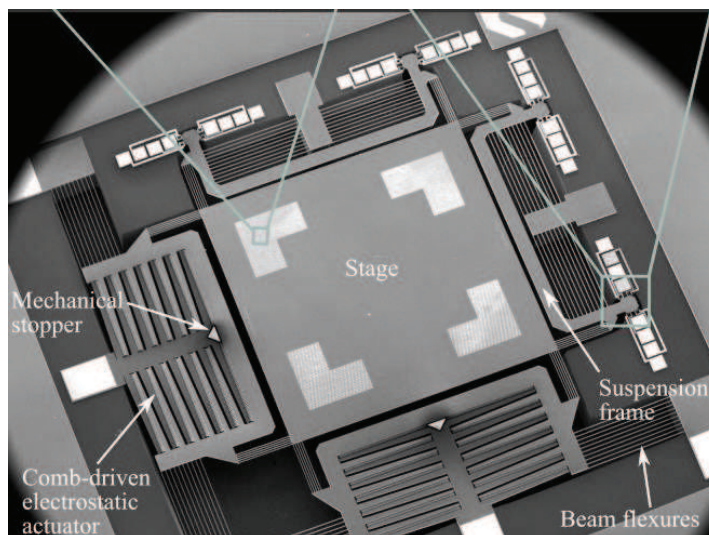


FIGURE 2.19: Platform actuated by comb-drive electrostatic (capacitive) actuators [51].

Other electrostatic 2-DoF (orientation-orientation) platforms were studied in [158, 100, 137, 170]. The designs offer resonant frequencies of about 720Hz and rotation angle between  $\pm 5.5^\circ$  and  $10^\circ$ , as shown in Figure 2.20. Again compared to the specifications of the  $\mu$ RALP project, these ranges are not sufficient enough.

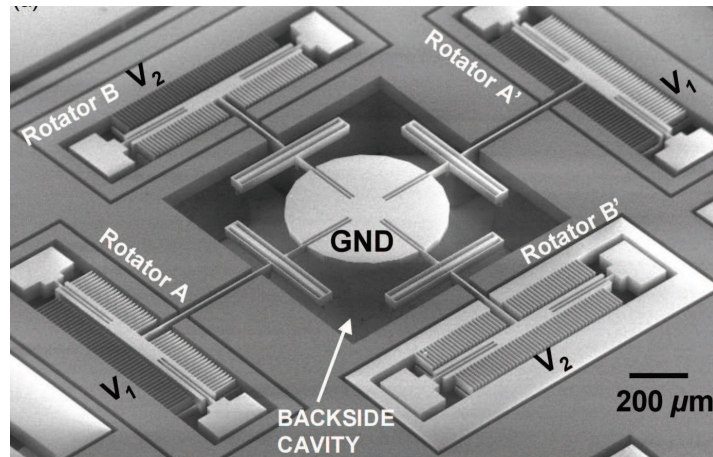


FIGURE 2.20: Platform with electrostatic actuation [100].

Electromagnetically actuated 2-DoF (orientation-orientation) platforms have also been developed. They demonstrated rotation angles of  $\pm 15.7^\circ$  [30] and  $\pm 18^\circ$  [20]. The main limitation is that they require large external magnets that impeded the suitability of such techniques to pack-able platforms such as required in the  $\mu$ RALP project.

## 2.4 Actuators for high resolution positioning

Actuators transform electric, thermal, magnetic or other energy type into mechanical work. Actuators are key components in robotics. Usually, in micromechanisms, the word used to designate actuators is “microactuators”. In these micromechanisms, the microactuators are often made of active or smart materials. Active materials have remarkable features such as high resolution and/or high bandwidth. In addition, most of them can be used for sensing additionally to the actuation. However, active materials are also very sensitive to environmental conditions and have usually strong nonlinear behavior such as hysteresis which need to be compensated by a suitable control system.

The choice of a microactuator for a micromechanism is done to meet several criteria such as:

- the input energy,
- the power consumption,
- the strain amplitude,

- the available dimensions,
- the available fabrication technology and associated ease of use,
- the repeatability and the bandwidth,
- the force and the torque to be developed,
- the stiffness,
- the cost,
- and the biocompatibility.

A microactuator has an identical definition to that of a traditional actuator, which is a system that transforms any type of energy (electric, thermal, magnetic, chemical, etc.) into mechanical work (displacement and force) [48, 58, 138, 59]. In micromechanisms, the term microactuator implies that the transducer that generates the displacement typically provides micrometric or submicrometric resolution. The dimensions of a microactuator are generally lower than 10 mm.

According to the input energy, there are different types of actuators usually used, as shown in Figure 2.21. They are described in the following subsection. This part is inspired from [141].

#### 2.4.1 Thermomechanical Conversion

Here the input energy is thermal. Such actuators have the disadvantage of being slow and are subject to heat dissipation concerns.

**Microactuators obtained with thermal dilation of a solid** The thermal dilation of a solid is exploited here. An example is the actuation of the micromirror in [87]. Usually, the actuator is based on two or more materials of different dilation-coefficients.

**Microactuators based on thermal expansion of a gas** As Gay Lussac's law describes, the volumetric expansion of a gas can be used to create a displacement. Examples of these microactuators are the micro-engines proposed in [112, 105].

**Shape Memory Alloy microactuators (SMA)** A shape-memory alloy is an alloy that finds its original shape when heated [98, 18, 23, 150, 95], the original shape being created by cold-forging. Their principle is based on solid-state to solid-state phase change. These alloys are still relatively expensive to manufacture and are difficult to machine compared to other materials such as steel and aluminum. Most SMA's have poor fatigue properties. An example of utilization of SMA is the active endoscope based on SMA microactuators [109].



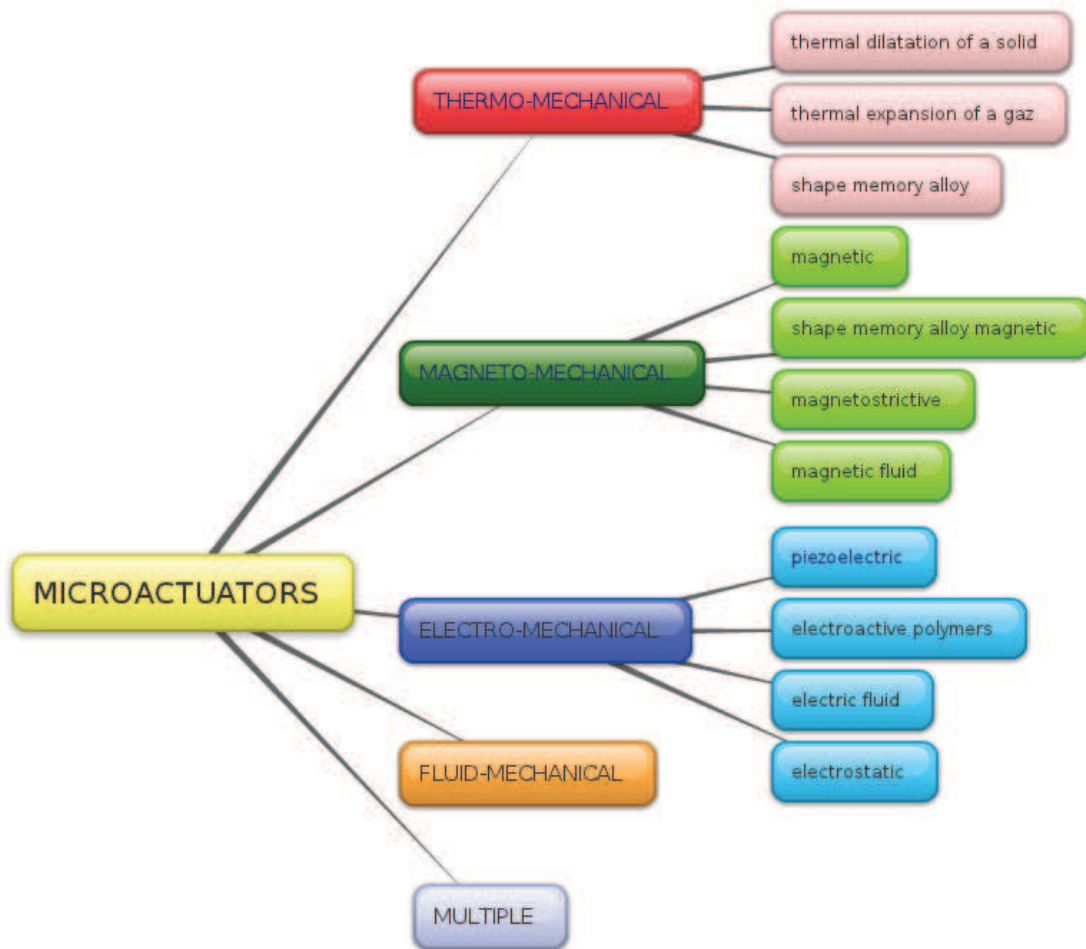


FIGURE 2.21: Actuators Classification

### 2.4.2 Magnetomechanical Conversion

The input energy is of magnetic type. Magnetic principle based actuators have the advantage of possible remote control. However, the repeatability is weak and the actuators exhibit strong nonlinear behaviors.

**Magnetic microactuators** Here the attraction force produced by a magnetic field<sup>2</sup> is used to create a displacement of ferromagnetic materials. However the use of high frequencies (KHz, MHz) and high amplitudes magnetic fields can be harmful for humans as described in [163], making this type of actuators less convenient for medical applications. An example of this type of actuator is the magnetic micromotors of [25].

**Magnetostrictive microactuators** These actuators have their shape and dimensions changed when subjected to a magnetic field due to the magnetostriction property [126, 65, 174].

<sup>2</sup>Magnetic field: generated by permanent magnets or electromagnets.

An example of application is the loudspeaker based on magnetostrictive microactuators [12].

**Magnetic fluid microactuators** These actuators use fluids that respond to magnetic fields: magnetorheological fluids and ferrofluids [28, 4, 189]. An example of this type of actuator is the micropumps described in [81].

**Magnetic Shape Memory Alloy microactuators (MSMA)** The principle is similar to classical SMA, but instead of the temperature, the excitation can also be a magnetic field [56, 54, 55]. An example of this type of actuator is the microvalves for fluid control systems described in [118].

### 2.4.3 Electromechanical Conversion

The electromechanical conversion is based on the transformation of electrical energy into mechanical energy.

**Piezoelectric microactuators** Piezoelectricity is a phenomenon which makes electrical charges appear on the surfaces of a material when it is exposed to a mechanical load. This is called the direct piezoelectric effect<sup>3</sup> which is used for sensor design. This effect is reversible. In the converse effect, deformation is obtained when an electrical field is applied<sup>4</sup>. Piezo actuators offer a high resolution (up to some nanometers), a high bandwidth (up to tens of kilohertz) and a high force density compared to others smart materials. All that makes them well recognized for microactuators design [13, 34, 92, 104, 10, 43]. Lead Zirconate Titanate (PZT) is the most used piezoelectric material in the world and its biocompatibility has been proven in [125] under certain conditions. Piezoelectric microactuators can be *piezostacks* [9] or *piezoelectric cantilevers*. In cantilevers, the section can be rectangular (multimorph) or circular (piezotubes). These simple structures can be used to develop more complex systems like *Inch-Worm* [176], *Impact-Drive* [67] or *Stick-Slip* [134] actuator. However these arrays allow to increase the range of movement but decrease their dynamic performances.

**Electro-Active Polymers based microactuators (EAP)** Electroactive polymers are polymers which exhibit a deformation when they are exposed to an electric field. The deformation can be large but the generated forces are often weak. They are considered as biocompatible. In addition, the input voltages used to supply them are low. However, most electroactive polymers typically have low bandwidth, making them not suitable for applications with high speed tasks [156]. An example are the micromuscles developed in [117].

**Electric fluid microactuators** They are fluids that react to an electric field. They often require high input energy. An example is the valves controlled by fluids electrically actuated described in [27, 26].

---

<sup>3</sup>Discovered by Pierre and Jacques Curie in 1880 [113].

<sup>4</sup>Predicted by Gabriel Lippmann in 1881 and immediately confirmed by the Curie brothers [32].

**Electrostatic microactuators** The principle of operation is based on the Coulomb attraction between two electrically charged bodies. The force generated by the actuator depends on the distance between the surfaces, the levels of electric charges and the media between the two surfaces. The operating voltage for this kind of microactuators are between 40 V and 200 V [114, 39, 99, 14, 84]. An example is the arrays for air-flow control described in [52].

#### 2.4.4 Fluid Mechanic Conversion

When the pressure or the flow of a hydraulic or pneumatic fluid is used to obtain a linear or angular motion or a bending, a fluid mechanic microactuator is obtained. Currently, few numbers of fluid mechanic microactuators exist. An example is the scanner endoscope system developed in [153].

#### 2.4.5 Multiple Conversion

When several energy conversions are used in the same microactuator, the multiple conversion principle is achieved. Actuators of this principle are also called hybrid actuators. The commonly used of this kind is the electrothermal microactuators that combines electrical and thermal energies to provide a mechanical work. More precisely, electricity is used to create the thermal energy, by Joule effect, and this later is employed to create the mechanical displacement of force [147].

#### 2.4.6 Summary on microactuators

Each of the above microactuator offers advantages and disadvantages. Certain criteria should be used to evaluate and thus to choose the actuators, all that depending downright of the application.

Table 2.2 synthesizes the different characteristics of these actuators. They are: the resolution, the energy density, the possibility or not to have bi-direction of actuation, the typical response time, the connection type, the efficiency<sup>5</sup> and the biomedical compatibility.

---

<sup>5</sup>Efficiency to transfer the input energy to the output.



Input Energy	Actuator transductor	Reso- lution	Energy density	Bi - Direction of Actuation	Typical response time [ms]	Connection type	Effi- ciency	Biocom - patibility	References
Thermal	Thermal dilation of a solid	-	++	No	100 - 800	Convection or Wire	~	~	[87, 147]
	Thermal expansion of a gaz	-	+	No			~	~	[112, 105]
Magnetic	Shape Memory Allow (SMA)	+	~	No	1 - 10	No Connection	+	~	[98, 18, 23, 150, 109, 95]
	Magnetic	+	~	Yes			+	~	[163, 25]
	Magnetic SMA	++	~	No			+	~	[56, 54, 55, 118]
	Magnetostrictive	++	++	Yes			+	~	[126, 65, 174, 12]
Electrical	Magnetic Fluid	++	+	Yes	0.1 - 100	Wire	~	~	[28, 4, 189, 81]
	Piezoelectric	+++	++	Yes			++	+	[125, 13, 34, 92, 104, 10, 43]
	Electroactive Polymers	-	-	No			-	-	[156, 117]
	Electric Fluids	+	+	Yes			~	~	[27, 26]
Fluidic	Electrostatics	++	~	No	~ 500	Pipes	~	~	[114, 39, 52, 99, 14, 84]
	Hydraulic/Pneumatic	-	++	Yes			+	~	[153]

TABLE 2.2: Comparison of microactuators.

where:

+++ very high  
 ++ high  
 + good  
 ~ regular  
 - poor

## 2.5 Compliant mechanisms

Nowadays, miniaturizing devices is a trend in several areas. Nevertheless, the direct miniaturization poses challenges at different levels, including the assembly process. Thereby, a basic and essential desire is to build complex micromechanisms with few small pieces and components to be assembled. Micro-assembly tools such as grippers or others mechanisms without contact are still under development [152, 3]. To remedy this lack of tools of micro-assembly, compliant mechanisms have been proposed as one of the bases in the manufacture of microdevices.

Compliant mechanisms, also called mechanisms with flexure hinges, are suitable to that spirit since they can be fabricated with only one bulk (a monolithic structure) instead of several components like in classical mechanical hinges. A definition given by [106] of a flexure hinge is a thin member that provides the relative rotation between two adjacent rigid members through flexure.

Some of the advantages of flexure hinges are:

- no friction and thus high resolution,
- no lubrication required,
- no backlash due to mechanical clearances, therefore hysteresis is prevented,
- possibility to be integrated in microscale structures,
- easy to manufacture,
- practically no maintenance needed.

Yet, flexure hinges have limitations, such as:

- relatively low range of rotation,
- complex deformation (torsion combined with flexure/bending),
- non-fixed rotation center during the deformation of the flexure hinge,
- high local divergence of stress around the deformed part of the flexure hinge,
- different spring rates in the rotation,
- sensitivity to temperature variations.

Most of the time, micromechanisms are based on smaller subparts. These subparts generate their motion by means of flexure-like components, as shown in the Figure 2.22. Generally they are fabricated by removing materials from the initial wafer, for instance with either end-milling or electrical discharge machining or photolithography, as was discussed in Section 2.3.1.

Nevertheless, SCM fabrication process (quickly discussed in Subsection 2.3.1.11) proposes a different way to create flexible hinges made up of polyimide and rigid links based on carbon

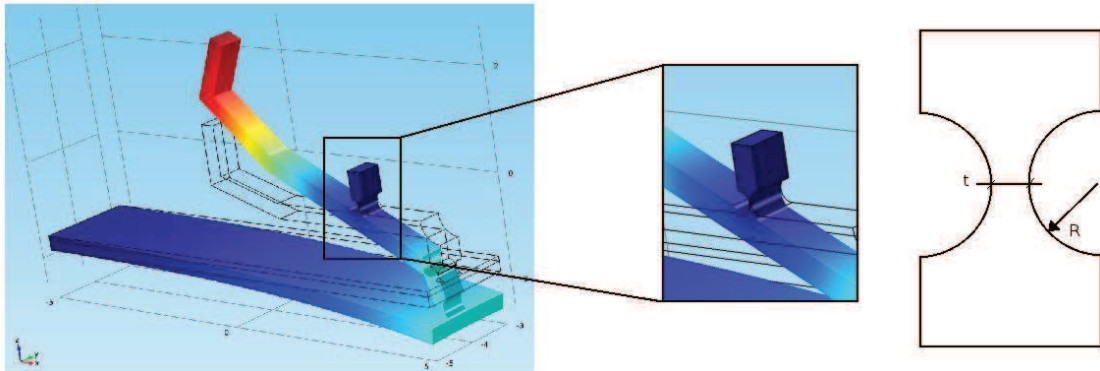


FIGURE 2.22: Compliant mechanical part.

fibers. Flexure hinges made by SCM are flat in the beginning (planar shape) and they are supposed to be compliant only along an axis, which gives them a relative rotation between the two rigid parts. They are usually symmetrical about the longitudinal and middle transverse axes, as shown in Figure 2.23. Flexure hinges of polyimide (sheet of  $10\mu\text{m}$  of thick) are completely compliant i.e. without opposition caused by the rigidity of the material. These compliant hinges yield relatively high range of rotations. However, these hinges present complex deformation (torsion combined with flexure/bending) which can affect the precision of the end-effector of the robot.

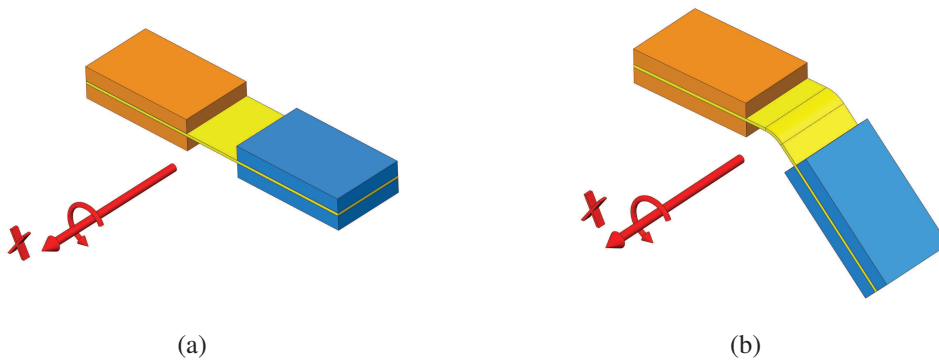


FIGURE 2.23: (a) Flexure hinge manufacture with SCM technology. (b) Flexure hinge with rotation about the x-axis.

## 2.6 Parallel Kinematic Mechanisms (PKM)

Among the variety of microdevices which we have shown in Section 2.3.2, most of them have a parallel architecture. Despite the numerous works on microplatforms, their analysis as parallel

structures has not been enough carried out. This is why this section is dedicated to give a general overview of parallel kinematic machines.

Over the last two decades, parallel manipulators have received a great attention because they have special attractive characteristics such as high stiffness, high local dexterity, low inertia effect, less sensitivity to input errors, high speed conservation, large payload capacity and compact size [120]. An example of a PKM is shown in Figure 2.24.

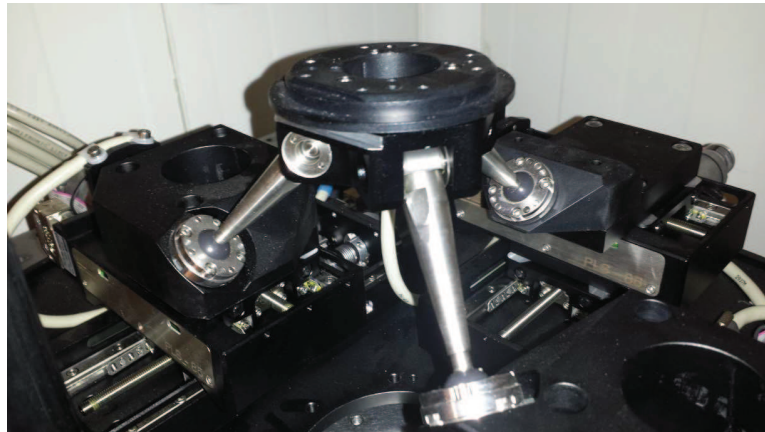


FIGURE 2.24: A 6 DoF parallel robot [136].

Generally a parallel manipulator consists of two rigid plates (the moving and the base platforms) and several actuating links that provide the corresponding degrees of freedom (DoF) for the moving platform with respect to its base platform. There are several similar terms to describe them: parallel robot, parallel mechanism, motion platform, in-parallel mechanism, parallel-link mechanism, closed-loop mechanism, parallel kinematic machine (PKM).

For conventional robot, the kinematic transformation of linear displacement to rotation and conversely rotation to linear displacement is achieved through mechanical joint. It is not convenient for mesoscale and microscale robots due to the space limitation. Furthermore, the superficial forces (pull-up, van-der-Waals, electrostatics) predominate over the volumetric forces (gravity, magnetic force, etc.) when the scale is shrunk, thus the friction forces can limit the performances of conventional joints in small scales. In addition a conventional system with mechanical joints becomes more complex, with less dynamics, and with presence of backlash, which affect the robot accuracy.

Finally, challenging research issues in parallel manipulators are related to the forward kinematics, singularity, workspace, calibration, optimal design, control and implementation, as depicted in Figure 2.25. We will briefly describe them below.

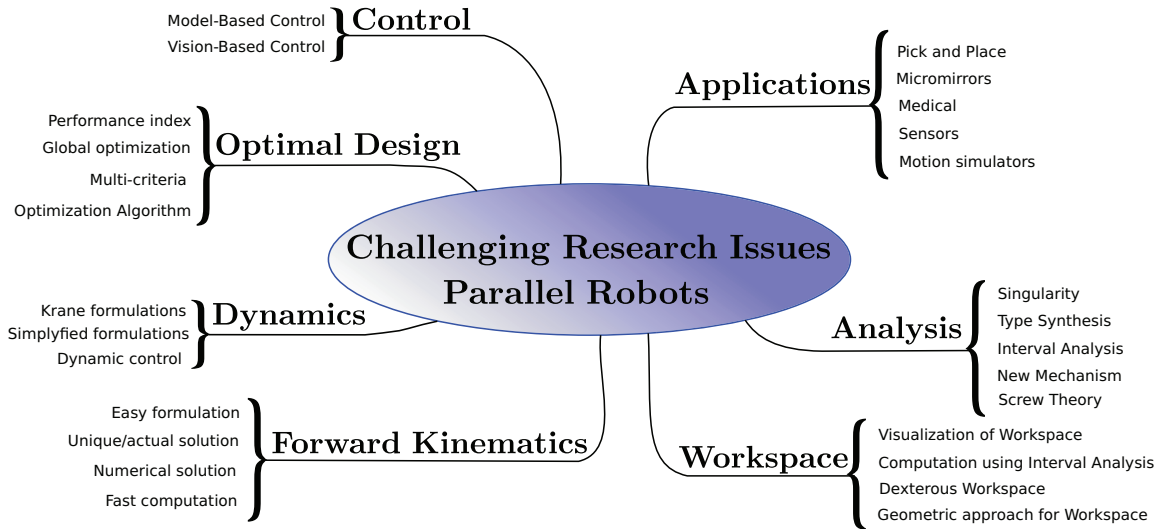


FIGURE 2.25: Challenging research issues in PKMs

## 2.6.1 Kinematics of robots

Robot kinematics deals with the study of the robot motion as constrained by the geometry of the links. The next topics are dedicated only to parallel robots.

### 2.6.1.1 The Zeroth-Order Kinematic Models

These models describe the static relations between the configuration variables such as the platform or end-effector pose  $\mathbb{X}$  and the joint variable value  $q$  of the robot, in relation with the kinematic structure and its geometrical parameters ( $\xi_{geo}$ ).

#### i) Implicit Kinematic Model (ImplKM)

This model gives a non-causal relation between the end-effector pose ( $\mathbb{X}$ ), joint variable value ( $q$ ) and the geometric parameters ( $\xi_{geo}$ ) called implicit model. The implicit model is a holonomic constraint for any relevant state of the variables:

$$M_{\phi}^0(\mathbb{X}, q, \xi_{geo}) = 0 \quad (2.1)$$

where  $M_{\phi}^0$  is the implicit kinematic model of a parallel robot. From this model, generally easy to express thanks to the so-called loop closure constraint, one can extract two causal relations: the inverse and the direct kinematic model.

### ii) Inverse Kinematic Model (IKM)

This model describes the joint variables values ( $q$ ) given the end-effector pose ( $\mathbb{X}$ ) and the geometric parameters ( $\xi_{geo}$ ) of the robot. Generally the IKM of parallel robots yields a unique decoupled solution for each leg of the mechanism:

$$q_i = M_{I_{p_i}}^0(\mathbb{X}, \xi_{geo}), \quad i = 1, \dots, n \geq 2 \quad (2.2)$$

where  $M_{I_p}^0$  is the inverse kinematic model of a parallel robot. The super-right script denotes the order of the kinematic models.

### iii) Forward Kinematic Model (FKM)

This model describes the pose of the end-effector ( $\mathbb{X}$ ) given the joint variables values ( $q$ ) and the geometric parameters of the robot ( $\xi_{geo}$ ).

$$\mathbb{X} = M_{F_p}^0(q, \xi_{geo}), \quad i = 1, \dots, n \geq 2 \quad (2.3)$$

where  $M_{F_p}^0$  is the forward kinematic models of a parallel robot. Notice that the FKM of parallel robots is often highly coupled and might offer several solutions.

#### 2.6.1.2 The First-Order Kinematic Models

The time differentiation of the previous kinematic models gives the differential kinematic models relating the Cartesian velocity of the end-effector pose to the speed of the actuators.

### i) Implicit Differential Kinematic Model (ImplDKM)

The differentiation of (2.1) yields the implicit differential kinematic model:

$$\frac{\partial M_{\phi}^0(\mathbb{X}, q, \xi_{geo})}{\partial \mathbb{X}} L_{\mathbb{X}} \zeta + \frac{\partial M_{\phi}^0(\mathbb{X}, q, \xi_{geo})}{\partial q} \dot{q} = 0 \quad (2.4)$$

or equivalently,

$$M_{\phi(\mathbb{X})}^1 \zeta + M_{\phi(q)}^1 \dot{q} = 0 \quad (2.5)$$

where  $\dot{\mathbb{X}} = L_{\mathbb{X}} \zeta$ ,  $\zeta = [v \ \omega]^T$ ,  $v$  and  $\omega$  are the linear and angular velocities of the platform.

This model has two matrices: i) the differential Cartesian kinematics matrix  $-M_{\phi(\mathbb{X})}^1$  also called  $D$ -matrix, ii) and the differential joint kinematic matrix  $M_{\phi(q)}^1$  also called  $B$ -matrix.

### ii) Inverse Differential Kinematic Model (IDKM)

This model gives the speed of the joint variables, given the end-effector pose and velocity, and as well as the geometric parameters of the robot:

$$\dot{q} = \frac{\partial M_{I_p}^0(\mathbb{X}, \xi_{geo})}{\mathbb{X}} L_{\mathbb{X}} \zeta \quad (2.6)$$

or equivalently,

$$\dot{q} = M_{I_p}^1(\mathbb{X}, \xi_{geo})\zeta \quad (2.7)$$

where  $M_{I_p}^1$  is the inverse differential kinematic model of a parallel robot.

### iii) Forward Differential Kinematic Model (FDKM)

This model gives the velocity of the end-effector pose, given the positions and speeds of the joint variables and as well as the geometric parameters of the robot:

$$\zeta = L_{\mathbb{X}}^{-1} \frac{\partial M_{F_p}^0(q, \xi_{geo})}{\partial q} \dot{q} \quad (2.8)$$

or equivalently,

$$\zeta = M_{F_p}^1(q, \xi_{geo})\dot{q} \quad (2.9)$$

where  $M_{F_p}^1$  is the forward differential kinematic model of a parallel robot.

## 2.6.2 Singularity analysis

In some configurations, the robot cannot be fully controlled (either too rigid or without stiffness). Such configurations are called singular configurations and they limit the performances of the parallel manipulators. Singularities lead either to a loss of the controllability and/or to a degradation of the natural stiffness of the manipulators. The singularities analysis in parallel manipulators has been raising considerable attention [120]. Most parallel robots are adversely affected by the presence of singular configurations in their workspace which limit their performances. Singularity analysis, in the case of parallel robots, is much more difficult than in the case of serial robots, since such mechanisms contain unactuated joints and usually these joints have more than one DoF.

Thus, from (2.5) the implicit differential kinematic model can be expressed by:

$$D\zeta = B\dot{q} \quad (2.10)$$

where  $B$  is a matrix that represents the direct power developed by the actuators (active joints) which are considered in the movement of the platform, and  $D$  is the matrix which represents all the actions transmitted by the actuators directly to the platform.

Gosselin and Angeles suggested a classification of singularities for parallel manipulators into three main groups associated with the singularity of square matrices such as  $D$  and  $B$  above [62]. Later, Zlatanov gave a more comprehensive study of the singularities of closed-loop mechanisms including configurations where the matrices  $D$  and  $B$  are not square [194, 195]. Thus, depending on which of  $B$ ,  $D$  or both is singular, the robot has three types of singularity as detailed below.

- a) ***D* is singular**- Also called parallel singularity or singularity by direct kinematic or Cartesian singularity [6], this first singularity occurs when the following condition is satisfied:

$$\det(D) = 0 \text{ and } \det(B) \neq 0$$

The physical interpretation of this kind of singularity is that even if all of the input velocities are zero, there are still be instantaneous motion of the platform. In this configuration, the platform loses stiffness and becomes uncontrollable. This kind of singularity is located inside the workspace of the manipulator. Such a singularity is only identified by a thorough analysis and expansion on the equation  $\det(D) = 0$ .

- b) ***B* is singular**- Also called serial singularity or singularity by inverse kinematic or joint-space singularity [6], this second singularity occurs when the following condition is satisfied:

$$\det(D) \neq 0 \text{ and } \det(B) = 0$$

Such a singularity corresponds to the limit of the workspace.

- c) ***B* and *D* are singulars**- The third kind of singularity occurs when:

$$\det(D) = \det(B) = 0$$

Such a singularity corresponds to the first and second type of singularity occurring simultaneously. This singularity is both configuration and architecture dependent.

Parallel singularities are particularly undesirable because they cause the following problems:

- i) an increase of the mechanism stiffness and consequently an increase of the forces in the joints and links that may damage the structure,
- ii) a decrease of the mechanism stiffness which leads to uncontrolled motions of the platform though actuated joints are locked. This singularity is the most dangerous from the point of view of the power laser steering inside of the laryngeal cavity.

### 2.6.3 Performance evaluation

Together with the workspace (which is an important design criterion), the transmission quality index is another important criterion. The transmission quality index couples velocity and force transmission properties of a parallel robot. It is formally defined as:

$$T = \frac{\|E\|}{\|J\| \cdot \|J\|^{-1}}$$

where  $E$  is the identity matrix. We have  $0 < T < 1$ . When  $T=0$  we have a singular pose. The optimal value is  $T=1$  which at the same time stands for isotropy [8].



### 2.6.4 Robot vision control

Control of robots using a vision feedback has been described in [47, 36, 70, 29, 73]. Vision is an efficient way of estimating the end-effector pose and/or joint variables states in robotics. This point of view is interesting for the control of parallel mechanisms, as shown in several cases by Andreff [6, 16, 15, 131, 38]. Vision feedback technique is useful when installing sensors inside the structure can increase the uncertainty of the measure, increase the disturbance influence, or is even impossible.

Some reasons to use vision in robotics were explained in [148], they are summarized below:

- vision sensors are exteroceptive sensors: they provide an information of the interactions of the robot with its environment,
- vision sensors are contactless: they do not impact on the robot dynamics,
- vision sensors are versatile. Depending on the processing of the received information, different information can be issued for a same hardware configuration.
- vision sensors are inexpensive sensor, whose performance in terms of resolution and miniaturization are changing dramatically, for instance miniature VGA cameras (Mizumi) are available for a few hundreds euros.

In microrobotics, the utilization of vision is fully appropriate since the use of sensors such as encoders or potentiometer is difficult or impossible.

Vision-based robot control comes under two fundamental configurations, as shown in Figure 2.26. These two configurations are based on the relative localization of the camera and the robot end-effector [29].

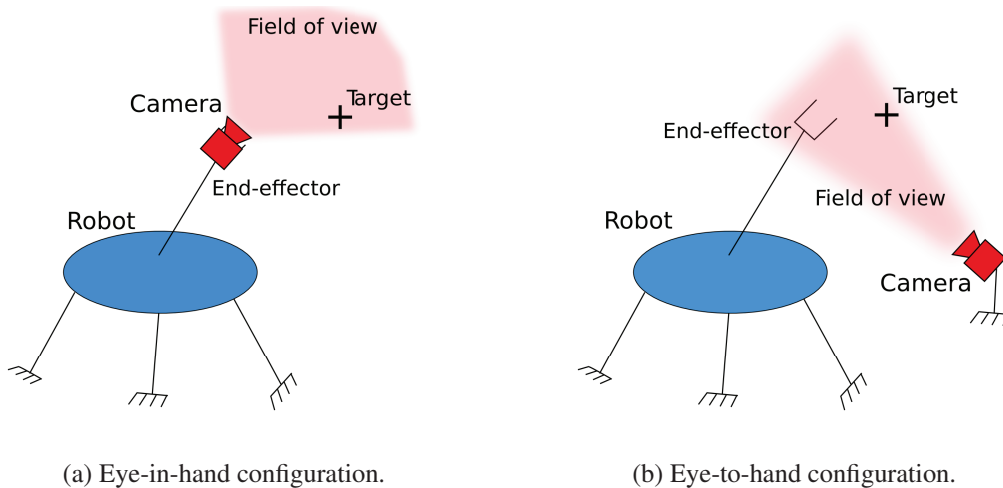


FIGURE 2.26: Two fundamental configurations based on the relative localization of the camera and the robot end-effector.

- Eye-in-hand: where the camera is attached to the moving end-effector and observing the relative position of the target, as shown in Figure 2.26a.
- Eye-to-hand: where the camera is fixed in the same reference system as the base of the robot. The camera observes both the target and the motion of the robot end-effector, as shown in Figure 2.26b.

Robustness of vision-based robot control was investigated in [46, 85, 101, 110]. The authors proved the effectiveness of visual-based robot control over others methods, they also concluded that the global stability is achieved even in presence of errors due to the calibration or unawareness of parameters that can affect the robot model.

In the kinematic control of robots there are many strategies. The so-called model-based control strategies make use of the zero<sup>th</sup> order model of the robot. Regarding Cartesian control of parallel robots, the forward kinematic model (FKM) is used in the feedback loop, as depicted in Figure 2.27. Therefore, if the model is not accurate enough (formally incorrect, simplified or simply poorly calibrated) then the estimation of the pose of the end-effector will be biased, thereby generating positioning errors. Additionally, in the case of PKM, the trouble is even worse, since the FKM can have several solutions. Usually, the estimation of the pose depends strongly on the geometry and contrary to conventional robotics, in microrobotics the geometric tolerances corresponds to a considerable percentage of the whole size. Thereby, those tolerances can importantly increase the errors in the estimation of the pose from the FKM.

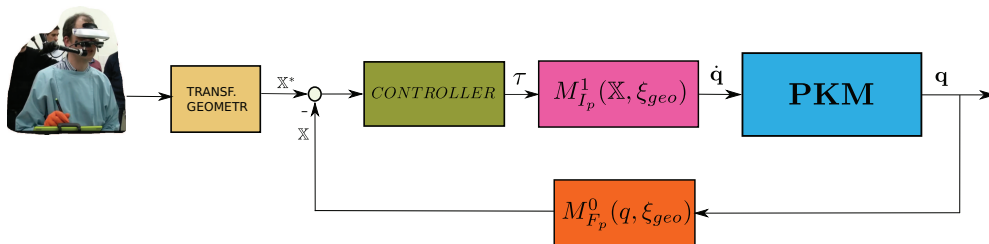


FIGURE 2.27: Model-based Cartesian control of parallel robots.

Regarding vision based control, the reference signal is an image which represents the Cartesian variables to control, as depicted in Figure 2.28. One can remark, that the control scheme does not involve any zero<sup>th</sup> order model at all. Therefore, mis-modelling or mis-calibration will only result in velocity errors that will be compensated by the closed-loop. Thereby, the control accuracy is almost uniquely dependent on the sensor accuracy.

The potential drawback of sensor based control is the definition of the control reference. In practice, it is usually defined by “teaching”, i.e., recording the desired signal ( $s^*$ ). In the context of this thesis, this feature is extremely interesting since the surgeon has the ability, through the surgeon robot interface to directly draw the reference in the image.

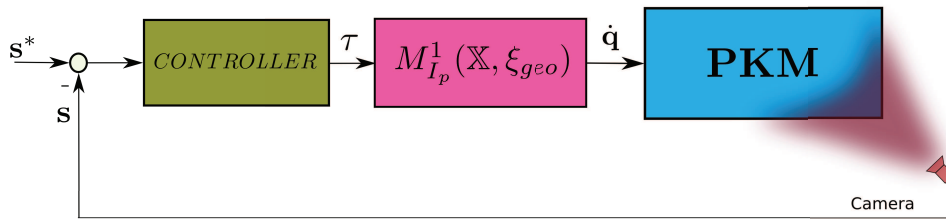


FIGURE 2.28: Vision based control of parallel robots.

## 2.7 Laser systems

### 2.7.1 Definitions

A laser<sup>6</sup> is a light emitted (electromagnetic radiation) through a process of optical amplification based on the stimulated emission of photons [162]. Laser light is remarkable for its high degree of spatial and temporal coherence<sup>7</sup> [31]. Its spatial coherence is relative to its few diffraction i.e. a laser beam can be focused in small spots and its temporal coherence is relative to the large distance that it can travel.

Most so-called “single wavelength” lasers actually produce radiation in several modes having slightly different frequencies (wavelengths), often not in a single polarization. There are lasers that emit a broad spectrum of light, or emit different wavelengths of light simultaneously. Some non single spatial mode lasers diverge more than the requirement. Most of them are visible lasers. Consequently the divergence of power lasers (invisible laser like CO<sub>2</sub> or like Tm:YAG or others) is less than visible lasers (He-Ne).

Lasers have a relatively recent contribution in laryngeal surgery. The benefits of lasers in laryngeal surgery have offered a time- and cost-efficient alternative to others surgical techniques. For that, lasers are used in the treatment of numerous laryngeal pathologies. However, lasers can damage the healthy tissue adjacent to the treated zone and can also produce scares on the vocal folds. These problems can be minimized through understanding the mechanisms by which lasers function and correctly manipulating the parameters under a surgeon’s control. By varying the fluency, the power density, the spot position, and the pulsation (by PWM), tissue damage can be decreased and lasers can be used with more confidence. The various types of lasers and their applications to the treatment of specific pathologies are reviewed below.

### 2.7.2 CO<sub>2</sub> laser

This laser was incorporated into the medical community with an emphasis on its potential capability to remove cancerous lesions. CO<sub>2</sub> laser is easily absorbed by water and with its 10600 nm

<sup>6</sup>The term “laser” is an acronym for Light Amplification by Stimulated Emission of Radiation.

<sup>7</sup>Coherence means that they have a constant phase difference.

wavelength, biological tissue responds well to its excitation [190, 139]. In addition, its continuous wave has a high output power, i.e. by using an appropriate focus system, its beam on a small area makes it adequate for clean and fast surgeries. Typically, the mirrors for this kind of laser are coated with silver or gold [178]. Gold coated mirrors have a wide usage in high power CO<sub>2</sub> laser systems because of its low absorption coefficient and high resistance to thermal shock. On the other hand, windows and lenses are made of either Germanium or Zinc Selenide that is a chemically vapor deposited material commonly used in thermal imaging, forward-looking infrared imaging systems, and medical systems. Lens materials are relatively soft materials which can be easily scratched and they are not recommended for use in harsh environments or in contact with any other surfaces [128]. Therefore, lenses are very delicate for handling, mounting, and cleaning<sup>8</sup>. These lenses are available over 17 mm of diameter. Mirrors and lenses for CO<sub>2</sub> laser are described in [79, 102, 44].

### 2.7.3 Thulium YAG laser

Holmium-chromium thulium triple-doped YAG (Ho:Cr:Tm:YAG, or Ho,Cr,Tm:YAG) is an active laser medium material with high efficiency. Its wave is about 2097 nm and it is widely used in military applications, medicine, and meteorology. The wavelength of thulium-based lasers is very efficient for superficial ablation of tissue, with minimal coagulation depth in air or in water [182]. This makes thulium lasers attractive for laser-based surgeries. Usually, lenses are made of sapphire which is a cheap material, easy to manufacture [11, 129].

### 2.7.4 Femto-second laser

In optics, an ultrashort pulse of light is an electromagnetic pulse whose time duration is in the order of a femto-second ( $10^{-15}$  second) or less. Such pulses have a broadband optical spectrum, and can be created by mode-locked oscillators. They are commonly referred to as ultrafast events. Amplification of ultrashort pulses always requires the technique of chirped pulse amplification in order to avoid damage to the gain of the amplifiers [184, 66, 115, 37, 21].

Femto-second laser is characterized by a high peak intensity that usually leads to nonlinear interactions in various materials, including air. Interactions between femto-second laser and other materials are studied in the field of nonlinear optics. In [17], an endoscopic system with a device that uses a precise femto-second laser to ablate surfaces of vocal folds has been proposed.

### 2.7.5 Safety and classes of lasers

Lasers have been classified according to their potential danger. There are four classes [78].

- Class 1: these lasers do not pose risk because they are completely inserted in a housing (e.g. CD player).
- Class 2: these lasers emit wavelengths in the visible zone of the spectrum with low power density and do not represent risk (e.g. Helium-Neon laser pointers).

<sup>8</sup>To manipulate these lenses the operator must apply uniform pressure when handling and he/she should wear latex finger cots or gloves to prevent contamination. Furthermore, tweezers or other tools should not be used.

- Class 3a: these lasers represent a danger for the eye when the reflected lasers are in a focused laser spot.
- Class 3b: they represent a high danger even regardless the lens system used.
- Class 4: they are very hazardous to the eye, from the direct or reflected laser beams.

Medical lasers are classified in classes 3b and 4.

## 2.8 Synthesis and our proposition

Several topics have been involved to the development of a microrobot intended to laser phonomicrosurgery. They have included medical robotics, microdevices, microfabrication techniques, actuators compatibles with microfabrication, parallel structures, compliant mechanisms and laser technologies.

A synthesis of the current state-of-the-art of the existing microdevices discussed in the previous sections is presented below:

- currents microplatforms are planar devices which are limited to 2D and/or  $2^{1/2}D$ ,
- the ranges of the developed angles are not enough to satisfy the  $\mu$ RALP specifications,
- in cases where the angles are large enough, there exists others issues such as: either high working temperatures or low bandwidth or non-biocompatibility.

The analysis of the state-of-the-art yields that the existing developments do not satisfy the whole specifications imposed in the  $\mu$ RALP project. Thereby, a new microplatform which should be able to rotate with high range of angles, to have a high working bandwidth, to be pack-ageable, and to be biocompatible needs to be developed following the specification of  $\mu$ RALP project.

The survey of microdevices shows that most of the microplatforms are built in two dimensions and works in two  $^{1/2}$  dimensions. Those microplatforms are forced to bend out of the plane to accomplish their tasks, forcing the materials to their limits of fatigue, of rupture and decreasing their lifetime. Our proposition regarding this point is to use the SCM fabrication technique which gives a way to build structures capable to perform large angles according with the specification. SCM proposes to combine: thin carbon fiber sheets with very thin polyimide sheets, in a flat structure which is afterwards folded to yield a 3D structure. Currently SCM has been used to build mobile robots (MAVs and walking robots). Our proposition is to use this fabrication technique to build parallel kinematic machines with millimeter scale.

Moreover, the severe performances demanded in the specifications, such as a minimal bandwidth of 200 Hz and a high scanning resolution better than 100  $\mu$ m, make us design a novel structure and architecture of actuation. The chosen actuator must be capable to ensure such performances. Based on Table 2.2, piezoelectric materials are the most appropriate to construct part of the actuators for the proposed microplatform. We propose to employ cantilever structures for these actuators (piezoelectric cantilevers) because of the high displacements and high dynamics generated by them. Bimorph piezoelectric cantilevers have been particularly chosen as they can yield relatively high force density, with, in the same time, a simple electrical wiring.

# Kinematic Analysis

*This chapter deals with the description and analysis of the two parallel kinematic mechanisms that are proposed and which are called PiBot and Micro Agile-eye. The first section describes first our motivation to choose their structures. The next two sections are devoted to the kinematic modeling of each of the two Parallel Kinematic Machines (PKMs). The kinematic model and analysis of both structures are carried out by using Screw Theory which permits to perform the velocity and the singularity analysis. Finally, the last section is devoted to the optical-kinematics modeling.*

## Chapter contents

---

<b>3.1</b>	<b>Introduction</b>	<b>56</b>
<b>3.2</b>	<b>Proposals for microrobot structure</b>	<b>56</b>
<b>3.3</b>	<b>Theoretical background</b>	<b>57</b>
3.3.1	Screw Theory	57
<b>3.4</b>	<b>Modeling the Micro Agile-Eye</b>	<b>62</b>
3.4.1	Amplifier based on lever-principle	62
3.4.2	Agile Eye: Spherical 2-DoF 5R PKM	64
3.4.3	Docking mechanism	66
3.4.4	Complete Micro Agile Eye	67
<b>3.5</b>	<b>Modeling the PiBot</b>	<b>67</b>
3.5.1	Inverse kinematics	68
3.5.2	Instantaneous kinematics	69
<b>3.6</b>	<b>Optical model</b>	<b>71</b>
3.6.1	Basic background on reflective optics	71
3.6.2	Kinematics	74
3.6.3	Instantaneous Kinematics	75
<b>3.7</b>	<b>Conclusion</b>	<b>76</b>

---

### 3.1 Introduction

Large rotations, high resolution and high bandwidth are a challenge in manufacturing micromechanisms working in static mode (see Section 2.3). To reach these objective, the choice of piezoelectric actuators has been a key. The other choice to take is: *what kind of mechanical structure has to be chosen?* For that reason, two ways have been considered and consequently two mechanical structures have been proposed. This choice is explained in Section 3.2. After the choice of the mechanical structures, we will focus on their kinematic analysis in Sections 3.4 and 3.5 respectively. After that, the kinematic model of the laser beam between the surface of the mirror (onto the platform of the microrobot) and the projected spot (onto a screen) is described in Section 3.6. Finally, a conclusion is drawn.

### 3.2 Proposals for microrobot structure

This section discusses the choice of the two parallel kinematic machines that have been selected for the project. The kinematics of these two structures are analyzed in the next sections. Then, their fabrication will be presented in the next chapter.

The selection of the actuators is very important before deciding the mechanical structure of the microrobot. Thus, first the material and the morphology of the actuators is described below. Then the two mechanical structures proposed are described.

#### A) Actuator:

Piezoelectric cantilever were chosen as actuators. The choice was based on the nanometric resolution and the high efficiency that piezoelectric materials can provide. We discard others arrays such as Inch-Worm, Impact-Drive or Stick-Slip, to preserve the high dynamics (bandwidth) that piezoelectric materials can furnish. Cantilever morphology was chosen based on the displacement better than of piezostacks. Among piezoelectric materials, we use the Lead Zirconate Titanate (PZT) which is a ceramic piezoelectric material. PZT usually has a low cost and is widely available compared to other piezoelectric materials. Also PZT exhibits large piezoelectric coefficients and large stiffness which make PZT cantilevers well adapted for actuation. Moreover they have been extensively studied and used in many successful applications. In Appendix A, we give a description of piezoelectric cantilevers actuators.

#### B) The mechanical structure:

- i) The first choice consists in amplifying the displacement generated by the piezoelectric cantilever actuator using a lever effect combined with a serial disposition to generate the large displacement. Then, a standard kinematic structure such as the “Agile-Eye 5R-2DoF” [63] is used to transform the displacements of the actuators into two rotations. The complete proposition is evidenced in Figure 3.1a. This microrobot, named “Micro-Agile-Eye”, is described in Section 3.4.
- ii) The second choice consists in directly amplifying the displacement by conveniently designing the structure and its size. A 2-DoF structure “2RUS” with simple piezoelectric

cantilevers as actuators is proposed. The complete proposition is evidenced in Figure 3.1b. This microrobot, named “PiBot”, is described in section 3.5.

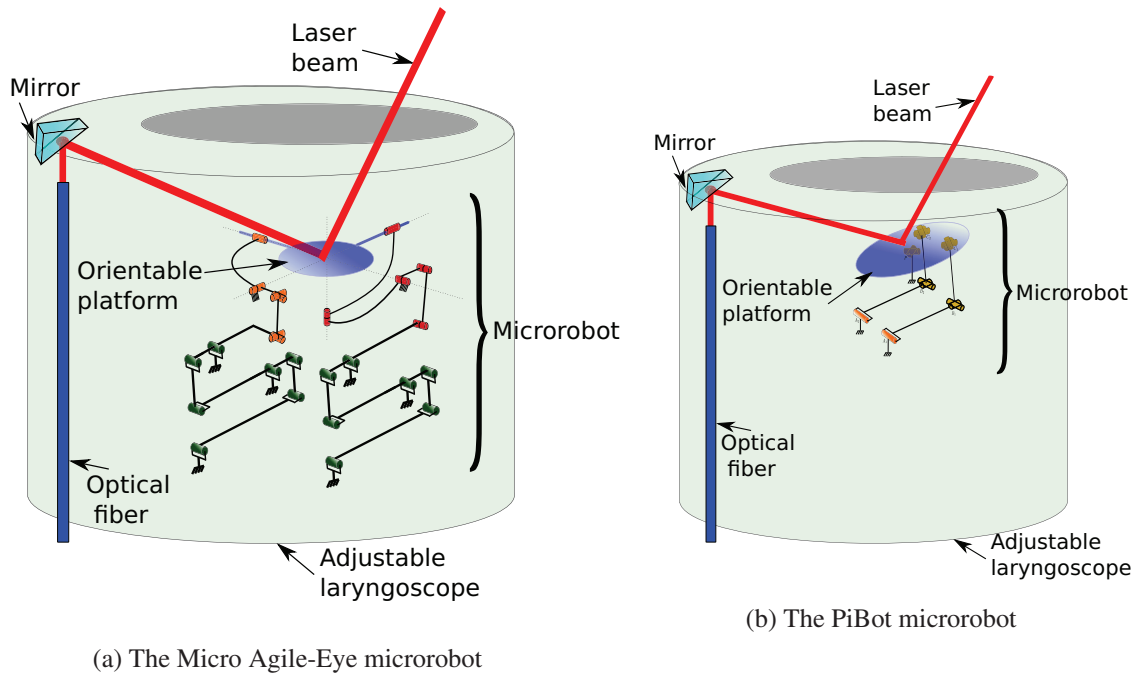


FIGURE 3.1: Proposed microrobots placed at the head of the adjustable laryngoscope driving a laser beam. (a) Micro Agile-Eye: a microrobot using amplification system made of three cantilevers per leg and a standard kinematic structure. (b) PiBot: a microrobot using a unique piezoelectric cantilever per leg and amplification made by appropriate connection onto the platform.

### 3.3 Theoretical background

Before starting with the kinematic analysis which will be useful for the controller design in Chapter 5, we first briefly give some preliminaries on screw theory used in the analysis of parallel kinematics.

#### 3.3.1 Screw Theory

Screw theory is basically a geometric method used to combine linear and rotational motion in only one mathematical expression. Screw theory is based on the principles of motion. It is simpler when it is compared with other methods such as algebraic or numerical methods. One limitation of the screw theory method is that it is only based on instantaneous kinematics. The time variable is not explicated in screw theory, which can bring advantages or disadvantages



according to what kind of analysis we need to perform. The preliminaires presented here are based on [76, 180, 24, 96].

### A) Screws

A normalized or unit screw as shown in Figure 3.2 is defined by a pair of vectors:

$$\mathcal{S} = \begin{bmatrix} a \\ b \\ c \\ d \\ e \\ f \end{bmatrix} = \begin{bmatrix} \mathbf{s} \\ \mathbf{s} \times \mathbf{r} + h\mathbf{s} \end{bmatrix} \quad (3.1)$$

where  $\mathbf{s}$  is a unit vector indicating the direction of the screw axis,  $\mathbf{r}$  is any vector between the screw axis and the origin of the reference frame, and  $h$  is the pitch (relation rotation/translation) of the screw.

The two particular cases are when the pitch is zero (pure rotation) and when the pitch is infinite (pure translation):

$$\mathcal{S} = \begin{cases} \begin{bmatrix} \mathbf{s} \\ \mathbf{s} \times \mathbf{r} \end{bmatrix}, & \text{if } h = 0 \\ \begin{bmatrix} \mathbf{0} \\ \mathbf{s} \end{bmatrix}, & \text{if } h = \infty \end{cases} \quad (3.2)$$

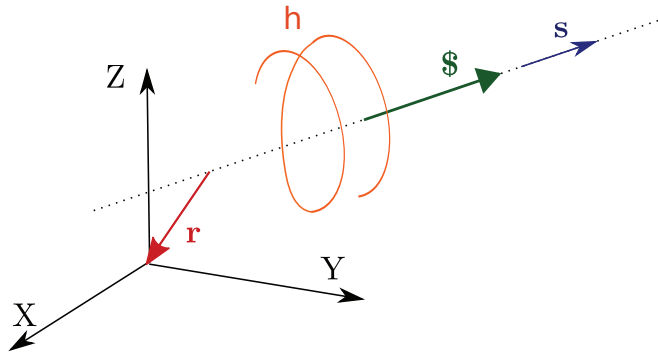


FIGURE 3.2: A Screw.

### B) Reciprocal screws

Let  $\mathcal{S}_1$  and  $\mathcal{S}_2$  be two unit screws. The reciprocal product (operator  $\circ$ ) between  $\mathcal{S}_1$  and  $\mathcal{S}_2$  is defined as:

$$\begin{aligned} \mathcal{S}_1 \circ \mathcal{S}_2 &= \begin{bmatrix} \mathbf{s}_1 \\ \mathbf{s}_1 \times \mathbf{r}_1 + h_1 \mathbf{s}_1 \end{bmatrix} \circ \begin{bmatrix} \mathbf{s}_2 \\ \mathbf{s}_2 \times \mathbf{r}_2 + h_2 \mathbf{s}_2 \end{bmatrix} \\ &= (\mathbf{s}_1) \cdot (\mathbf{s}_2 \times \mathbf{r}_2 + h_2 \mathbf{s}_2) + (\mathbf{s}_2) \cdot (\mathbf{s}_1 \times \mathbf{r}_1 + h_1 \mathbf{s}_1) \end{aligned} \quad (3.3)$$

Two screws,  $\mathcal{S}_1$  and  $\mathcal{S}_2$ , are said to be reciprocal whether their reciprocal product is equal to zero. Thus, if  $\mathcal{S}_1 \circ \mathcal{S}_2 = 0$  then  $\mathcal{S}_1$  is reciprocal to  $\mathcal{S}_2$  and vice versa.

Usually many references utilize the reciprocity condition in (3.4) which is derived from Figure 3.3:

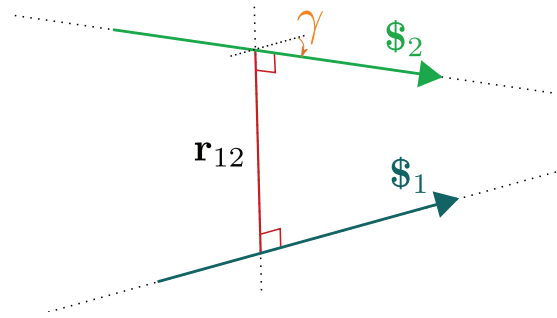


FIGURE 3.3: Reciprocal product of two screws.

$$\mathcal{S}_1 \text{ is reciprocal to } \mathcal{S}_2 \rightarrow \begin{cases} \text{no constraint} & , \text{ if } h_1 \text{ and } h_2 \text{ are } \infty \\ \cos(\gamma) = 0 & , \text{ if } h_1 \text{ or } h_2 \text{ are } \infty \\ (h_1 + h_2)\cos(\gamma) - r_{12}\sin(\gamma) = 0, & \text{ if } h_1 \text{ and } h_2 \text{ are finite} \end{cases} \quad (3.4)$$

where  $r_{12}$  is the offset distance along the common perpendicular leading from the screw axis of  $\mathcal{S}_1$  to  $\mathcal{S}_2$ . The angle  $\gamma$  is the angle between the axes of  $\mathcal{S}_1$  and  $\mathcal{S}_2$ , measured from  $\mathcal{S}_1$  to  $\mathcal{S}_2$ , about the common perpendicular according to the right-hand screw rule.

From (3.4), it is concluded that:

- i) two screws each one with  $h = \infty$  are always reciprocal each other;
- ii) a screw with  $h = \infty$  is reciprocal to a screw with  $h = 0$  if and only if their axes are perpendicular each other;
- iii) two screws with  $h = 0$  are reciprocal each other if and only if they are in the same plane.

### C) Screw systems and reciprocal screw systems

A screw system of order  $n$  ( $0 \leq n \leq 6$ ) comprises all screws which are linearly dependent on  $n$  given linearly independent screws. Reciprocal screws systems can be defined by a given  $n$ -system. There is a unique reciprocal screw system of order  $(6 - n)$  which comprises all screws reciprocal to the original screw system.

**D) Twist and wrench of kinematics chains**

A twist is a screw that represents an instantaneous motion of a rigid body. Its three first components define the angular velocity and its three last components define the linear velocity relative to the reference frame.

A wrench is a screw that represents a system of forces and couples acting on a rigid body. Its three first components define the resultant force and its three last components define the resultant moment about the origin of the reference frame.

The reciprocal product between a twist and a wrench corresponds to the virtual work of the wrench over the twist. If this reciprocal product is zero (the twist is reciprocal to the wrench and vice versa), then the wrench does not realize any virtual work over the twist.

**E) Screws in kinematic analysis**

We give here some screws in basic kinematic structures.

## a) Revolute joint

For a revolute joint (see Figure 3.4a), the unit screw associated is a screw (twist) with zero pitch lying along the joint axis. The associated reciprocal screw to the revolute joint is a 5-system (wrenches), in particular, those zero pitch reciprocal screws which lie on all planes containing the axis of the revolute joint, and those infinity pitch screws whose axes are perpendicular to the joint axis of the revolute joint.

## b) Prismatic joint

For a prismatic joint (see Figure 3.4b), the unit screw associated with a prismatic joint is a screw of infinite pitch pointing along the joint axis. The associated reciprocal screw to the prismatic joint is a 5-system (wrenches), in particular those zero pitch screws whose axes are perpendicular to the joint axis of the prismatic joint and also those with all infinity pitch screws.

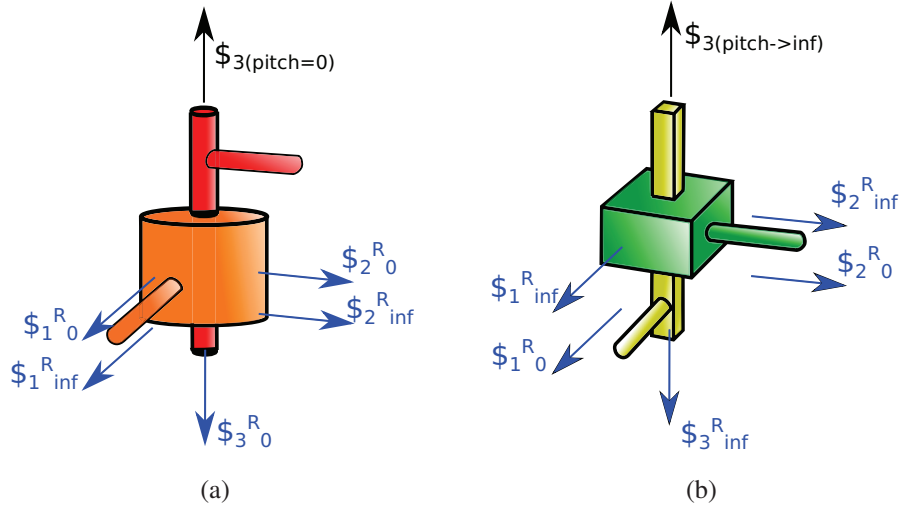


FIGURE 3.4: (a) Revolute joint and its twist and wrenches. (b) Prismatic joint and its twist and wrenches.

c) Universal and spherical joints

An universal joint and a spherical joint can be modeled with the combination of two and three revolute joints respectively.

d) Serial kinematic manipulator

The output twist ( $\xi_s$ ) of the end-effector in a serial kinematic manipulator is the resultant of the contribution of each twist given by each individual joint, as represented in Equation (3.5).

$$\xi_s = \sum_{j=1}^{f=6} \dot{q}_j \rho_j \quad (3.5)$$

where  $\rho_j$  is the twist of the  $j$ -th joint and  $\dot{q}_j$  is its instantaneous velocity, and where  $f$  represents the number of DoF of the serial kinematic chain (for instance  $f = 6$ ) as shown in Figure 3.5a.

e) Parallel kinematic manipulator

The output twist ( $\xi_p$ ) of the moving platform in a parallel kinematic manipulator is the result of the intersection of all resultant twists of all legs of the parallel kinematic manipulator.

$$\xi_p = \xi_s^1 \cap \xi_s^2 \cap \xi_s^3 \quad \text{with} \quad \begin{cases} \xi_s^1 = \sum_{j=1}^{f=6} \dot{q}_j^1 \rho_j^1 \\ \xi_s^2 = \sum_{j=1}^{f=6} \dot{q}_j^2 \rho_j^2 \\ \xi_s^3 = \sum_{j=1}^{f=2} \dot{q}_j^3 \rho_j^3 \end{cases}, \quad (3.6)$$

where  $\xi_s^1$ ,  $\xi_s^2$  and  $\xi_s^3$  are the output twist of each leg respectively, as shown in Figure 3.5b. Individually each leg is a serial kinematic manipulator.

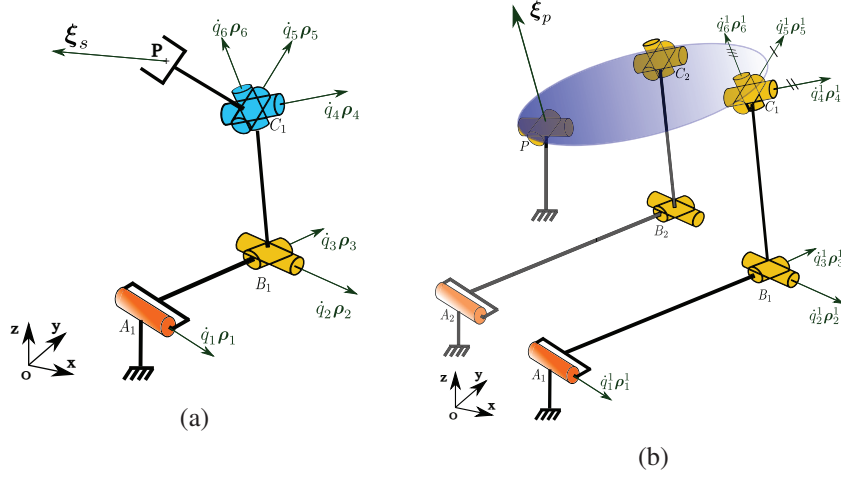


FIGURE 3.5: (a) A Serial Kinematic Chain. (b) A Parallel Kinematic Chain.

### 3.4 Modeling the Micro Agile-Eye

In this section a kinematic analysis is performed to our first proposed structure called “Micro Agile-Eye” as shown in Figure 3.1a. The Micro Agile-Eye is divided into two parts to facilitate its analysis. The first part is devoted to analyze the actuation system which is formed by three piezoelectric cantilevers in each leg. Thus, these three actuators are positioned such that the amplification is performed by using the leverage effect, such as is explained in Section 3.4.1. Then the upper part of the microrobot is the well known 2 DoF Agile Eye structure developed in [63]. This upper part is dedicated to transform the movement generated by the actuation system into two rotations of the platform (end-effector), as explained in Section 3.4.2.

#### 3.4.1 Amplifier based on lever-principle

Consider Figure 3.6. The three piezoelectric cantilever actuators in each leg ( $\overline{D_1^j D_2^j}$ ,  $\overline{D_3^j D_5^j}$  and  $\overline{D_6^j A_j}$  with  $j = 1$  or  $2$  denoting the leg) are independently driven and are disposed in series, as shown in Figure 3.7.

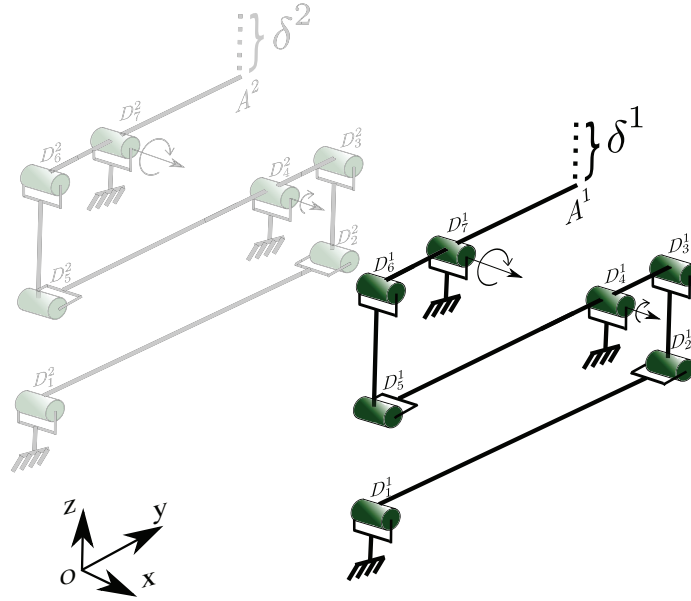


FIGURE 3.6: Kinematic representation of the piezoelectric cantilever actuators and amplification mechanisms by lever effect of the two active legs in the PKM.

To amplify the displacement generated by the lower piezoelectric actuator, a lever effect is introduced using the middle piezoelectric actuator with pivot point at  $D_4^j$ . The same principle is applied to the middle and to the upper piezoelectric actuator with pivot point at  $D_7^j$ . Therefore the final displacement  $\delta_j$  at the point  $A_j$  furnished by the leg is expressed as:

$$\delta^j = C_1 C_2 \delta_1^j - C_2 \delta_2^j + \delta_3^j \quad \text{for } j = 1, 2 \quad (3.7)$$

where  $C_1 = \frac{|D_3^j D_4^j|}{|D_4^j D_3^j|}$  and  $C_2 = \frac{|A^j D_7^j|}{|D_7^j D_6^j|}$  are constants, and where the displacements generated by the actuators  $D_1^j D_2^j$ ,  $D_3^j D_5^j$ , and  $D_6^j A^j$  have been denoted  $\delta_1^j$ ,  $\delta_2^j$ , and  $\delta_3^j$  respectively,

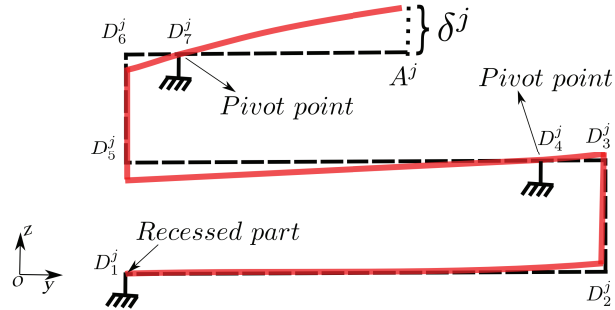


FIGURE 3.7: The system without actuation is shown in black while in red the system is shown after actuation.

To find the instantaneous kinematics of the amplification system, we differentiate equation (3.7) as shown below:

$$\begin{bmatrix} \dot{\delta}^1 \\ \dot{\delta}^2 \end{bmatrix} = \begin{bmatrix} C_1 C_2 & C_1 & 1 & 0 & 0 & 0 \\ 0 & 0 & 0 & C_1 C_2 & C_1 & 1 \end{bmatrix} \begin{bmatrix} \dot{\delta}_1^1 \\ \dot{\delta}_2^1 \\ \dot{\delta}_3^1 \\ \dot{\delta}_1^2 \\ \dot{\delta}_2^2 \\ \dot{\delta}_3^2 \end{bmatrix} \quad (3.8)$$

where  $\delta_i^j$  is the elementary displacement of the  $i$ -piezoelectric cantilevers in the  $j$ -leg and with  $\dot{\delta}_i^j$  denoting its velocity.

### 3.4.2 Agile Eye: Spherical 2-DoF 5R PKM

This standard mechanism which was proposed by C. Gosselin [63] gives as result a platform with only two rotations. We proposed to use it as the upper part of the microrobot. Let us study its kinematics.

The forward kinematics of this structure was investigated in [187]. Recently, a formula has been proposed by X. Kong [97] which produces a unique solution of the forward kinematics for a given set of inputs. An adaptation to our case is shown below.

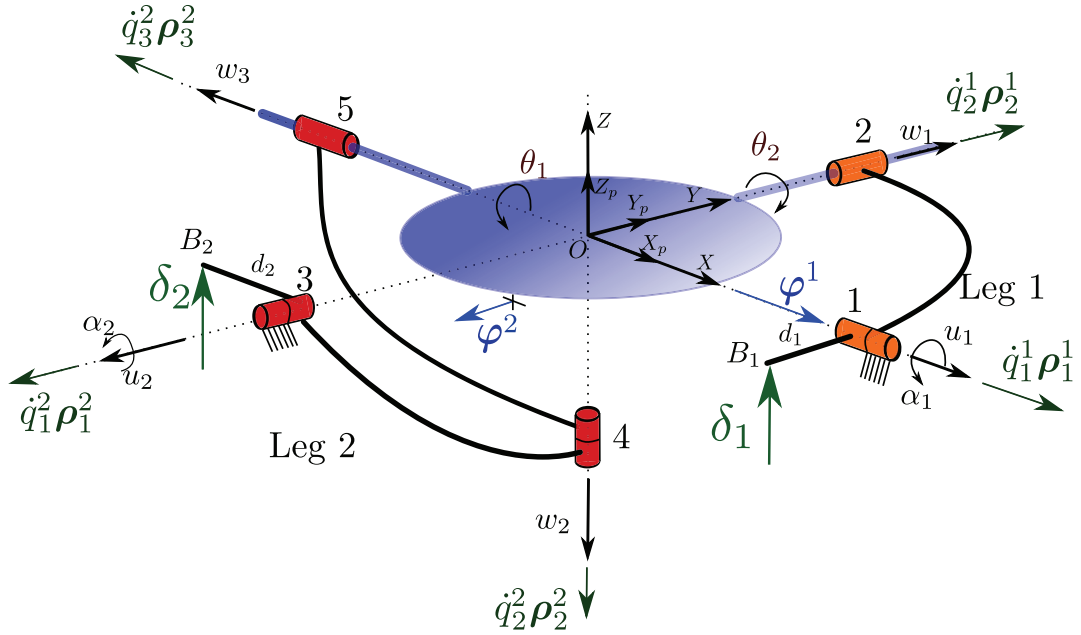


FIGURE 3.8: Kinematic representation of the Agile Eye 2-DoF [63].

From [97] the results of the forward kinematic model (FKM) of the 2 DoF Agile Eye is:

$$\theta_1 = \arctan\left(-\frac{\tan \alpha_2}{\cos \alpha_1}\right) \quad (3.9)$$

$$\theta_2 = \arctan\left(\frac{-\sin \alpha_1 \cos \alpha_2}{\sqrt{1 - (\sin \alpha_1 \cos \alpha_2)^2}}\right) \quad (3.10)$$

where  $\theta_1$  and  $\theta_2$  are the angles developed by the platform about its  $x$  and  $y$ -axes respectively and  $\alpha_1$   $\alpha_2$  are the input angles imposed joints 1 and 2 respectively.

Again, from [97] the inverse kinematic model (IKM) is:

$$\alpha_1 = \arctan\left(-\frac{\tan \theta_2}{\cos \theta_1}\right) \quad (3.11)$$

$$\alpha_2 = \arctan\left(\frac{-\sin \theta_1 \cos \theta_2}{\sqrt{1 - (\sin \theta_1 \cos \theta_2)^2}}\right) \quad (3.12)$$

Then the instantaneous kinematic can be performed using the screw theory. In a first time, the equation of twists is computed as below:

$$\xi = \dot{q}_1^1 \rho_1^1 + \dot{q}_2^1 \rho_2^1 \quad (3.13a)$$

$$\xi = \dot{q}_1^2 \rho_1^2 + \dot{q}_2^2 \rho_2^2 + \dot{q}_3^2 \rho_3^2 \quad (3.13b)$$



Since legs -1 and -2 have 2 and 3 DoF respectively, they impose constraints on the platform. Therefore the possible twists,  $\xi$ , at every configuration are given by (3.13a). When such a well-defined continuously-changing basis exists for the twist system of the platform, the velocity kinematics can be expressed with as few equations as the parallel mechanism's DoF [196].

For each active leg, there is pure force,  $\varphi^j$ ,  $j = 1, 2$ , reciprocal to all second or second and third passive-joint screws in leg 1 and leg 2 respectively.

Taking the reciprocal product of  $\varphi^1$  with (3.13a) and of  $\varphi^2$  with (3.13b), we obtain:

$$\begin{bmatrix} \varphi^1 \cdot \xi \\ \varphi^2 \cdot \xi \end{bmatrix} = \begin{bmatrix} \varphi^1 \cdot \rho_1^1 & 0 \\ 0 & \varphi^2 \cdot \rho_1^2 \end{bmatrix} \begin{bmatrix} \dot{q}_1^1 \\ \dot{q}_1^2 \end{bmatrix} \quad (3.14)$$

we can abbreviated as:

$$B\dot{q} = D\dot{\theta} \quad (3.15)$$

To calculate the output twist of (3.14), we can use:

$$\varphi^1 = \begin{bmatrix} 0 \\ 1 \\ 0 \\ 0 \end{bmatrix}, \quad \rho_1^1 = \begin{bmatrix} 1 \\ 0 \\ 0 \\ 0 \end{bmatrix}, \quad \rho_2^1 = \begin{bmatrix} 0 \\ \cos(\alpha_1) \\ \sin(\alpha_1) \\ 0 \end{bmatrix} \quad (3.16)$$

and

$$\rho_1^2 = \begin{bmatrix} 0 \\ -1 \\ 0 \\ 0 \end{bmatrix}, \quad \rho_2^2 = \begin{bmatrix} \sin(\alpha_2) \\ 0 \\ -\cos(\alpha_2) \\ 0 \end{bmatrix}, \quad \rho_3^2 = \begin{bmatrix} -\cos(\theta_2) \\ -\sin(\theta_1)\sin(\theta_2) \\ \cos(\theta_1)\sin(\theta_2) \\ 0 \end{bmatrix} \quad (3.17)$$

According with Figure 3.8, in leg 1, the two R-joints will never be collinear and for that matrix B will not be singular by the leg 1. In leg 2, the three R-joints will set the matrix B in singular whether they are coplanar. That happens when the joint 4 has 180 or 0°. The analysis when matrix D become singular can be done locking the actuated joints, thus the robot become a structure with three joints (joints 2,4 and 5). The matrix D become singular when the twists of those three joints are linearly dependent, i.e., when joint 5 has 0°. Both singularities require larges displacements and since the PKM workspace is limited to the angles required to scan the vocal folds ( $\pm 12.5^\circ$ ), both B and D are expected nonsingular in such reduced workspace.

### 3.4.3 Docking mechanism

An analysis of the position of the actuator system and the upper part has carried out that the mechanical system which will not block the structure is in one case two simple revolutes joints and for the other leg a double universal-joint is provided.

### 3.4.4 Complete Micro Agile Eye

The Micro Agile Eye microrobot which is the combination of the actuation system and the platform using the docking mechanism is depicted in Figure 3.9

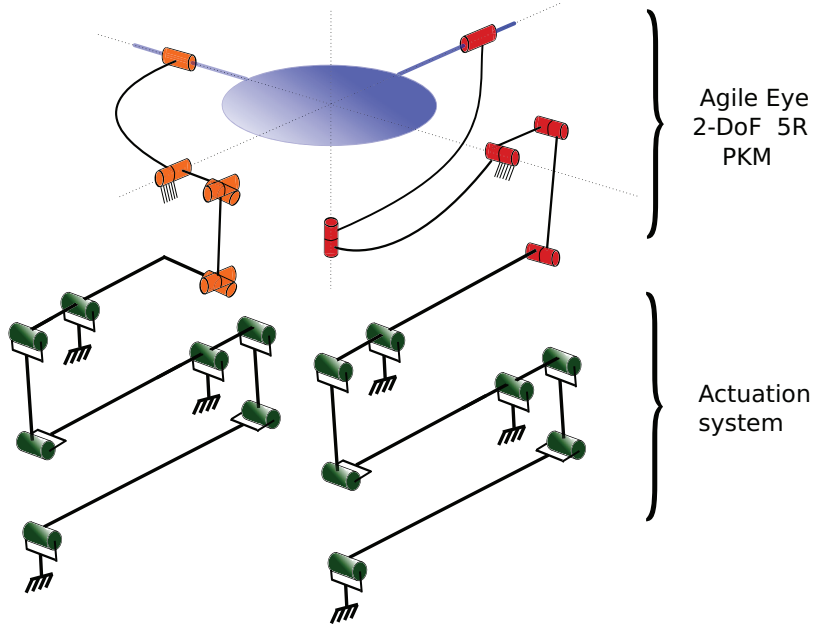


FIGURE 3.9: Micro Agile Eye complete.

## 3.5 Modeling the PiBot

In this section a kinematic analysis of the second proposed structure called “PiBot” is performed. The proposed PKM structure is depicted in Figure 3.10. Despite its simplicity, we have not yet found any publication mentioning this kinematic structure. The orientable platform is used to orient a mirror. As already explained, the PiBot is actuated by one piezoelectric cantilevers in two active legs. The platform is connected to the base (attached to the laryngoscope) by a passive U-joint at  $P$  (leg 3), which constrains it to only tilt and pan. We define the base reference frame  $Pxyz$  with coordinate unit vectors  $\mathbf{i}$ ,  $\mathbf{j}$ ,  $\mathbf{k}$ , and a rotating frame, fixed to the platform, with origin at  $P$  and coordinate unit vectors  $\mathbf{u}$ ,  $\mathbf{v}$ ,  $\mathbf{w}$ , as shown in Figure 3.10.

The 2-DoF platform motion is actuated with two identical 6-DoF RUS legs: leg 1 and leg 2. Piezoelectric actuation is used as the first R-joint of each actuated leg, i.e., the piezoelectric cantilever is assumed to be a rigid rod rotating about a fixed axis. The two active joints have a common axis,  $A_2A_1$ , with unit vector  $\mathbf{k}_1 = \sqrt{2}/2\mathbf{i} - \sqrt{2}/2\mathbf{j}$ . Point  $A_i$  is the projection of the U-joint center  $B_i$  on this axis.

In each active leg, the axis of joint 2, the first joint of the passive U-joint centered at  $B_i$ ,  $i = 1, 2$ , is parallel to  $A_1A_2$ , while the center  $C_i$  of the spherical joint is along the common perpendicular of the U-joint axes.

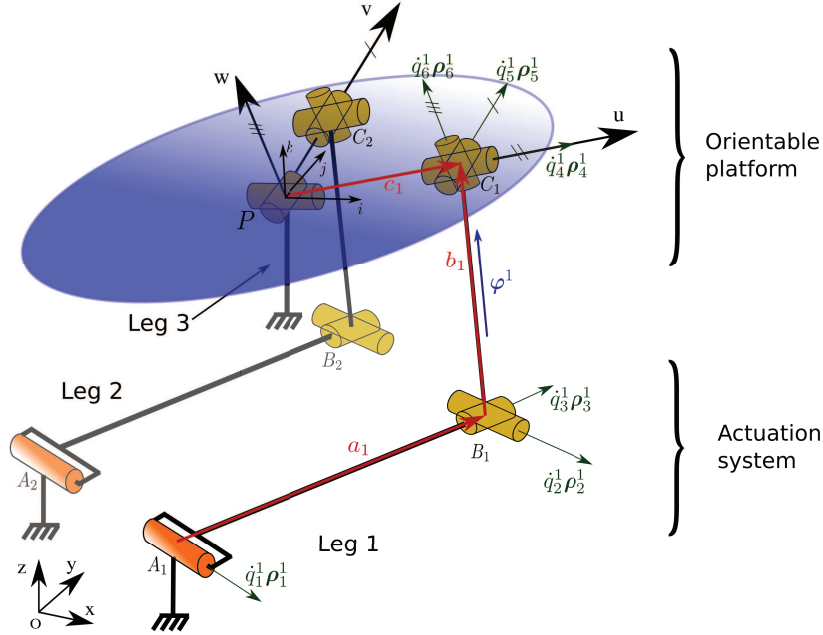


FIGURE 3.10: Platform operated in parallel by two active legs and constrained by an unactuated U-joint leg.

At the reference configuration, when the angles of the U-joint at  $P$  are  $\theta_1 = \theta_2 = 0$ , we have  $\mathbf{c}_1 = \overrightarrow{PC_1}$  parallel to  $\mathbf{u} = \mathbf{i}$  and  $\mathbf{c}_2 = \overrightarrow{PC_2}$  parallel to  $\mathbf{v} = \mathbf{j}$ . Moreover, at the zero configuration, the distal links,  $B_i C_i$ , are parallel to the  $z$  axis, while the proximal links,  $A_i B_i$ , are perpendicular to it and at equal angles with the  $x$  and  $y$  axes.

The dimensions of the PKM are given by  $|A_i B_i| = 20l$  (corresponding to the piezoelectric cantilever actuator),  $|B_i C_i| = 2l$  and  $|P C_i| = l$ , where  $l = 0.5$  mm. The distance between  $Pz$  and the common actuated-joint axis,  $A_1 A_2$ , is  $(20 - \frac{\sqrt{2}}{2})l$ , while points  $A_1$  and  $A_2$  are at  $\sqrt{2}l$  from each other. Therefore,

$$\begin{aligned} \overrightarrow{PA_1} &= -(10\sqrt{2} - 1)li - 10\sqrt{2}lj - 2lk \\ \overrightarrow{PA_2} &= -10\sqrt{2}li - (10\sqrt{2} - 1)lj - 2lk \end{aligned} \quad (3.18)$$

### 3.5.1 Inverse kinematics

Given a feasible platform orientation defined by the values of the passive-leg U-joint angles  $(\theta_1, \theta_2)$ . The mechanism configuration can be calculated by finding the intersection of a sphere centered at the point  $C_i$ ,  $i = 1, 2$ , with radius  $|B_i C_i|$  and the circle of center  $A_i$  with radius  $|A_i B_i|$ , in a plane normal to line  $A_1 A_2$ . In general, there are four solutions of the inverse kinematics. Points  $C_i$  are obtained as:

$$\overrightarrow{PC_1} = l\mathbf{u} = c_2l\mathbf{i} + s_1s_2l\mathbf{j} - c_1s_2l\mathbf{k} \quad (3.19)$$

$$\overrightarrow{PC_2} = l\mathbf{v} = c_1l\mathbf{j} + s_1l\mathbf{k} \quad (3.20)$$

where  $c_1 = \cos \theta_1$  and  $s_1 = \sin \theta_1$ . Indeed, the platform orientation is given by

$$R(\theta_1, \theta_2) = R_x(\theta_1)R_y(\theta_2) = \begin{bmatrix} c_2 & 0 & s_2 \\ s_1s_2 & c_1 & -s_1s_2 \\ -c_1s_2 & s_1 & c_1c_2 \end{bmatrix} \quad (3.21)$$

On the other hand, we have  $\overrightarrow{B_jC_j} = \overrightarrow{A_jC_j} - \overrightarrow{A_jB_j}$ , and thus:

$$|\overrightarrow{B_jC_j}|^2 = 4l^2 = |\overrightarrow{A_jC_j}|^2 + 400l^2 - 2\overrightarrow{A_jC_j} \cdot \overrightarrow{A_jB_j} \quad (3.22)$$

where  $\overrightarrow{A_jB_j} = 10l(\sqrt{2}c_1^j\mathbf{i} + \sqrt{2}c_1^j\mathbf{j} + 2s_1^j\mathbf{k})$ , in which  $c_i^j = \cos q_i^j$  and  $s_i^j = \sin q_i^j$ . Using (3.18)–(3.20) and (3.22) it is now possible to obtain a linear equation in term of  $c_1^j, s_1^j$ :

$$F_jc_1^j + G_js_1^j = H_j \quad (3.23)$$

where  $F_j, G_j$ , and  $H_j$  depend only on  $\theta_1, \theta_2$ , resulting in two solutions for  $q_1^j$ .

For instance, when choosing  $\theta_1 = 15^\circ$  and  $\theta_2 = -15^\circ$ , the solutions for  $(q_1^1, q_1^2)$  are:

$$\begin{aligned} & (0.720102952001288^\circ, 0.742258398498497^\circ) \\ & (0.720102952001288^\circ, 12.160623836841685^\circ) \\ & (12.16311819616120381^\circ, 0.742258398498497^\circ) \\ & (12.16311819616120381^\circ, 12.160623836841685^\circ) \end{aligned} \quad (3.24)$$

where only the first solution is feasible by the piezoelectric cantilevers proving that this extreme required position the is achievable with the proposed actuators.

### 3.5.2 Instantaneous kinematics

The velocity analysis is now performed using screw theory.

On a PKM the instantaneous twist,  $\xi$ , of the platform with respect to the ground can be expressed as a linear combination of the joint screws of leg  $j$  [121]. Denoting by  $\dot{q}_i^j$  and  $\rho_i^j$  the amplitude and the unit zero-pitch twist associated with the  $i^{\text{th}}$  joint of the  $j^{\text{th}}$  leg, we have:

$$\xi = \dot{q}_1^1\rho_1^1 + \dot{q}_2^1\rho_2^1 + \dot{q}_3^1\rho_3^1 + \dot{q}_4^1\rho_4^1 + \dot{q}_5^1\rho_5^1 + \dot{q}_6^1\rho_6^1 \quad (3.25a)$$

$$\xi = \dot{q}_1^2\rho_1^2 + \dot{q}_2^2\rho_2^2 + \dot{q}_3^2\rho_3^2 + \dot{q}_4^2\rho_4^2 + \dot{q}_5^2\rho_5^2 + \dot{q}_6^2\rho_6^2 \quad (3.25b)$$

$$\xi = \dot{\theta}_1\rho_1^3 + \dot{\theta}_2\rho_2^3 \quad (3.25c)$$

Since legs 1 and 2 have 6 DoF they does not impose any constraint on the platform. Therefore the possible twists  $\xi$  at every configuration are given by (3.25c) as any linear combination of the passive leg's two revolute-joint unit twists  $\rho_1^3$  and  $\rho_2^3$ . When such a well-defined

continuously-changing basis exists for the twist system of the platform, the velocity kinematics can be expressed with as few equations as the parallel mechanism's DoF [196]. For this, one can first substitute (3.25c) into (3.25a) and (3.25b), and then eliminate the passive joint velocities using reciprocal screws obtaining a system of two equations relating the platform angular speeds  $\dot{\theta}_1$  and  $\dot{\theta}_2$  with the input velocities  $\dot{q}_1^1$  and  $\dot{q}_1^2$ .

For each active leg, there is a unit pure force  $\varphi^j$ ,  $j = 1, 2$ , reciprocal to all five passive-joint screws. Its axis passes through the centers of the leg's U- and S-joints.

Remark: In a leg-singular configuration, where the center of the spherical joint is in the plane of the U-joint, there will be a whole pencil of concurrent planar forces with this property, and two, rather than one, reciprocal screws for that leg must be used to obtain the input-output velocity equations. We will assume that such leg postures do not occur during the operation of the mechanism.

Taking the reciprocal product of  $\varphi^1$  with (3.25a) and of  $\varphi^2$  with (3.25b), we obtain:

$$\begin{bmatrix} \varphi^1 \cdot \rho_1^3 & \varphi^1 \cdot \rho_2^3 \\ \varphi^2 \cdot \rho_1^3 & 0 \end{bmatrix} \begin{bmatrix} \dot{\theta}_1 \\ \dot{\theta}_2 \end{bmatrix} = \begin{bmatrix} \varphi^1 \cdot \rho_1^1 & 0 \\ 0 & \varphi^2 \cdot \rho_1^2 \end{bmatrix} \begin{bmatrix} \dot{q}_1^1 \\ \dot{q}_1^2 \end{bmatrix} \quad (3.26)$$

In (3.26), the term  $\varphi^2 \cdot \rho_2^3$  is zero because the joint-2 axis of the passive leg always passes through point  $C_2$ . To calculate the other entries, we can use:

$$\rho_1^3 = \begin{bmatrix} \mathbf{i} \\ 0 \end{bmatrix}, \quad \rho_2^3 = \begin{bmatrix} \mathbf{v} \\ 0 \end{bmatrix}, \quad \varphi^j = \begin{bmatrix} \frac{\mathbf{b}^j}{|\mathbf{b}^j|} \\ \mathbf{c}^j \times \frac{\mathbf{b}^j}{|\mathbf{b}^j|} \end{bmatrix}, \quad \rho_1^j = \begin{bmatrix} \mathbf{k}_1 \\ \overrightarrow{PA_1} \times \mathbf{k}_1 \end{bmatrix}, \quad j = 1, 2 \quad (3.27)$$

Since  $\overrightarrow{PA_j} = \mathbf{c}^j - \mathbf{b}^j - \mathbf{a}^j$  we have:

$$\begin{aligned} \varphi^j \cdot \rho_1^j &= \frac{\mathbf{b}^j}{|\mathbf{b}^j|} \cdot (\mathbf{c}^j - \mathbf{b}^j - \mathbf{a}^j) \times \mathbf{k}_1^j + \mathbf{k}_1^j \cdot (\mathbf{c}^j \times \frac{\mathbf{b}^j}{|\mathbf{b}^j|}) \\ &= \frac{\mathbf{b}^j}{|\mathbf{b}^j|} \cdot [\mathbf{k}_1^j \times \mathbf{a}^j] \quad j = 1, 2 \end{aligned} \quad (3.28)$$

and so (3.26) can be written as:

$$\begin{bmatrix} \frac{\mathbf{b}^1}{|\mathbf{b}^1|} \cdot \mathbf{k}_1 \times \mathbf{a}^1 & 0 \\ 0 & \frac{\mathbf{b}^2}{|\mathbf{b}^2|} \cdot \mathbf{k}_1 \times \mathbf{a}^2 \end{bmatrix} \begin{bmatrix} \dot{q}_1^1 \\ \dot{q}_1^2 \end{bmatrix} = \begin{bmatrix} \mathbf{c}^1 \times \frac{\mathbf{b}^1}{|\mathbf{b}^1|} \cdot \mathbf{i} & \mathbf{c}^1 \times \frac{\mathbf{b}^1}{|\mathbf{b}^1|} \cdot \mathbf{v} \\ \mathbf{c}^2 \times \frac{\mathbf{b}^2}{|\mathbf{b}^2|} \cdot \mathbf{i} & 0 \end{bmatrix} \begin{bmatrix} \dot{\theta}_1 \\ \dot{\theta}_2 \end{bmatrix} \quad (3.29)$$

which can be abbreviated as:

$$B\dot{\mathbf{q}} = D\dot{\boldsymbol{\theta}} \quad (3.30)$$

where  $B$  is a diagonal matrix.

The Jacobian of the robot is given by:

$$J_{PiBot} = D^{-1}B \quad (3.31)$$

### 3.5.2.1 Singularity Analysis

Matrices  $D$  and  $B$  can become singular depending of the microrobot position. This occurs when leg 1 or leg 2 is in a singular posture with the center of the S-joint lying in the plane of the U-joint. In this case a redundant passive mobility singularity is present. However, if we assume that such leg postures are outside of the range of operation of the mechanism, the singularities of the mechanism are the configurations where either  $B$  or  $D$  is singular, leading to a degeneration of the inverse or the direct instantaneous kinematics, respectively.

In (3.26) or (3.29), matrix  $B$  is singular when one or both elements of its diagonal becomes zero, signifying that the actuated joint axis intersects one of the reciprocal force axes. In this case, if  $D$  is nonsingular, we have a singularity where the end-effector loses freedoms and the input velocities can be nonzero with a stationary platform. This cannot happen in a neighborhood of the reference configuration where  $\mathbf{q}_1^j = 0$ . In this configuration, matrix  $B$  is equal to  $\text{diag}(|\mathbf{a}_1^1|, |\mathbf{a}_2^1|)$  far from having a zero determinant.

To find a singularity of the matrix  $D$ , the axis of either  $\varphi^1$  or  $\varphi^2$  must lie in the plane of the passive-leg U-joint. In this case, the platform cannot be controlled. It can move even with actuators locked and the actuators velocities are not independent and cannot be chosen arbitrarily. Here again, with a good choice of the geometric parameters, the microrobot is safe in a neighborhood of the position where  $\mathbf{q}_1^j = 0$ , with:

$$D = \begin{bmatrix} 0 & -|\mathbf{c}^1| \\ |\mathbf{c}^2| & 0 \end{bmatrix} \quad (3.32)$$

Since the PKM workspace is limited to the angles required to scan the entire vocal fold ( $\pm 12.5^\circ$ ), both  $B$  and  $D$  are expected nonsingular in such reduced workspace.

## 3.6 Optical model

In this section the kinematics of the laser beam which is reflected by a planar mirror located on the microrobot platform is described. In the ideal configuration, the laser beam will be brought by an optical fiber from the exterior until the laryngoscope distal-end. In there, a micromirror is placed in order to focus the laser beam and at the same time to reflect it onto the microrobot platform. On the platform, a planar mirror reflects that laser beam onto the vocal folds. The orientation of the planar mirror is driven by the microrobot. Thus the microrobot steers the direction of the laser beam onto the vocal folds.

### 3.6.1 Basic background on reflective optics

A kinematic scheme is shown in Figure 3.11, which depicts a laser beam that comes from a fixed source and that is then reflected by a planar mirror onto a plane  $\mathcal{P}'$  (representing the vocal folds). The planar mirror undergo two rotations  $\theta_1$  and  $\theta_2$ . Thereby, the laser spot onto the plane  $\mathcal{P}'$  performs a behavior depending on these two rotations  $\theta_1$  and  $\theta_2$  of the platform. This behavior is described below.

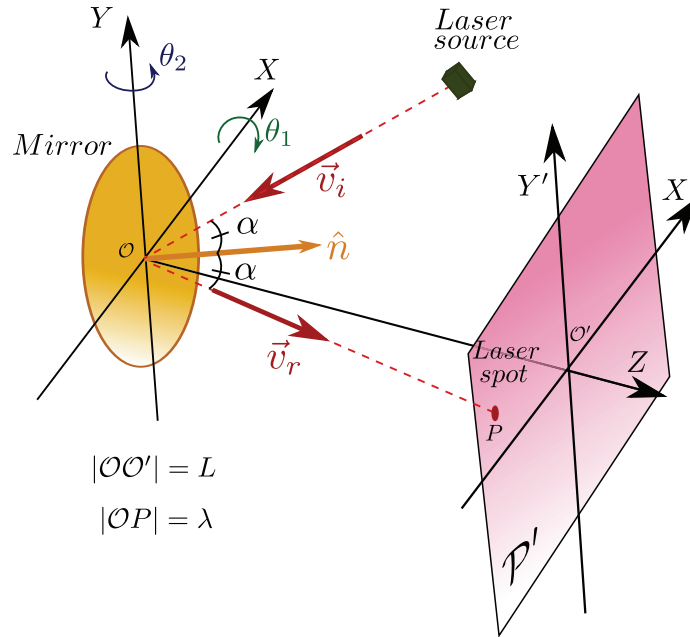


FIGURE 3.11: Laser beam trajectory reflected by a planar mirror.

The unit normal ( $\hat{n}$ ) of the mirror which depends on the angles developed by the mirror ( $\theta_1$  and  $\theta_2$ ) is given by:

$$\hat{n} = R_x(\theta_1)R_y(\theta_2)[0, 0, 1]^T$$

$$\hat{n} = \begin{bmatrix} \sin \theta_2 \\ -\sin \theta_1 \cos \theta_2 \\ \cos \theta_1 \cos \theta_2 \end{bmatrix} \quad (3.33a)$$

where  $R_x$  and  $R_y$  are rotation matrices about  $x$  and  $y$ -axes respectively.

We propose to address the reflection of the laser beam by the planar mirror using Snell law [60]. Considering Figure 3.12 where Snell law states that the reflected laser beam ( $\vec{v}_r$ ) lies in the same plane as the incident laser beam ( $\vec{v}_i$ ) and the unit normal of the mirror ( $\hat{n}$ ). Snell law can be presented analytically as:

$$\vec{v}_r = \vec{v}_i - 2\hat{n}(\hat{n} \cdot \vec{v}_i) \quad (3.34)$$

where  $\vec{v}_i$  and  $\vec{v}_r$  are the unit vectors of the incident and reflected laser beam respectively.

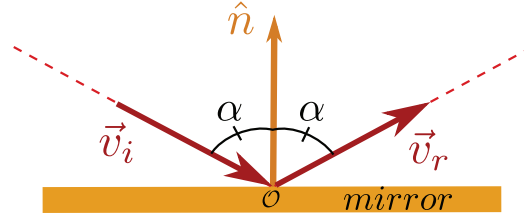


FIGURE 3.12: Snell law.

Moreover, the angle  $\alpha$ , between  $\vec{v}_i$  and  $\hat{n}$  is the same as that between  $\vec{v}_r$  and  $\hat{n}$ . The physical interpretation is relative to the conservation of momentum<sup>1</sup> of the photons that are bouncing off the mirror surface [94].

Considering (3.34) from which we write in the form:

$$\vec{v}_r = \vec{v}_i - 2\hat{n}(\hat{n}^T \vec{v}_i) \quad (3.35)$$

$$\vec{v}_r = \vec{v}_i - 2\hat{n}\hat{n}^T \vec{v}_i \quad (3.36)$$

from which we yield to the form:

$$\vec{v}_r = (I - 2\hat{n}\hat{n}^T) \vec{v}_i \quad (3.37)$$

denoting:

$$\text{ref}(\hat{n}) = (I - 2\hat{n}\hat{n}^T) \quad (3.38)$$

where  $\text{ref}(\hat{n})$  is called mirror reflection transform.

The mirror reflection transform, also called Householder reflection matrix [74] constitutes the basis of the optical kinematics analysis. The operator  $\text{ref}(\hat{n})$  is a  $3 \times 3$  matrix that governs the reflection phenomenon. Notice that  $\text{ref}(\hat{n})$  (3.38) is based on the values coming from  $\hat{n}$ , i.e., in function of  $\theta_1$  and  $\theta_2$ .

Thereby, the unit vector of the reflected laser beam can be computed using:

$$\vec{v}_r = \text{ref}(\hat{n}) \vec{v}_i \quad (3.39)$$

where  $\vec{v}_i$  is the incident laser beam unit vector which has a known and invariable value. Moreover, the component values of  $\vec{v}_i$  depend on the localization of the laser source in the distal-tip of the laryngoscope.

Figure 3.13 shows that the subtraction between  $\vec{v}_r$  and  $\vec{v}_i$  gives a vector in the line direction of  $\hat{n}$ . Thus:

$$\hat{n} = \frac{\vec{v}_r - \vec{v}_i}{\|\vec{v}_r - \vec{v}_i\|} \quad (3.40)$$

<sup>1</sup>Considering a laser beam reflected by a mirror, its normal component of motion is reversed, while its parallel component remains unchanged.



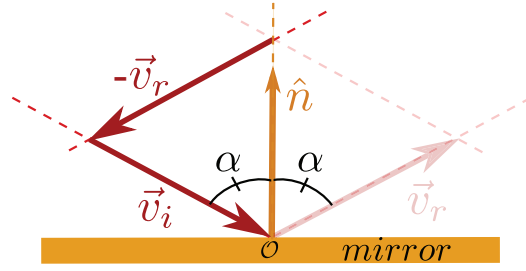


FIGURE 3.13: Optical triangle.

### 3.6.2 Kinematics

#### 3.6.2.1 Forward kinematic model (FKM)

Forward kinematics of the optical system provides the position  $(P = [P_x, P_y, P_z]^T)$  of the spot laser onto the vocal folds (plane  $\mathcal{P}'$ ) given the rotation angles of the mirror ( $\theta_1$  and  $\theta_2$ ), that is  $P = f_p(\theta_1, \theta_2)$ , where  $f_p$  is a nonlinear  $(3 \times 1)$  function depending on  $\theta_1$  and  $\theta_2$ . Considering a reference frame  $O - XYZ$  with origin in the center of mirror. Then, from Figure 3.11, we have:

$$P = \begin{bmatrix} P_x \\ P_y \\ P_z \end{bmatrix} = \lambda \vec{v}_r \quad (3.41)$$

where  $P_x, P_y, P_z$  are values of the components of the point  $P$ .

$$\begin{bmatrix} P_x \\ P_y \\ P_z \end{bmatrix} = \begin{bmatrix} \lambda \vec{v}_{rx} \\ \lambda \vec{v}_{ry} \\ \lambda \vec{v}_{rz} \end{bmatrix} \quad (3.42)$$

where  $\vec{v}_{rx}, \vec{v}_{ry}, \vec{v}_{rz}$  are values of the components of the vector  $\vec{v}_r$ .

From the third component of  $P$  in (3.42) and from Figure 3.11:

$$P_z = \lambda \vec{v}_{rz} = L \quad (3.43)$$

$$\lambda = L / \vec{v}_{rz}$$

Since the working distance  $L$  is fixed and from (3.43) and the first and second component of  $P$  in (3.42), the analyses can be reduced to:

$$\begin{bmatrix} P_x \\ P_y \end{bmatrix} = \begin{bmatrix} L \frac{\vec{v}_{rx}}{\vec{v}_{rz}} \\ L \frac{\vec{v}_{ry}}{\vec{v}_{rz}} \end{bmatrix} \quad (3.44)$$

where the components of  $\vec{v}_r$  are computed using (3.39) ( $\vec{v}_r = \text{ref}(\hat{n})\vec{v}_i$ ), i.e.,  $P_x$  and  $P_y$  are function of the variables  $\theta_1, \theta_2$  and the components of the  $\vec{v}_i$  which is constant.

### 3.6.2.2 Inverse kinematic model (IKM)

The inverse kinematics of the optical system provides the angles of the mirror ( $\theta_1$  and  $\theta_2$ ) given a position of the laser spot onto the vocal folds ( $P_x$  and  $P_y$ ). It can be used to find the necessary posture of the platform to attain a given position of the laser spot.

From (3.33a) and (3.40) the values of  $\theta_1$  and  $\theta_2$  can be computed as a function that depends of  $P_x$  and  $P_y$ . These values were calculated using the nonlinear solver function of Matlab and discarding the solutions which were not compatible with the real setup.

### 3.6.3 Instantaneous Kinematics

#### 3.6.3.1 Forward differential kinematic model (FDKM)

The forward instantaneous kinematics of the optical system provides the relationship between differential positions ( $dP_x$  and  $dP_y$ ) onto the vocal fold's frame and the associated differential rotation in the mirror ( $d\theta_1$  and  $d\theta_2$ ). This relationship, that we will call "Optical Jacobian", is expressed in Cartesian coordinates on the frame associated to the mirror ( $oxyz$ ). We have:

$$\frac{dP_x}{dt} = \frac{\partial P_x}{\partial \theta_1} \frac{d\theta_1}{dt} + \frac{\partial P_x}{\partial \theta_2} \frac{d\theta_2}{dt} \quad (3.45a)$$

$$\frac{dP_y}{dt} = \frac{\partial P_y}{\partial \theta_1} \frac{d\theta_1}{dt} + \frac{\partial P_y}{\partial \theta_2} \frac{d\theta_2}{dt} \quad (3.45b)$$

which provides:

$$\begin{bmatrix} \frac{dP_x}{dt} \\ \frac{dP_y}{dt} \end{bmatrix} = \begin{bmatrix} \frac{\partial P_x}{\partial \theta_1} & \frac{\partial P_x}{\partial \theta_2} \\ \frac{\partial P_y}{\partial \theta_1} & \frac{\partial P_y}{\partial \theta_2} \end{bmatrix} \begin{bmatrix} \frac{d\theta_1}{dt} \\ \frac{d\theta_2}{dt} \end{bmatrix} \quad (3.46)$$

$$\dot{P} = J_{opt} \dot{\theta} \quad (3.47)$$

where  $J_{opt}$  is the Optical Jacobian.

#### 3.6.3.2 Inverse differential kinematic model (IDKM)

The inverse instantaneous kinematics of the optical system provides the relationship between the differential rotation of the mirror ( $d\theta_1$  and  $d\theta_2$ ) and the associated differential position of the laser spot onto the vocal folds ( $dx$  and  $dy$ ). This relationship is based on the inverse of the Optical Jacobian. It is expressed in Cartesian coordinates on the frame associated to the mirror ( $oxyz$ ) as follows:

$$\dot{\theta} = J_{opt}^{-1} \dot{P} \quad (3.48)$$

### **3.7 Conclusion**

This chapter has introduced the kinematic structures of the two proposed microrobots based on two different approaches. Then, theoretical aspects of kinematic analysis including the screw theory were presented. Kinematic analysis of the two proposed structures were performed which permitted to obtain the kinematic Jacobian matrices that will be useful in Chapter 5, devoted to the control of the microrobots. Finally a kinematic optical model of the part between the mirror and the laser spot behavior has been developed. Again, this will be used in Chapter 5. The contributions of this chapter have dealt: first, with the proposition of two concepts to obtain microrobots with large amplitudes and high bandwidth, and second with the introduction of a new parallel kinematic mechanism named PiBot.

# Fabrication

*This chapter is devoted to the fabrication of the two novel microrobots (The Micro Agile-Eye and the PiBot) whose kinematics were previously presented. The Smart composite microstructures (SCM) fabrication technique is presented and used to build the two proposed microrobots. Then an analysis of the errors of positioning of one of the robots and caused by the fabrication is presented. For that we use Interval Analysis.*

## Chapter contents

---

<b>4.1</b>	<b>Introduction</b>	<b>78</b>
<b>4.2</b>	<b>Proposed fabrication process</b>	<b>78</b>
4.2.1	Materials	78
4.2.2	Process of fabrication	78
4.2.3	Parallel robots and the SCM technique	80
4.2.4	Important parameters for designing hinges in SCM	81
<b>4.3</b>	<b>Fabricated prototypes</b>	<b>82</b>
4.3.1	Fabrication of a single hinge	82
4.3.2	Fabrication of the Micro Agile-Eye microrobot	83
4.3.3	Fabrication of the PiBot microrobot	88
<b>4.4</b>	<b>Precision evaluation</b>	<b>90</b>
4.4.1	Interval analysis	91
4.4.2	Spatial rigid motion tools	93
4.4.3	Interval representation of uncertainties	94
4.4.4	Transferring the uncertainties	94
4.4.5	Methodology to evaluate uncertainties in parallel robots	95
4.4.6	Implementation of the method on the proposed PiBot microrobot	96
<b>4.5</b>	<b>Conclusions</b>	<b>101</b>

---

## 4.1 Introduction

The two microrobots (Micro Agile-Eye and PiBot) to be fabricated present 3D structures. However, the fabrication of 3D microstructures is a very challenging step in the literature due to the difficulty to create complex shape and to assemble small components at the mesoscale. This scale can be defined by the fact that mesoscale mechanisms have a volume in order of a  $\text{cm}^3$ . Below is the microscale and the world of MEMS, based on Si-based processes; above is the macroscale and the world of conventional fabrication. One of the very rare efficient methods to produce 3D microstructures is the SCM (Smart Composite Microstructures) technology [185, 186, 127, 192]. We will use this for the development of our microrobots. This technology yields however imperfect joints, like the other methods. We therefore propose to evaluate the imprecision of the realized microrobot by using interval analysis.

## 4.2 Proposed fabrication process

### 4.2.1 Materials

First, we present the materials used for the SCM technology to fabricate the microrobots. They are:

- i) carbon fiber (CF): sheet of carbon fiber with  $130 \mu\text{m}$  of thickness. The carbon fiber permits to rigidify the structure of the microrobots at a very light weight cost.
- ii) polyimide film: a film of  $7\sim 10 \mu\text{m}$  of thickness made of polyimide which is used as flexure material to fabricate all compliant parts of the flexure hinges. This material was chosen for its anti-crystallization<sup>1</sup> properties with respect to high temperature changes at the moment of the fabrication (from  $120^\circ\text{C}$  to room temperature). Note that this high temperature range is very interesting both for the intracorporeal use of the structure but also for its compliance with sterilisation processes.
- iii) piezoelectric cantilevers actuators: actuators made of piezoelectric material (Lead Zirconate Titanate - PZT, see Appendix A) with a cantilever shape. They are mixed with carbon fiber and polyimide into the SCM fabrication process.

### 4.2.2 Process of fabrication

The fabrication of the complex structure starts with the fabrication of single flexible joints that are fundamental for the microrobot such as depicted in Figure 4.1.

---

<sup>1</sup>Crystallization makes the compliant part of the hinge very brittle and decreases the structure lifetime.

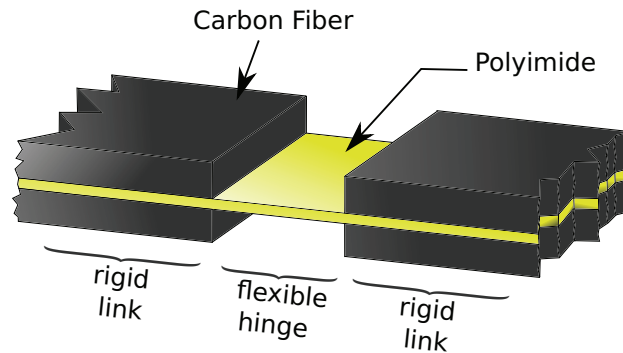


FIGURE 4.1: Parts of a flexure hinge which results from the SCM fabrication technique.

Thereby, the fabrication is based on: one polyimide layer that serves as a flexible element and two layers of carbon fiber to rigidify the structure. The thickness of each carbon fiber layer and polyimide layer is  $130\ \mu\text{m}$  and  $10\ \mu\text{m}$ , respectively. The stages of this process are depicted in Figure 4.2 and defined as:

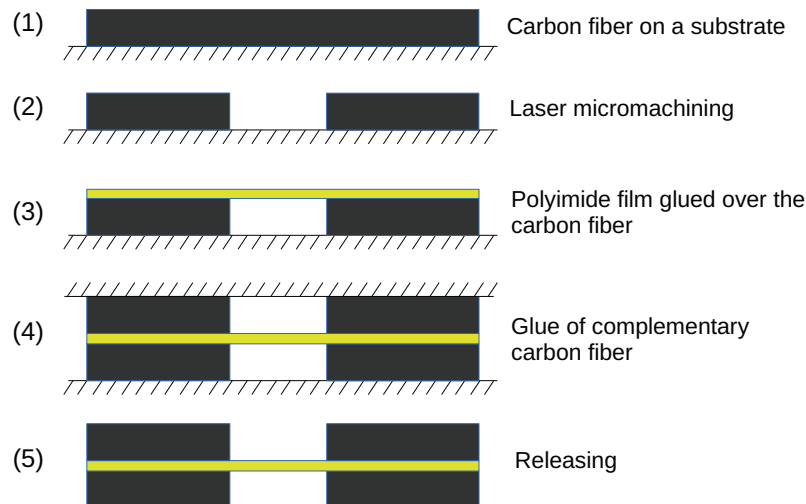


FIGURE 4.2: Process of fabrication of single flexible joints.

1. **Step 1:** A unidirectional carbon fiber sheet with  $130\ \mu\text{m}$  of thickness is cured using a thermosetting resin in an oven and then fixed on a support (see Figure 4.2-(1)),
2. **Step 2:** The cured carbon fiber sheet is micromachined by a femtosecond laser in order to have the patterns as depicted in Figure 4.2-(2). Patterns details are approximately of  $\sim 10\ \mu\text{m}$ . Two similar patterns are fabricated,
3. **Step 3:** A layer of polyimide with  $10\ \mu\text{m}$  of thickness is glued on one of the patterns of the carbon fiber, as depicted in Figure 4.2-(3),

4. **Step 4:** The other carbon fiber pattern is glued and adjusted on the top of the first pattern with polyimide, as depicted in Figure 4.2-(4), then the whole is put into an oven for solidification. A pressure is applied to keep the new sandwich structure flat and to avoid ripples.
5. **Step 5:** Finally, the sandwich (CF-Polyimide-CF) is again machined with laser in order to release the final structure.

The realized structure is therefore composed of two rigid bodies made of carbon fiber linked by a flexible hinge made of polyimide: rigid - flexible - rigid, as shown in Figure 4.1. Basically the flexible part is used to fold the structure and the rigid part serves as a link.

### 4.2.3 Parallel robots and the SCM technique

The basic concept behind SCM is to create passive hinges. These passive hinges are like passive joints which are combined in some parts with actuators and in other parts simply left free. The whole (actuated joints and passive joints) are combined in an auto-constrained structure. That auto-constrained structure should be capable to use passive joints and, at the same time, have the controllability of them. These structures are clearly parallel architecture structures which unlike to serial architecture structures, can use passive joints inside. In our case, we propose to create parallel kinematic machines or parallel robots using SCM combined with piezoelectric actuators. Let us recall that the dimensions of these parallel robots are in the millimeter-scale. Each microrobot should be full packaged in  $10 \times 10 \times 10 \text{ mm}^3$  as maximum, with pattern details in the micro-scale (dimension of the detail are  $10\mu\text{m}$ ).

To create the parallel robots, some basic joints have first to be feasible with this process. Table 4.1 presents all joints and their equivalences made by SCM as we proposed and those that are normally used in classical robotics (large scale robotics).

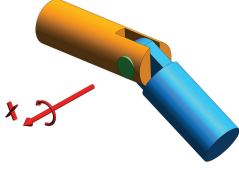
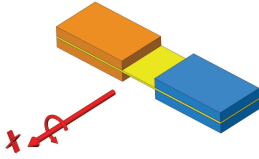
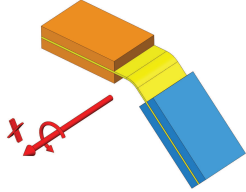
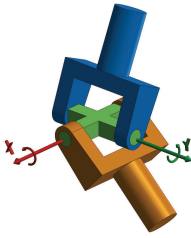
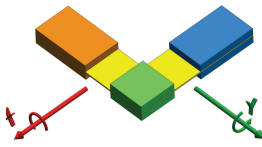
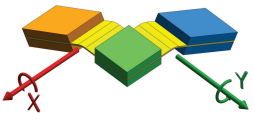
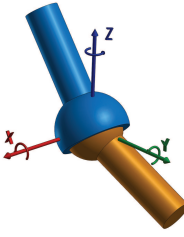
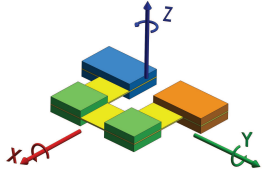
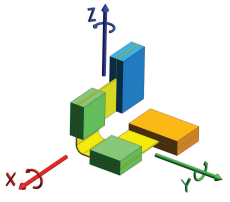
Joints		Large-Scale	Millimeter-Scale	
		Using conventional techniques	Using SCM	
			<i>Planar</i>	<i>Folded</i>
Revolute	R			
				
Spherical	S			

TABLE 4.1: Conventional joints and their equivalences made with SCM process.

#### 4.2.4 Important parameters for designing hinges in SCM

The design of one simple hinge is first based on the gap “ $e$ ” evidenced in Figure 4.3a. Then the dimensions of the hinge is calculated according to the angle  $\theta$  to be developed and to this gap, see Figure 4.3b. From this figure, we can see the strong link between the gap and the angle:

$$e = f\theta L_{cf} \quad (4.1)$$

where:

$L_{cf}$  is the thickness of the carbon fiber which is approximatively  $130 \mu\text{m}$ ,

$\theta$  (rad) is the maximum angle to be developed by the hinge,

$e$  is the gap permitting the rotation,

$f$  is a safety factor that we introduce to ensure that the hinge does not lock due to unavoidable



defects in the fabrication process. In practice, we have used  $f=1.1$ .

Notice that the thickness of the polyimide layer has not been taken into account because the thickness of one layer (about  $8.5 \mu\text{m}$ ) does not affect significantly the calculus.

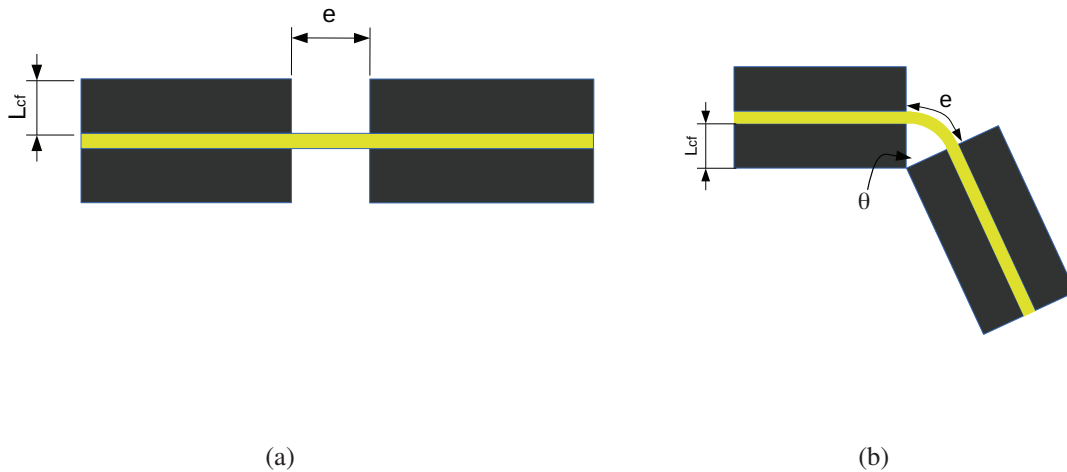


FIGURE 4.3: Main parameters for designing hinges in SCM. (a) Unfolded hinge where the gap  $e$  is the space between the two links,  $L_{cf}$  is the thickness of the carbon fiber. (b) Folded hinge where the maximum reachable  $\theta$  angle is in accordance with  $e$  and  $L_{cf}$ .

### 4.3 Fabricated prototypes

In this section, the different fabrication results and the prototypes of the two microrobots are presented. First, a simple hinge was fabricated. Then complex 2D structures are shown. These 2D structures are afterwards folded to create 3D structures. The process to yield the 3D structure from the 2D one follows a specific procedure.

First and foremost, to fold 2D to 3D structures, we have two options: either *bottom-up* (first fix the legs and then the platform), or *top-down* (first fix the platform and then each leg). Thus, based on the property of parallel kinematic structures that inverse kinematics is easier than forward kinematics, i.e., it is easier to compute the actuator values from the end-effector pose rather than the converse, we used and propose to use the top-down option. In practice, we have also tried the bottom-up (i.e. fixing legs first then the platform) without success.

#### 4.3.1 Fabrication of a single hinge

The basic element necessary for the development of the two microrobots is the revolute joint. Such unactuated joints, realized by SCM technique, are perfectly adapted to parallel kinematic

machines where the use of unactuated joint is allowed. Figure 4.4 presents a SEM-image of a fabricated sample that we have fabricated. Many details can be appreciated from the image. For instance, we observe that the hinge is far from being perfect, contrary to the CAD design that is shown in Figure 4.1, since the fabrication yielded defaults and imprecisions.

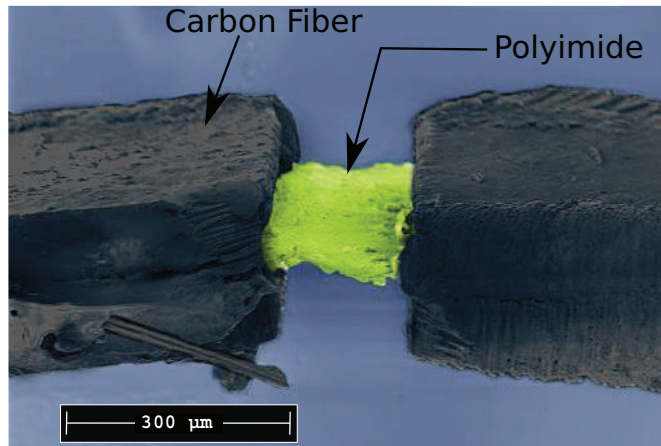


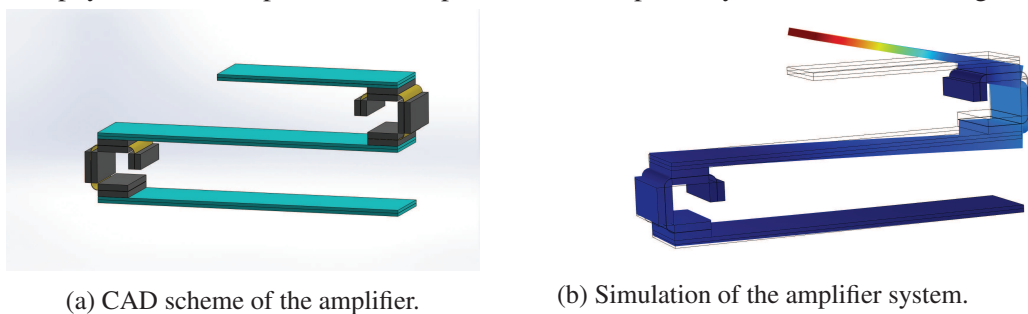
FIGURE 4.4: Pseudocolored SEM image depicting the carbon fiber along with the flexible polyimide.

### 4.3.2 Fabrication of the Micro Agile-Eye microrobot

The fabrication process of the microrobot called Micro Agile-Eye was split into three main parts. The first part consisted in developing an array of actuators with their mechanical amplifier. The second part consisted in developing the spherical parallel structure Agile-Eye (2DoF) that transforms the displacement of the actuators into rotations of the platform. Finally the two structures, i.e. the legs based on the array of actuators and the Agile-Eye structure are assembled and mounted on a 3D printed frame.

#### 4.3.2.1 Mechanical amplifiers

The CAD design of the amplifier system is shown in Figure 4.5a. Simulation using Comsol Multiphysic shows the performances expected of the amplifier system, as shown in Figure 4.5b.



(a) CAD scheme of the amplifier.

(b) Simulation of the amplifier system.

FIGURE 4.5: Amplifier system.

Results of the microfabrications are described in the sequence of Figures 4.6a, 4.6b, 4.6c, 4.6d. Figure 4.6a shows the flexible element that allow the lever effect. The view of the flexible element and a piezoelectric cantilever actuator compared with 1 cent euro coin is shown in Figure 4.6b. The support of the actuation system fabricated by 3D printing with the other elements are shown in Figure 4.6c. The assembled of piezoelectric cantilever actuators with the flexible element are shown in Figure 4.6d.

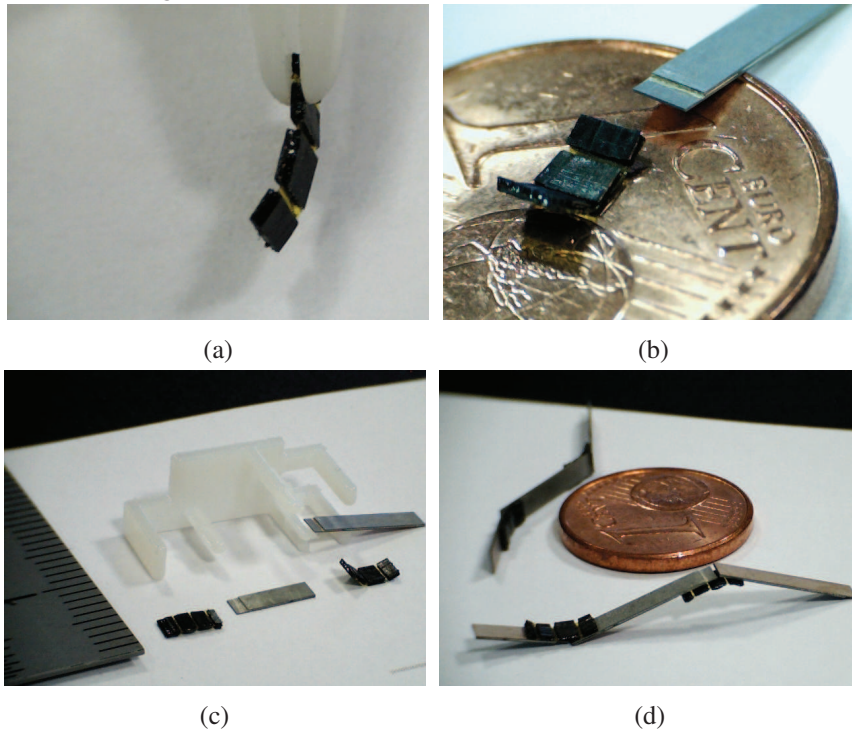


FIGURE 4.6: Fabrication result of the amplifier system. (a) Flexible elements which are a constituent part of the joints in the mechanical amplifier. (b) A flexible element and a piezoelectric cantilever actuators before they are assembled. (c) Support and elements before they are assembled. (d) Piezoelectric cantilever actuators assembled with the flexible elements.

Finally the assembled prototype with its electrical connections are shown in Figure 4.7a and Figure 4.7b.

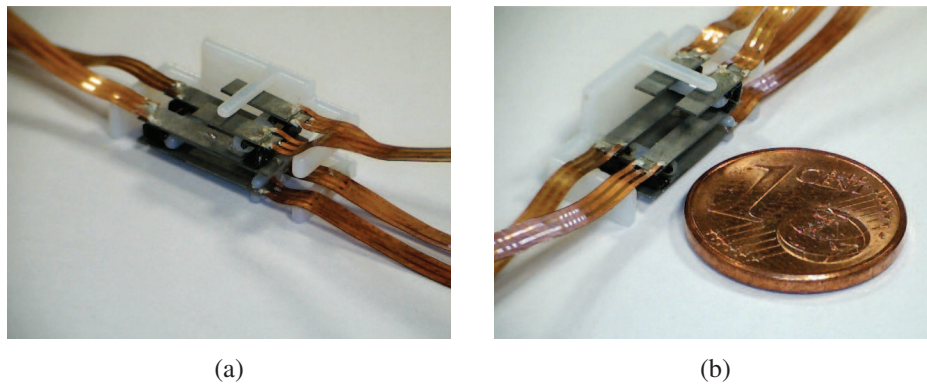


FIGURE 4.7: (a) Amplifier mechanism assembled with its electrical connections. (b) Other view of the amplifier system compared with one cent euro coin.

#### 4.3.2.2 Platform

The platform which is destined to be placed on the actuation system is fabricated entirely as a planar structure and then the structure is folded to yield in a 3D structure. The CAD design of the platform is shown in Figure 4.8.

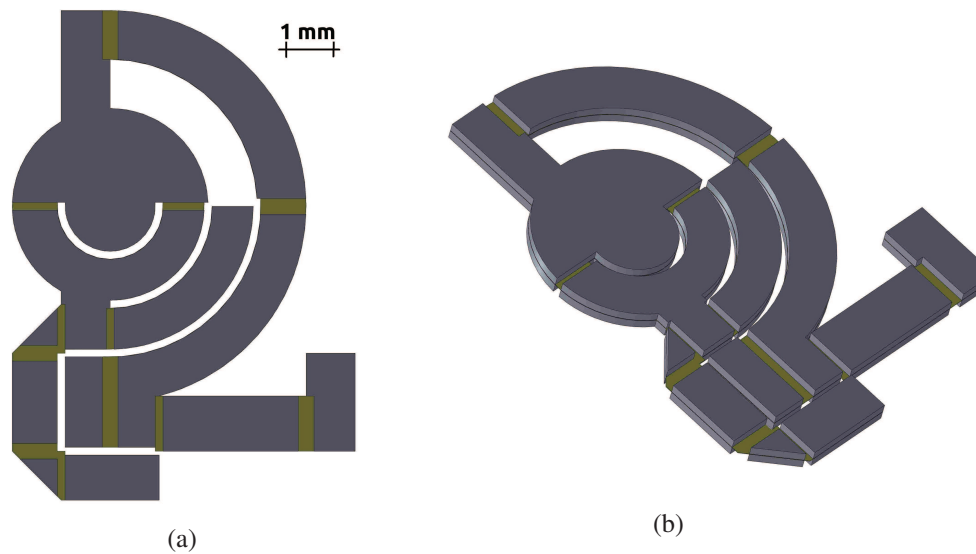


FIGURE 4.8: (a) CAD design of the orientable platform before the folding process. (b) Other view of the structure.

The fabrication outcome of the planar structure is shown in Figure 4.9.

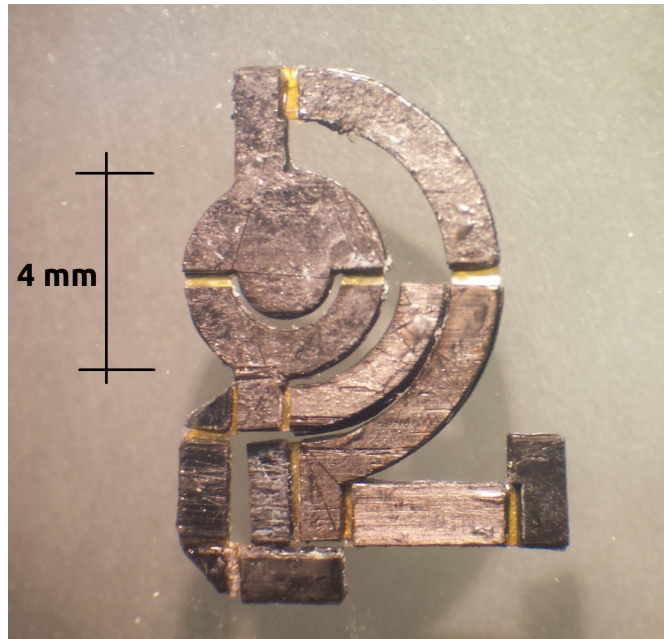


FIGURE 4.9: Fabricated orientable platform in 2D.

#### 4.3.2.3 Complete system

The assembled microrobot which is composed by the actuation legs and the platform is depicted in a CAD design, as shown in Figure 4.10. An initial orientation is shown in the complete system. This initial orientation is obtained by geometrical design in order to reflect the laser beam perpendicular to the topside (upper surface). The support that holds the complete system is shown in Figure 4.10c and Figure 4.10d.

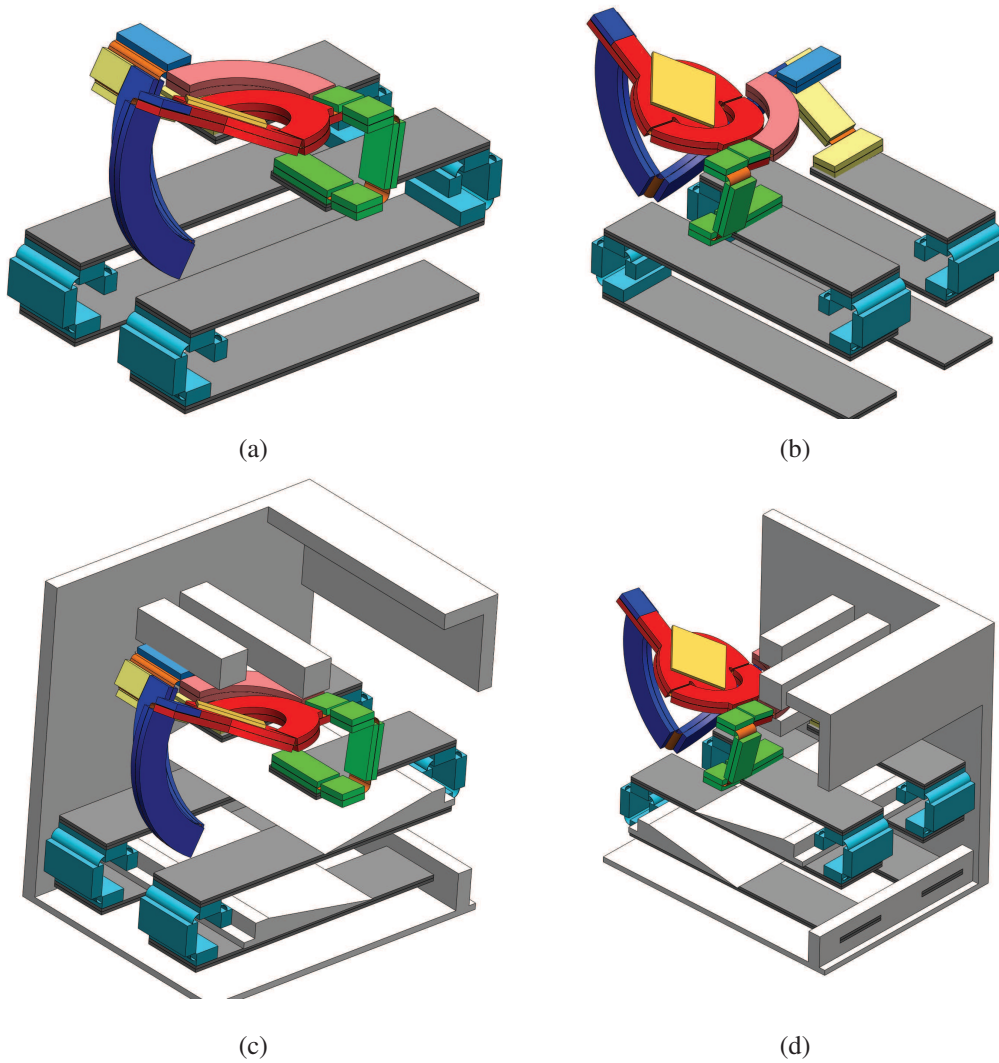


FIGURE 4.10: (a) CAD design of the assembled microrobot. (b) A micromirror layer device is placed on the platform. (c) CAD design of the complete assembled microrobot including its support. (d) Other view of the microrobot Micro Agile-Eye.

The fabrication outcome is shown in Figure 4.11 The electrical connections are fixed through the support which was done by 3D printing. The complete device has a size slightly smaller than  $1 \text{ cm}^3$ .



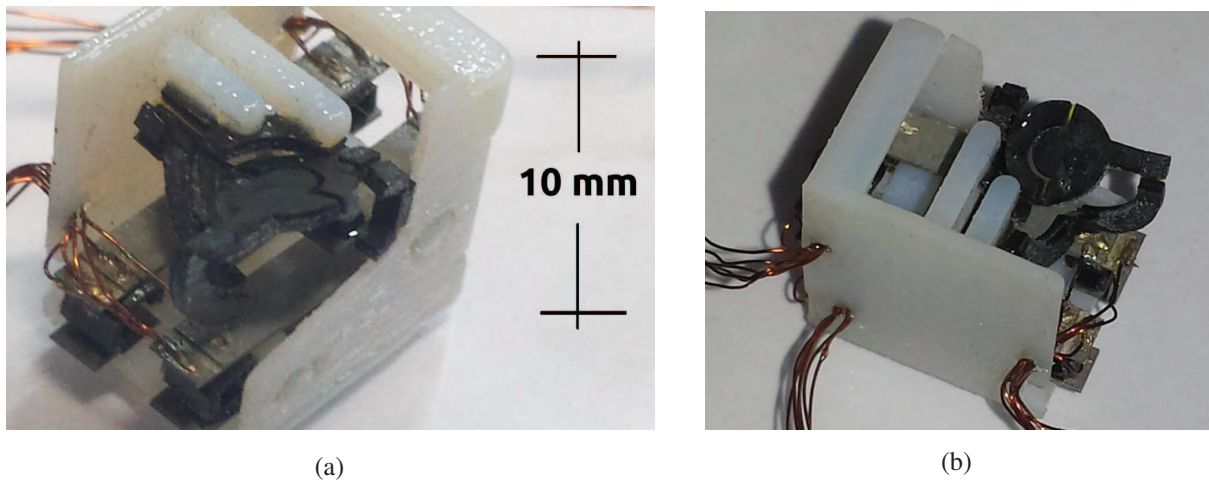


FIGURE 4.11: (a) Fabricated and assembled Micro Agile-Eye microrobot. (b) Other view of the Micro Agile-Eye.

### 4.3.3 Fabrication of the PiBot microrobot

As mentioned earlier, the SCM technique was also used to fabricate the PiBot. Thereby, the first stage was the design of the 2D CAD structure, as shown in Figure 4.12. The fabrication outcome of the 2D structure is shown in Figure 4.13.

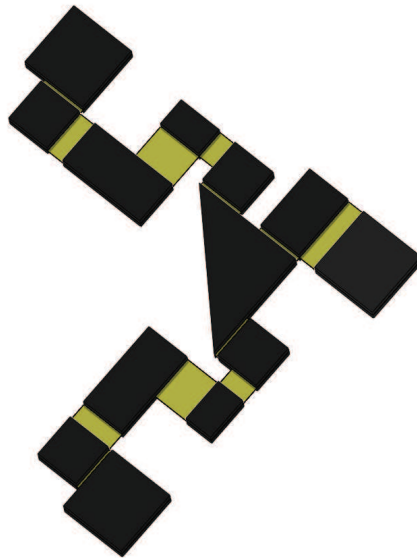


FIGURE 4.12: CAD design of the planar stage of the PiBot.

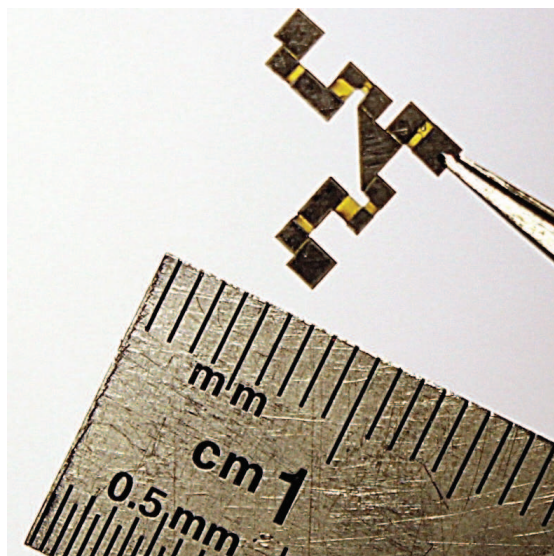


FIGURE 4.13: Realization of the planar structure corresponding to the PiBot.

Then, two piezoelectric cantilever actuators of 10 mm length, 2 mm width and 250  $\mu\text{m}$  thickness are introduced. A base fabricated by 3D printing serves as support. The CAD model of the folded PiBot microrobot is shown in Figure 4.14. Finally, Figure 4.15 shows the amazingly resemblant realization of the PiBot microrobot.

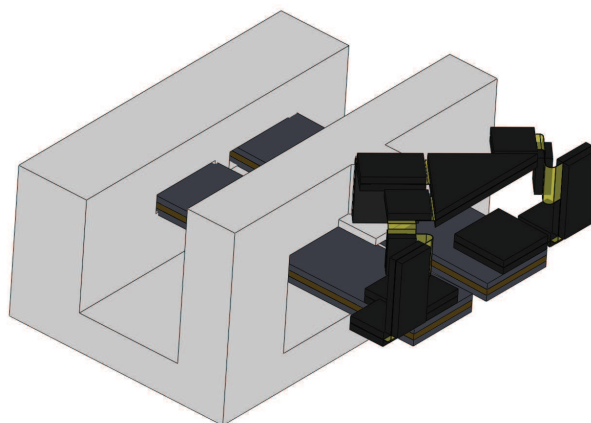


FIGURE 4.14: CAD design of the folded structure.



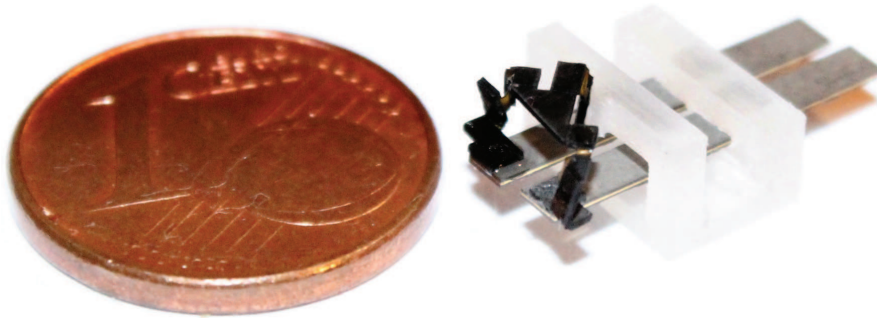


FIGURE 4.15: Realization of the PiBot compared with one cent euro coin.

#### 4.4 Precision evaluation

Indeed, SCM technology has many advantages over other methods. The SCM-based structures allow to perform large deformations thanks to the polyimide layer and to the carbon fiber. SCM technique yields therefore remarkable improvements without causing either fracture or rapid fatigue on the operating structure. Nevertheless, this advantage disfavors the overall precision. To explain this, a bent joint of a SCM structure is shown in Figure 4.16a. As shown in Figure 4.16b, the joint itself generates undesirables strains. The latter will dislocate the direction and location of the rotation axis. Consequently, uncertainties on the end-effector tilts are observed in SCM-based structures.

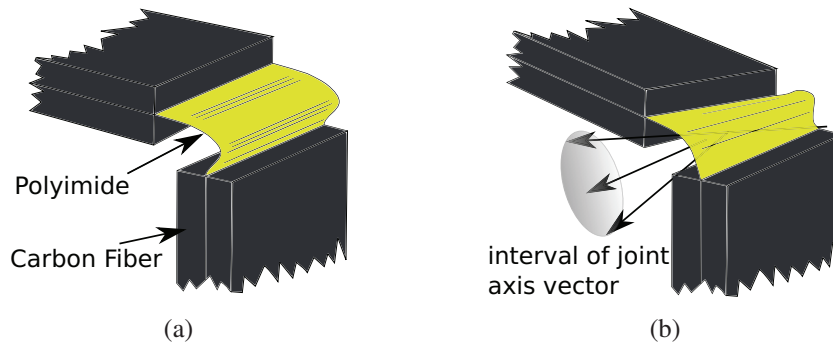


FIGURE 4.16: (a) A hinge based on the flexibility of a polyimide material. (b) Sprained kink dislocating the position and the direction of the rotation axis in position and direction.

These uncertainties are principally due to defects created during the microfabrication. Thus, in each joint, SCM microfabrication results in an uncertain Euclidean transformation built upon three components:

- 1) uncertainties on the joint angle,
- 2) uncertainties on the joint axis orientation,
- 3) uncertainties on the position coordinate of the joint axis.

These uncertainties can be quantified from the dimensions of the flexible hinge: the rigid-to-rigid distance for the position or the cone defined by the hinge (see Figure 4.16b) for the direction. It is noteworthy that all these uncertainties can drastically decrease the overall precision of the microrobot platform (end-effector). Thanks to interval analysis, we do not need to push further on the modeling of the associated physics and can rely on (interval) kinematics representation to bound the latter components. A brief introduction about the theory of interval analysis is first presented below. then we present the errors evaluation by using interval techniques.

#### 4.4.1 Interval analysis

##### 4.4.1.1 Definitions

A closed interval denoted by  $[x]$ , is the set of real numbers given by:

$$[x] = [x^-, x^+] = \{x \in \mathbb{R} / x^- \leq x \leq x^+\} \quad (4.2)$$

The endpoints  $x^-$  and  $x^+$  are respectively the left and right endpoints of  $[x]$ .

$[x]$  is said as degenerate interval if  $x^- = x^+$ . Such an interval contains a single real number  $x$ . By convention, a degenerate interval  $[a, a]$  can be described with the real number  $a$ .

- The width of an interval  $[x]$  is given by:

$$w([x]) = x^+ - x^- \quad (4.3)$$

- The midpoint of  $[x]$  is given by:

$$mid([x]) = \frac{x^+ + x^-}{2} \quad (4.4)$$

- The radius of  $[x]$  is given by:

$$rad([x]) = \frac{x^+ - x^-}{2} \quad (4.5)$$

##### 4.4.1.2 Operation on intervals

The elementary mathematical operation are also extended to intervals, the operation result between two intervals is an interval containing all the operations results of all pairs of numbers in the two intervals. So, if we have two intervals  $x = [x^-, x^+]$  and  $y = [y^-, y^+]$  and a law  $\circ \in \{+, -, \cdot, /\}$ , we obtain:

$$[x] \circ [y] = \{x \circ y \mid x \in [x], y \in [y]\} \quad (4.6)$$

The four basic operations are as follows.

- The sum of two intervals  $[x] + [y]$  is defined by:

$$[x] + [y] = [x^- + y^-, x^+ + y^+] \quad (4.7)$$

- The difference of two intervals  $[x] - [y]$  is defined by:

$$[x] - [y] = [x^- - y^+, x^+ - y^-] \quad (4.8)$$

- The product of two intervals  $[x] \cdot [y]$  is the set:

$$[x] \cdot [y] = [\min(x^-y^-, x^-y^+, x^+y^-, x^+y^+), \max(x^-y^-, x^-y^+, x^+y^-, x^+y^+)] \quad (4.9)$$

- The quotient of two intervals  $[x] / [y]$  is defined as:

$$[x] / [y] = [x] \cdot [1/y^+, 1/y^-], \quad 0 \notin [y] \quad (4.10)$$

- The intersection of two intervals  $[x] \cap [y]$  is the interval defined by:

- i) if  $y^+ < x^-$  or  $x^+ < y^-$  the intersection is the empty set:

$$[x] \cap [y] = \emptyset \quad (4.11)$$

- ii) Otherwise:

$$[x] \cap [y] = [\max\{x^-, y^-\}, \min\{x^+, y^+\}] \quad (4.12)$$

- In the latter case, the union of two intervals  $[x] \cup [y]$  is also an interval defined by:

$$[x] \cup [y] = [\min\{x^-, y^-\}, \max\{x^+, y^+\}] \quad (4.13)$$

When  $[x] \cap [y] = \emptyset$ , the union of the two intervals is not an interval. For that, the interval hull is defined:

$$[x] \sqcup [y] = [\min\{x^-, y^-\}, \max\{x^+, y^+\}] \quad (4.14)$$

It was proven that:  $[x] \cup [y] \subseteq [x] \sqcup [y]$  for any two intervals  $[x]$  and  $[y]$ .

#### 4.4.1.3 The set inversion problem

The problem which consists in finding the set  $X$  of variable  $x$  such that  $f(x) \in Y$ , where  $Y$  is a given set, is a set inversion problem. That is, find  $X$  such that  $X = \{x \in \mathfrak{R}^n \mid f(x) \in Y\} = f^{-1}(Y)$ . Such a problem can be solved by a set inversion algorithm, such as SIVIA (set inversion *via* interval analysis) [93]. This algorithm is based on interval techniques and operations and is summarized in Table 4.2, where  $w([\mathbf{x}])$  is the width of the interval argument  $[\mathbf{x}]$  (as was defined in (4.3)) and  $\varepsilon$  is the accuracy of the computation.  $\underline{\mathbb{S}}$  and  $\overline{\mathbb{S}}$  correspond to the upper and lower bounds of the set solution  $\mathbb{S}$ :  $\underline{\mathbb{S}} \subseteq \mathbb{S} \subseteq \overline{\mathbb{S}}$ .

SIVIA(inputs: $[\mathbf{x}]$ , $\varepsilon$ ; outputs: $\underline{\mathbb{S}}$ , $\overline{\mathbb{S}}$ )
1: if $[\mathbf{f}]([\mathbf{x}]) \cap [\mathbf{Y}] = \emptyset$ , $[\mathbf{x}]$ is non-solution;
2: if $[\mathbf{f}]([\mathbf{x}]) \subseteq [\mathbf{Y}]$ , thus $\underline{\mathbb{S}} := \underline{\mathbb{S}} \cup [\mathbf{x}]$ ; $\overline{\mathbb{S}} := \overline{\mathbb{S}} \cup [\mathbf{x}]$ ;
3: if $w([\mathbf{x}]) < \varepsilon$ thus $\overline{\mathbb{S}} := \overline{\mathbb{S}} \cup [\mathbf{x}]$ ;
4: otherwise bisect $[\mathbf{x}]$ into $[\mathbf{x}_1]$ and $[\mathbf{x}_2]$ ; <div style="margin-left: 20px;">SIVIA(inputs: <math>[\mathbf{x}_1]</math>, <math>\varepsilon</math> ; outputs: <math>\underline{\mathbb{S}}</math>, <math>\overline{\mathbb{S}}</math> ) ;</div> <div style="margin-left: 20px;">SIVIA(inputs: <math>[\mathbf{x}_2]</math>, <math>\varepsilon</math> ; outputs: <math>\underline{\mathbb{S}}</math>, <math>\overline{\mathbb{S}}</math> ).</div>

TABLE 4.2: The SIVIA algorithm [93].

SIVIA algorithm reaches its limit when  $\mathbb{S} = [f]^{-1}(Y)$  is large or has higher dimension than two. In fact, the computational time increases exponentially with the number of variables and with the desired accuracy  $\varepsilon$  on the characterization. Additionally, other possible causes of the increase the computation time are: the choice of the inclusion functions and the bisection strategy [93].

#### 4.4.2 Spatial rigid motion tools

In this work, the exponential mapping is used to highlight the uncertain motions in the micro-robot and that were not possible to yield by other representations. In fact, exponential mapping allows a global description and a geometric handling of spatial rigid body motion and is widely described in classically sized robotic systems [161]. Thus an exponential mapping representation for  $SE(3)$  (special Euclidean group) is used to account for the uncertain motions present in the joints. Remind that the motion generated by a rotational joint is described by the homogeneous transformation  $T_{joint} \in SE(3)$  obtained by the following exponential matrix:

$$T_{joint} = e^{\hat{\xi}q} \quad (4.15)$$

where  $q$  is the joint variable and  $\hat{\xi}$  belongs to  $se(3)$ , the Lie algebra associated to  $SE(3)$ . The latter is given by:

$$\hat{\xi} = \begin{bmatrix} \hat{\omega} & -\omega \times \mathbf{p}_{joint} \\ 0 & 0 \end{bmatrix} \quad (4.16)$$

where  $\mathbf{p}_{joint}$  is the joint position and

$$\hat{\omega} = \begin{bmatrix} 0 & -\omega_3 & \omega_2 \\ \omega_3 & 0 & -\omega_1 \\ -\omega_2 & \omega_1 & 0 \end{bmatrix} \quad (4.17)$$

where  $\hat{\omega} \in so(3)$  is built upon  $\omega = [\omega_1 \ \omega_2 \ \omega_3]^T$ , the unitary vector representing the direction of the joint axis.

### 4.4.3 Interval representation of uncertainties

Since the formalization of intervals in [122], these tools have been used in various applications: modeling, algorithms and computation, signals and parameters estimation, stability analysis, control design and robotic modeling. In particular, interval techniques permit to determine the bounds of uncertainties for a given function in which its variables have uncertainties. Having that possibility, it is possible for instance in robotics to determine the precision at the end-effector from the bounded uncertainties in the joints for a serial manipulators [132]. In order to perform an analysis of uncertainties, they have to be mathematically quantified in each joint axis. Their physical characteristics and limits have to be abstracted using intervals sets. Thus values of either scalars (angles) or vectors (axes direction and position coordinates) are expressed by intervals as:

i) an angle  $q$  becomes  $Q = [q - \delta_q, q + \delta_q]$ .

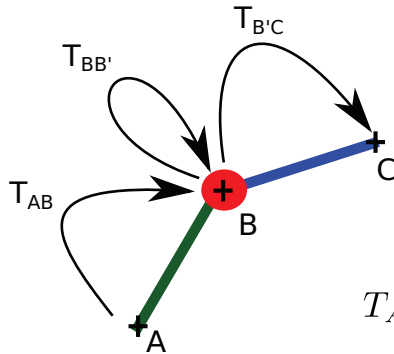
ii) a point  $p$  with coordinates  $[p_x, p_y, p_z]^T$  becomes:  $P = \begin{bmatrix} p_x - \delta_{p_x}, & p_x + \delta_{p_x} \\ p_y - \delta_{p_y}, & p_y + \delta_{p_y} \\ p_z - \delta_{p_z}, & p_z + \delta_{p_z} \end{bmatrix}$

iii) a vector  $\omega$  with components  $[\omega_1, \omega_2, \omega_3]^T$  becomes:  $\Omega = \begin{bmatrix} \omega_1 - \delta_{\omega_1}, & \omega_1 + \delta_{\omega_1} \\ \omega_2 - \delta_{\omega_2}, & \omega_2 + \delta_{\omega_2} \\ \omega_3 - \delta_{\omega_3}, & \omega_3 + \delta_{\omega_3} \end{bmatrix}$

where  $\delta_i$ , with  $i \in \{q, \omega_1, \omega_2, \omega_3, p_x, p_y, p_z\}$ , correspond to the radius of uncertainties.

### 4.4.4 Transferring the uncertainties

Similar to Figure 4.16b, Figure 4.17 shows two rigid links attached by the joint at B. Uncertainties due to the SCM fabrication technique are exhibited at the joint B (uncertainties of angle, of axis direction and of position).



joint at B shows uncertainties of:

- angle developed,
- joint axis orientation,
- position coordinate.

$$T_{AC} = T_{AB} * T_{BB'} * T_{B'C}$$

FIGURE 4.17: Two links and a flexible hinge at B with uncertainties due to the SCM fabrication technique.

Thus, the homogeneous transformation between the reference frame in A and the one in C is denoted by:  $T_{AC} = T_{AB} * T_{BB'} * T_{B'C}$ , where the homogeneous transformation  $T_{BB'}$  takes into account the joint uncertainties in B. It is explicitly denoted as:

$$T_{BB'} = e^{\hat{\Xi}_B Q_B} \quad (4.18)$$

where:

$Q_B$  is the interval representing the uncertain angle developed at B.

$\hat{\Xi}_B$  is an interval matrix that is compatible with the structure of  $se(3)$  and is given by:

$$\hat{\Xi}_B = \begin{bmatrix} \hat{\Omega}_B & -\Omega_B \times P_B \\ 0 & 0 \end{bmatrix} \quad (4.19)$$

where:

$\Omega_B$  is the vector interval representing the uncertain axis direction of the joint at B.

$P_B$  is the vector interval representing the uncertain position of the point B.

#### 4.4.5 Methodology to evaluate uncertainties in parallel robots

Our methodology to find the uncertainties in the platform follows the following steps.

- The analysis starts by solving the inverse kinematics (i.e finding the joint variables ( $q$ ) in function of a given space variables ( $x$ )) of the parallel robot, in a given configuration using conventional arithmetics.
- Then, the uncertainties corresponding to each joint ( $q \rightarrow Q$  and  $\xi \rightarrow \Xi$ ) are introduced, using the interval exponential matrices.
- Finally, the implicit kinematic constraint is solved for the end-effector pose  $X$ , given the calculated uncertainties.

Let us develop these three steps:

##### i) Inverse kinematics

A brief reminder: Inverse kinematics deals with computing the joint variables  $q$  with respect to the operational angles  $x$ . In [120], a methodology to calculate the inverse kinematics of a parallel robot using the implicit equations of the structure geometry was described. Initially, the coordinates of one specific point on the robot are expressed as a function  $H_1(x)$  of the end-effector variables. Then, the same coordinates are expressed as a function  $H_2(q)$  of the joint variables. Thereby, equating  $H_1(x)$  and  $H_2(q)$  yields the implicit kinematic constraint:  $H_1(x) = H_2(q)$ . Finally, joint variables are expressed in function of the end-effector variables ( $q = f(x)$ ).

ii) **Exponential interval matrices**

After taking into account the uncertainties in the joint variables (position, direction and angle), the evaluation of the overall precision is carried out based on exponential interval matrices.

Nevertheless, the counterpart of an easy representation of uncertainties with intervals parameters ( $Q$ ,  $P$  and  $\Omega$ ) is the numerical calculation of an exponential of interval matrix. Goldsztejn [61] proposed a computational method to calculate the exponential of an interval matrix, based on the truncated Taylor or Padé expansion (Horner-Taylor series) computed in double precision. Among the three methods to calculate such an exponential, this method minimizes the overestimation in the results [61]. This method is therefore employed here as it is well adapted to precision evaluation.

iii) **Set inversion via interval analysis (SIVIA)**

The process to find the space variables  $x$  by the intervals  $Q$  is directly addressed by using SIVIA (see Section 4.4.1.3) [?]. SIVIA formally states that, when given a nonlinear function from  $\mathfrak{R}^n$  to  $\mathfrak{R}^m$  and a set  $Y$  in  $\mathfrak{R}^m$ , the set  $X$  of solutions can be computed as  $X = \{x \in \mathfrak{R}^n \mid f(x) \in Y\} = f^{-1}(Y)$ .

#### 4.4.6 Implementation of the method on the proposed PiBot microrobot

The evaluation of the precision presented above has been applied to the microrobot called PiBot.

i) **Inverse kinematics**

This section uses a remainder of the inverse kinematics of the microrobot PiBot that was detailed in Section 3.5.1. Thereby, by observing Figure 3.10 and given a feasible platform orientation, defined by the values of the passive-leg U-joint angles  $(\theta_1, \theta_2)$ , the mechanism configuration can be calculated by finding the intersection of a sphere centered at the point  $C_i$ ,  $i = 1, 2$ , with radius  $|B_i C_i|$  and the circle with center  $A_i$ , with radius  $|A_i B_i|$ , in a plane normal to the line  $A_1 A_2$ . Thus, to find the implicit equation of the microrobot PiBot which is shown in Figure 3.10 we proceed as follows.

On the one hand,

$$\overrightarrow{PC}_i = \begin{bmatrix} R(\theta_1, \theta_2) & 0_{3 \times 1} \\ 0_{1 \times 3} & 1 \end{bmatrix} \overrightarrow{PC}_i|_{uvw} = H_1(\theta_1, \theta_2) \quad (4.20)$$

where  $\overrightarrow{PC}_i$  and  $\overrightarrow{PC}_i|_{uvw}$  are the homogeneous coordinates representing the vectors linking  $P$  and  $C_i$  expressed in the reference system fixed at the point  $P$  parallel to  $x, y, z$  and  $u, v, w$  respectively.  $R$  is the rotation matrix given by (4.21).

$$R(\theta_1, \theta_2) = R_x(\theta_1)R_y(\theta_2) = \begin{bmatrix} c_2 & 0 & s_2 \\ s_1 s_2 & c_1 & -s_1 s_2 \\ -c_1 s_2 & s_1 & c_1 c_2 \end{bmatrix} \quad (4.21)$$

where  $c_1 = \cos \theta_1$ ,  $s_1 = \sin \theta_1$ ,  $c_2 = \cos \theta_2$ ,  $s_2 = \sin \theta_2$ .

On the other hand,

$$\overrightarrow{PC}_i = \overrightarrow{PA}_i + \overrightarrow{A_iB}_i + \overrightarrow{B_iC}_i = H_2(q_i) \quad (4.22)$$

where  $\overrightarrow{PA}_i$  is a constant, and  $\overrightarrow{A_iB}_i = T_{PB}B_i|_A - A_i|_P$ ,  $\overrightarrow{B_iC}_i = T_1T_2C_i|_B - T_1T_2B_i|_B$ . We have  $T_{PB}$ ,  $T_1$  and  $T_2$  the homogeneous transformation matrices relative to the transformation between the coordinates of the joints of the robot and the coordinate system fixed at  $P$ , parallel to  $x$ ,  $y$  and  $z$  containing the joint variables  $q$ .

As consequence from (4.20) and (4.22), we obtain:

$$T(\theta_1, \theta_2)\overrightarrow{PC}_i|_{uvw} = (A_i - P) + (T_{PB}B_i|_A - A_i|_P) + (T_1T_2C_i|_B - T_1T_2B_i|_B) \quad (4.23)$$

Thus, for any desired operational angles  $\theta_1$  and  $\theta_2$ , (4.23) permits to find the joint variables  $q$ . This equation gives a large space of solution but only physically possible solutions are considered in our calculations. By physically possible solutions, we mean solutions reachable by the actuator. According to the actuators performance, only some physically possible solutions are considered in our calculations.

## ii) Applying Uncertainties as Intervals

Imposing intervals in the variables of position, direction and angle of (4.22), yields:

$$[\overrightarrow{PC}_i] = [\overrightarrow{PA}_i] + [\overrightarrow{A_iB}_i] + [\overrightarrow{B_iC}_i] \quad (4.24)$$

where square brackets denote interval vectors.

- In the left part of (4.24) we have

$$[\overrightarrow{PC}_i] = T(\Theta_1, \Theta_2)\overrightarrow{PC}_i|_{uvw} \quad (4.25)$$

where,  $\Theta_1$  and  $\Theta_2$  are intervals denoting the uncertainties of the mobile platform orientation of the microrobot and

$$T(\Theta_1, \Theta_2) = \begin{bmatrix} R(\Theta_1, \Theta_2) & 0_{3 \times 1} \\ 0_{1 \times 3} & 1 \end{bmatrix} \quad (4.26)$$

where  $R(\Theta_1, \Theta_2)$  is an interval matrix associated to (4.21).

- Furthermore, as  $\overrightarrow{PA}_i$  are fixed points on the support of the robot and are not prone to uncertainties, we trivially have

$$[\overrightarrow{PA}_i] = \overrightarrow{PA}_i = A_i - P \quad (4.27)$$

where  $\overrightarrow{PA}_i$  are fixed points in the support of the robot and does not show uncertainties that we are evaluating. Indeed, uncertainties of the fabrication of the base are fixed and do not change when the robot moves.



- The second vector of (4.24) is expressed by

$$[\overrightarrow{A_i B_i}] = [B_i] - [A_i] = T_{PB} e^{\hat{\Xi}_2 Q_2^i} e^{\hat{\Xi}_3 Q_3^i} B_i|_A - A_i|_P \quad (4.28)$$

- Finally, the third vector of (4.24) by

$$[\overrightarrow{B_i C_i}] = [C_i] - [B_i] = T_1 e^{\hat{\Xi}_1 Q_1^i} T_2 e^{\hat{\Xi}_2 Q_2^i} e^{\hat{\Xi}_3 Q_3^i} C_i|_B - T_1 e^{\hat{\Xi}_1 Q_1^i} T_2 e^{\hat{\Xi}_2 Q_2^i} e^{\hat{\Xi}_3 Q_3^i} B_i|_B \quad (4.29)$$

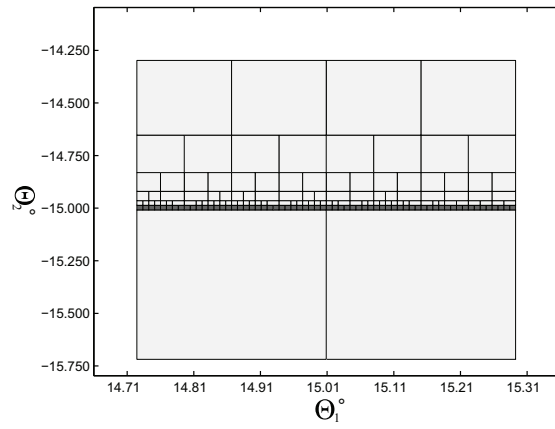
where  $e^{\hat{\Xi}_j Q_j^i}$  is the interval matrix exponential which takes into account the uncertainties in the joint angle ( $Q_j^i$ ) and in the joint axis position and direction ( $\hat{\Xi}_j$ ),  $T_1^i$  (resp.  $T_2^i$ ) is a constant homogeneous transformation between the reference frames attached to points  $P$  and  $A_i$  (resp.  $A_i$  and  $B_i$ ),  $C_i|_B$  are the homogeneous coordinates of the point  $C_i$  expressed in the reference frame attached to point  $B_i$ .

Finally, replacing (4.25), (4.27), (4.28) and (4.29) into (4.24) yields:

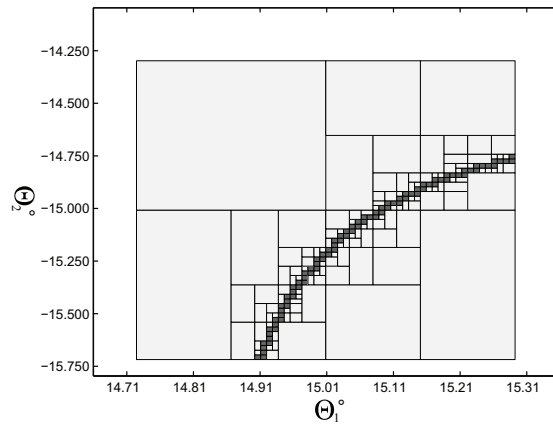
$$T(\Theta_1, \Theta_2) \overrightarrow{PC_i}|_{uvw} = (A_i - P) + (T_{PB} e^{\hat{\Xi}_2 Q_2^i} e^{\hat{\Xi}_3 Q_3^i} B_i|_A - A_i|_P) + (T_1 e^{\hat{\Xi}_1 Q_1^i} T_2 e^{\hat{\Xi}_2 Q_2^i} e^{\hat{\Xi}_3 Q_3^i} C_i|_B - T_1 e^{\hat{\Xi}_1 Q_1^i} T_2 e^{\hat{\Xi}_2 Q_2^i} e^{\hat{\Xi}_3 Q_3^i} B_i|_B) \quad (4.30)$$

### iii) Results

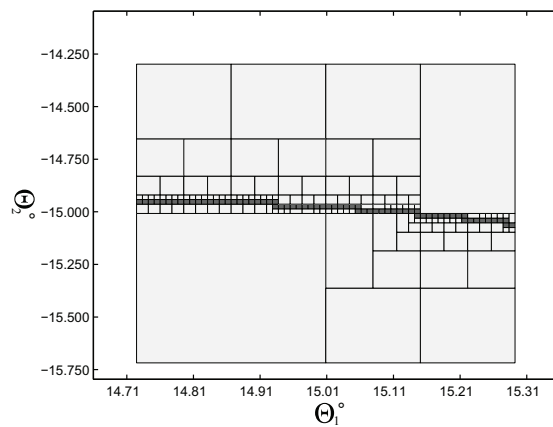
With (4.30) the process to find  $\Theta_1$  and  $\Theta_2$  by the intervals  $Q_i$  is directly addressed by using the SIVIA algorithm. In our case, we identify:  $X = \{\Theta_1, \Theta_2\}$ ,  $Y = \{Q_i\}$  and  $f^{-1}$  which is the inverse kinematics interval model. Thus, this part presents the interval solution that represents the precision at the end-effector. The INTLAB [155] Matlab toolbox was used to perform the interval calculations.



(a)



(b)



(c)

FIGURE 4.18: Result of the components of (4.24) by SIVIA algorithm (a) of the first component. (b) of the second component. (c) of the third component.

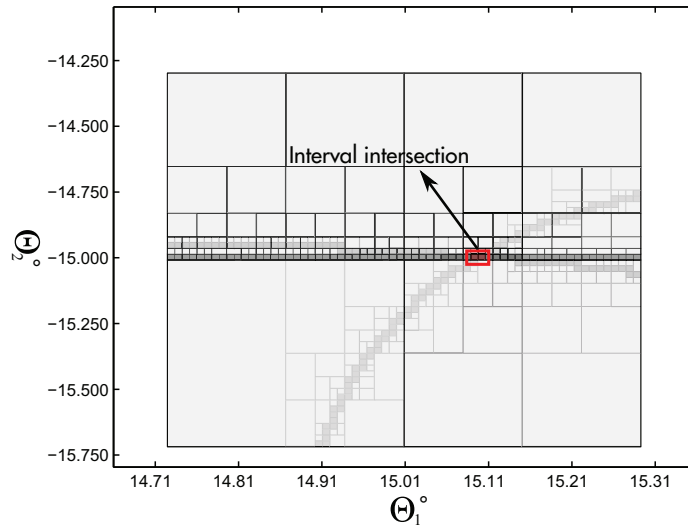


FIGURE 4.19: Outcome of the intersection of all the three solutions shown above.

Figure 4.18a, 4.18b and 4.18c show the solution of each of the three components of (4.30). Figure 4.19 is the region that belongs to the intersection of the three solutions respectively associated to each component of (4.30). The solution set  $S_c$  correspond to  $\Theta_1$  and  $\Theta_2$  that may take the platform orientation. In Figure 4.19, the uncertainties of the angle  $\Theta_1$  are bounded in an interval of width  $0.02^\circ$  and those of  $\Theta_2$  are bounded in an interval of width  $0.01^\circ$ . These uncertainties in the platform of the PKM directly result in uncertainties on the spot laser projected onto the vocal fold. Due to the mirror placed on the platform of the robot, the uncertainties are twice more on the vocal folds<sup>2</sup>. For a working distance of 20 mm between the platform and the vocal fold, the uncertainties are in the order of  $14 \mu\text{m}$ .

The results shown in Figure 4.20 are obtained by running the same algorithm for different sets of coupled angles i.e.,  $(15^\circ, 15^\circ)$ ,  $(-15^\circ, 15^\circ)$ ,  $(-15^\circ, -15^\circ)$  and  $(0^\circ, 0^\circ)$ . Each plot in the figure shows the interval intersection result. The intersection is computed using the individual component plots generated by SIVIA and (4.30). The platform response has been tested at the extreme tilts and at zero-tilt. From the obtained results, it is clear that the interval intersection is large at the origin of the tilting axis which clearly states the existence of higher uncertainties (unwanted movements) at  $(0^\circ, 0^\circ)$ . The maximum uncertainties found in the result obtained for different sets of coupled angles are intervals of width  $0.10^\circ$  (Figure 4.20d). When employing the platform to orient a laser beam onto a vocal fold distanced at 20 mm, the related scanning uncertainties are about  $70 \mu\text{m}$  which remain acceptable for the targeted phonomicrosurgery task. Figure 4.20(a,b, and c) shows the solution set  $S_c$  for which the extremal configuration of the platform is assured.

<sup>2</sup>Any angle developed by the mirror is the half of the angle developed by the laser beam.

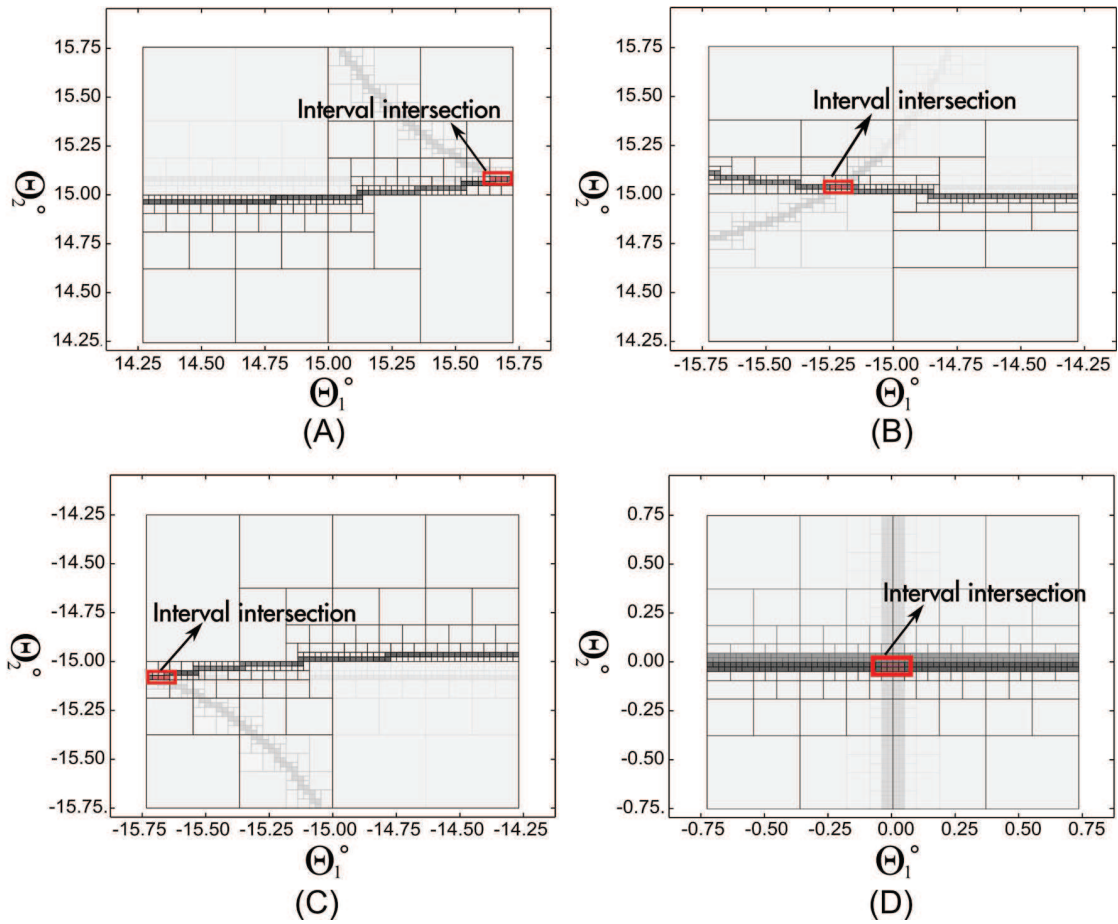


FIGURE 4.20: Algorithm performed to several angles (A)  $(\theta_1, \theta_2) = (15^\circ, 15^\circ)$  (B)  $(\theta_1, \theta_2) = (-15^\circ, 15^\circ)$  (C)  $(\theta_1, \theta_2) = (-15^\circ, -15^\circ)$  (D)  $(\theta_1, \theta_2) = (0^\circ, 0^\circ)$

## 4.5 Conclusions

This chapter deals with the SCM fabrication technique and its utilization to build the two proposed microrobots. An analysis of the errors of positioning caused by the fabrication was evaluated on one of the fabricated prototypes.

First, the details of the SCM fabrication technique were explained, such as materials to be used with this technique and the process steps to follow. Moreover, it was shown that this technique is well adapted to the fabrication of parallel kinematic structures since it allows to create structures using unactuated joints. This parallel kinematics structures created using the SCM technique can be mixed with piezoelectric cantilevers actuators to generate the displacements required. Furthermore, conventional joints and their equivalences made with SCM process were presented.

Afterwards, we presented the fabrication of the two microrobots. CAD design and fabrication outcome are presented for each microrobot.

Finally, an analysis of the errors of positioning of the microrobots caused by the SCM fabrication process was presented using interval analysis.

The contributions of this chapter are: i) the appropriation of the recent SCM fabrication technique; ii) the realization of two unprecedented microrobots, one being the miniature version of the Agile Eye and the other having an unpublished kinematic structure; iii) the proposition of a method for forecasting the accuracy of PKM's made of flexure joints, by extension of a method published in the case of serial kinematic structures; iv) and, incidentally, the confirmation that the proposed microrobot should be able to reach the expected accuracy for laser phonomicrosurgery.

# Chapter 5

## Control

*This chapter deals with the experimental performances, the characterization and the control of one the developed microrobots. The Micro Agile-Eye, which has a more complex structure than the other proposed microrobot, was tested in a closed loop control scheme. A feedback using vision was used in order to estimate the microrobot Cartesian variables which are the two orientation degrees of freedom of the microrobot platform. This estimation is computed from the position of a laser spot which is projected onto a screen, driven by the microrobot and captured by two cameras. Nonlinearities and badly damped oscillations due to the piezoelectric cantilever actuators were modeled and compensated using feedforward control. Then, merging the feedforward control scheme and the feedback using cameras, the controlled microrobot was tested with different input reference signals. Finally a comparison between the two schemes, i.e., the feedback only and the feedforward-feedback combined, was analyzed.*

### Chapter contents

---

<b>5.1</b>	<b>Introduction</b>	<b>104</b>
<b>5.2</b>	<b>Classical visual servoing control</b>	<b>104</b>
5.2.1	Experimental setup	105
5.2.2	Experimental results	107
<b>5.3</b>	<b>Feedforward compensation of vibrations and hysteresis</b>	<b>110</b>
5.3.1	General principle of feedforward control	113
5.3.2	Experimental Setup: Interferometer	120
5.3.3	Experimental results	121
<b>5.4</b>	<b>Visual servoing and feedforward compensation combined</b>	<b>127</b>
5.4.1	Experimental results	127
5.4.2	Step response	128
<b>5.5</b>	<b>Conclusion</b>	<b>133</b>

---

## 5.1 Introduction

In this chapter the Micro Agile-Eye microrobot is characterized and controlled. The microrobot is equipped with a mirror which is glued on its platform. Then, a laser beam which is reflected by this mirror is generated using a laser pointer. Thus, the direction of the reflected laser beam is driven by the orientation given by the microrobot platform. The reflected laser beam is projected onto a screen forming a laser spot at some 20 cm of distance from the mirror. The position of this laser spot is detected by two cameras. Using the position of the laser spot, the two orientations (angles about “x” and “y”-axes) of the platform are computed. Then, the microrobot is controlled using a classical visual servoing control scheme. This will be presented in Section 5.2. Furthermore, nonlinearities such as hysteresis which is originally caused by the piezoelectric cantilever actuators are identified and then compensated for. The same procedure is applied to compensate for the badly damped oscillations. These compensations are performed by using feedforward control schemes. This will be presented in Section 5.3. In addition, the feedforward controlled microrobot is augmented by a feedback scheme. This will be presented in Section 5.4. Finally, the performances of the classical visual servoing only scheme and the coupled scheme based on the feedforward compensation and the visual servoing, are compared using performances index based on the errors.

## 5.2 Classical visual servoing control

Visual servoing or vision-based robot control was defined and explained in Section 2.6.4 and it is used in this section. A closed loop control scheme was implemented using the feedback signal given by two cameras, as depicted in Figure 5.1 and explained now. To acquire the position of the laser spot, classical techniques based on epipolar geometry were implemented [69]. The signal is afterwards used to correct the position of the laser spot compared with the input reference. A proportional derivative controller (PD) is used for that. The Jacobian of the optical system ( $J_{opt}$ ) is used to decouple the control law signal after the PD controller to obtain the angular velocities of the platform required to correct the position of the laser spot. Notice that  $J_{opt}$  is a matrix which relates the laser spot rates ( $\dot{x}$ ,  $\dot{y}$ ) to the angular velocities of the platform ( $\dot{\theta}_1$ ,  $\dot{\theta}_2$ ). The inverse kinematics of the microrobot ( $J_{rob}$ ) is used to decouple the two required angular velocities of the platform to obtain the associated joint velocities and thereby to correct the position of the laser spot. Notice that  $J_{rob}$  is a matrix which relates the angular velocities of the platform ( $\dot{\theta}_1$ ,  $\dot{\theta}_2$ ) to the joint variables velocities ( $\dot{\delta}_1$ ,  $\dot{\delta}_2$ ). Both Jacobians  $J_{opt}$  and  $J_{rob}$  require the actual values of the platform orientation ( $\theta_1$  and  $\theta_2$ ). To do so, we used  $G_{opt}$ , the inverse static kinematic model of the optical system that provides the angles of the platform ( $\theta_1$ ,  $\theta_2$ ) given a position of the laser spot onto the screen ( $x,y$ ). Note also that an integrator is used before sending the signal to the actuators due to the fact that the piezoelectric cantilevers actuators are controlled in position (contrary to the motors used in macro robotics that are driven in velocities, i.e., a velocity is given when a voltage is applied). Finally, the correction signal ( $\delta_{r1}$  and  $\delta_{r2}$ ) is sent to the actuator to modify the laser spot position. The complete scheme is depicted in Figure 5.1.

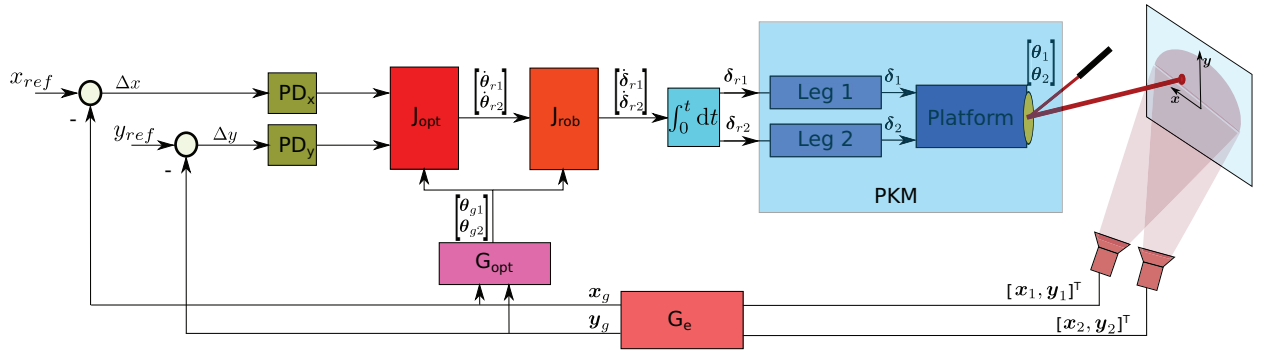
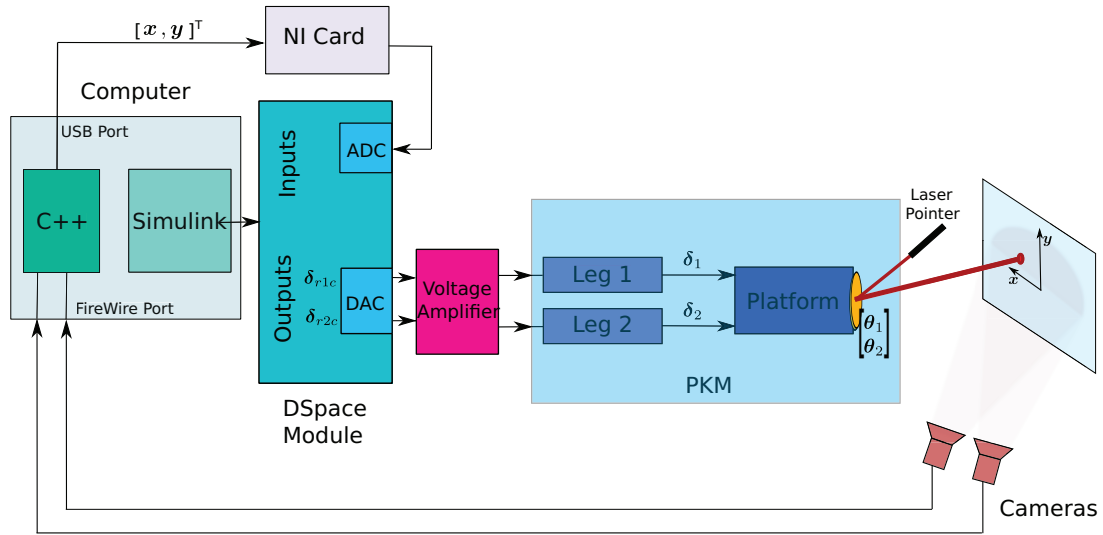


FIGURE 5.1: Control using visual feedback.

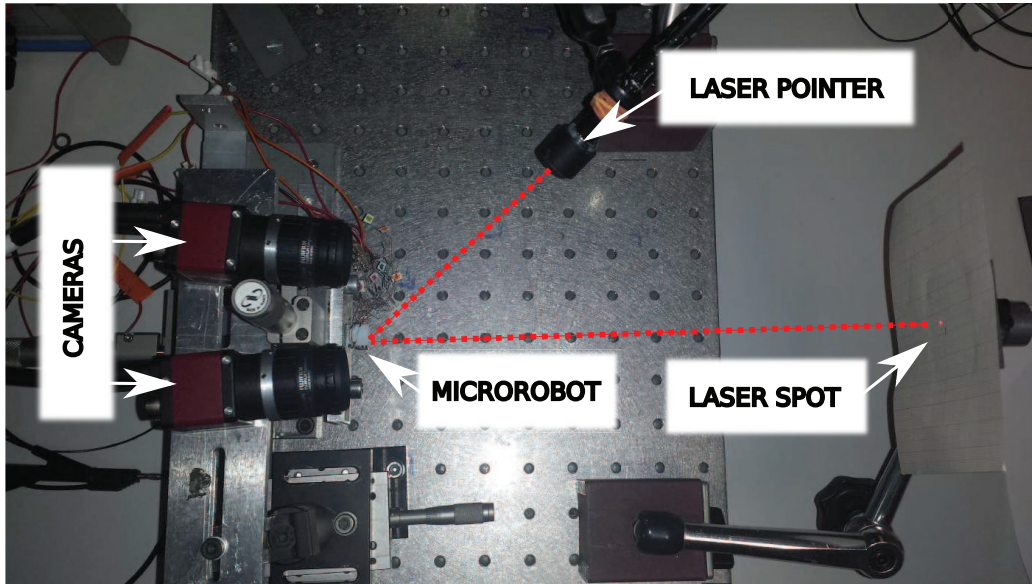
### 5.2.1 Experimental setup

Figure 5.2b depicts the experimental setup, where the two legs of the microrobot (each leg being composed of three piezoelectric cantilever actuators) are driven by high-voltage ( $\pm 100 V_{max}$ ) amplifiers (FLC Electronic model A400DI). A dSPACE module with 32 bits DAC and ADC channels is used to produce an analog voltage, which is then amplified by the high-voltage amplifier. Tilts in the  $x$  and  $y$ -axes of the orientable platform generate a change of the laser beam direction sent by a laser pointer. The laser spot is projected onto a screen located 20 cm from the surface of the mirror manipulated/orientable/steered by the microrobot. The displacement of the spot onto the screen is measured by two cameras (Guppy pro model:GPF 033B ASG - E0030013) set to work at 25 frames/s. The position is calculated with respect to the center of the platform by a computer (with a program in C++ using the library ViSP). That computed position is sent to a National Instrument card (NI model: USB-6211 with 250kS/s) externally installed via USB connection. Then the desired piezoelectric cantilever deflection, in an equivalent analog voltage, is sent to an analog input of the dSPACE module. Moreover, Matlab Simulink software is employed to implement the control scheme. Finally, the implemented system is embedded in the dSPACE microprocessor to perform real-time control using ControlDesk running at 1 kHz. Notice that the dSPACE module does not allow to manage the Guppy drivers (cameras), therefore the processing of images was performed by a C++ program, then the result was sent through the NI card as an input signal to the dSPACE module.





(a) Experimental setup to perform the control by visual servoing classical control.



(b) Detail of the experimental setup.

FIGURE 5.2: Experimental setup.

## 5.2.2 Experimental results

This section presents the experimental results which were obtained with the setup described above, i.e., using vision-based feedback to close the loop. First, step responses of the controlled microrobot are evaluated independently for both axes. Then, the hysteresis in each axis of the controlled microrobot is evaluated. Finally, the microrobot is controlled to trace complex spatial reference trajectories: a circle, a spiral and a Lissajous trajectory. Notice that the values of the controller gains were  $K_{px} = 40$ ,  $K_{dx} = 12$  and  $K_{py} = 50$ ,  $K_{dy} = 10$  for the x-axis and y-axis respectively. The sampling time was limited by the cameras and set to 10 Hz.

### 5.2.2.1 Step response

Each independent orientation of the platform is reflected onto the screen as a translation of the laser spot onto the projection plane. Thanks to the decoupled kinematics, the two translations direction are also decoupled. First, a step reference signal with 10 mm of amplitude is sent to the system for the x-axis, and later for the y-axis. Then, the response to that input signal is recorded by the vision-based capture system, as depicted in Figure 5.3 and in Figure 5.4 for the x-axis and for the y-axis respectively. An analysis of these figures shows that the closed-loop system is limited in bandwidth due to the cameras. Thereby, high dynamics are not observed. In both figures the sampling time used by the cameras is about 0.1 second, i.e., a sampling frequency of 10 Hz. The response time to the step is approximately 3.2 ms and 2.5 ms for the x-axis and y-axis respectively. In both axes the static error is about 1%. Improvement of these responses can be achieved using cameras with a high working frequency.

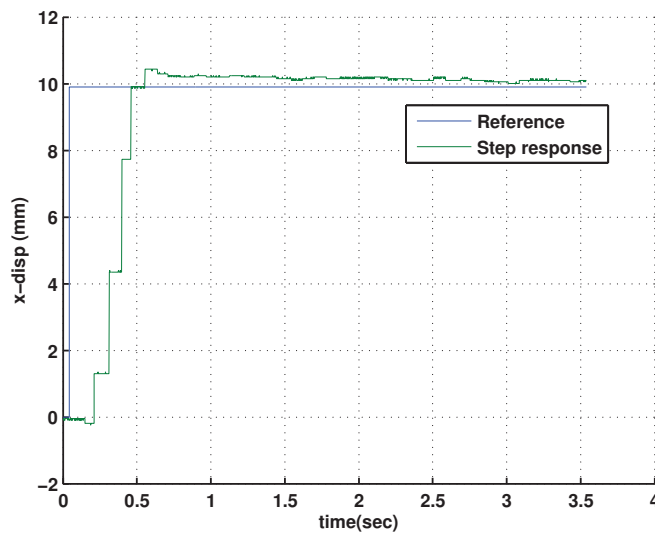


FIGURE 5.3: Step response of the controlled microrobot along the x-axis.

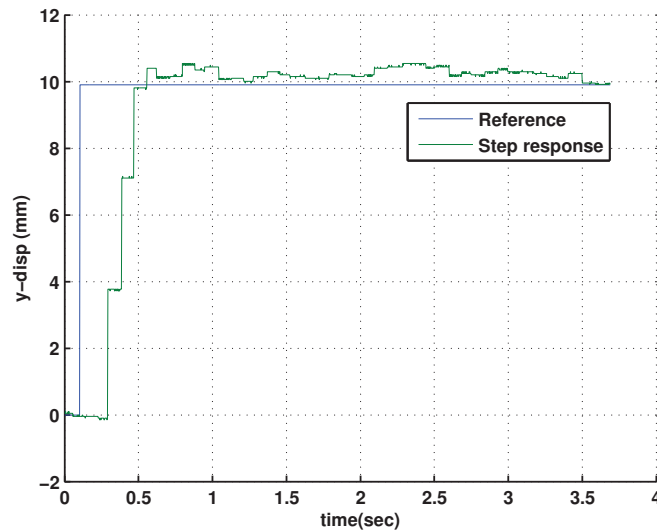


FIGURE 5.4: Step response of the controlled microrobot along the y-axis.

### 5.2.2.2 Complex spatial trajectory tracking

The controlled microrobot is now tested with three complex spatial trajectories: i) a circle, ii) a spiral iii) and a Lissajous curves. Each of them is described below.

#### Circular trajectory tracking

A coordinated and independent reference input signal is sent to the controlled microrobot system. For this experience, each axis is supplied with a sinusoidal input signal. Their equations are:  $x_n = \hat{X} \sin(2\pi ft)$  and  $y_n = \hat{Y} \cos(2\pi ft)$ , where  $\hat{X} = \hat{Y} = 10$  mm is the radius and  $f = 0.1$  Hz is the frequency. The result is depicted in Figure 5.5a. In that figure we can note that, in the low part of the circle, the tracking has not a good fit and the control law was not enough. The hysteresis as first hypothesis is planted as the cause of that misfit.

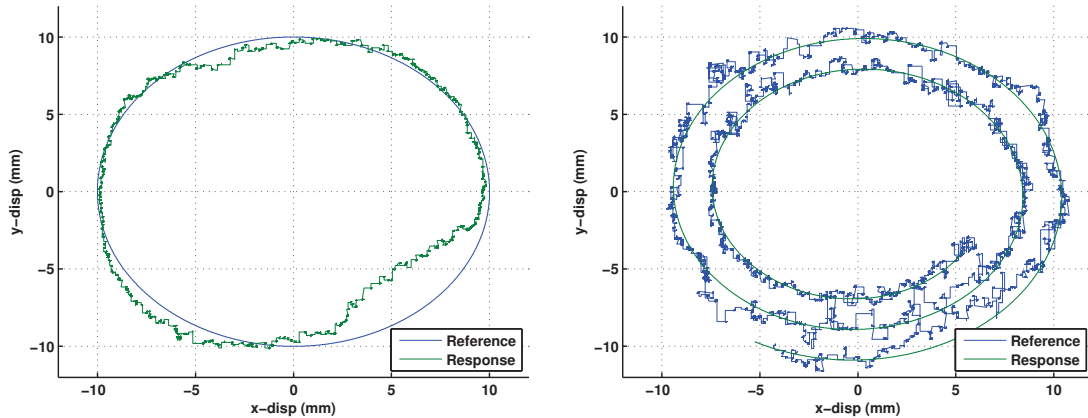
#### Spiral trajectory tracking

For this experience, each axis is supplied by a sinusoidal signal with a variable amplitude. The amplitude is gradually increased from 5 mm to 10 mm. Thus, the trajectory generated is a spiral, as depicted in Figure 5.5b. The time to generate that spiral is 15 seconds. In the figure, the misfit increases with the increasing distance of the path to the center.

#### Lissajous trajectory tracking

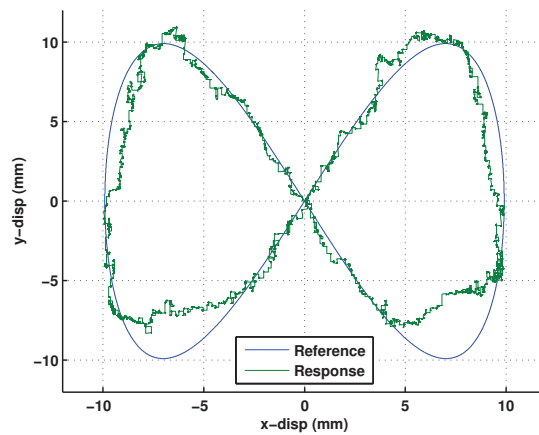
Finally, each axis is supplied by a sinusoidal signal with different frequency. The frequency in the y-axis is twice the frequency of the signal supplied to the x-axis. Thus, the path generated is a Lissajous figure, as depicted in Figure 5.5c. The amplitude of each sinusoidal signal is 10 mm, while the frequencies are 0.24 Hz and 0.12 Hz in the y-axis and x-axis respectively

which corresponds to a ratio of  $\frac{f_y}{f_x} = 2$ . In the figure, again we can note that in the low part of the trajectory, the tracking has not a good fit and the control law was not enough. Once again, *a priori* the hysteresis of the actuators is the principal cause of that misfit.



(a) Tracking of a circle trajectory.

(b) Tracking of a spiral trajectory.



(c) Tracking of a Lissajous trajectory.

FIGURE 5.5: Complex trajectory tracking using visual servoing.

### 5.2.2.3 Hysteresis analysis

The hysteresis of the controlled microrobot system is depicted in Figure 5.6a and in Figure 5.6b for the x-axis and the y-axis respectively. These hysteresis are obtained by applying a sine input reference along one axis and by letting the other axis null. The frequency used to generate a complete cycle was 10 Hz and the amplitude of each sinusoidal signal was 10 mm. The hysteresis obtained in both axes are asymmetric.

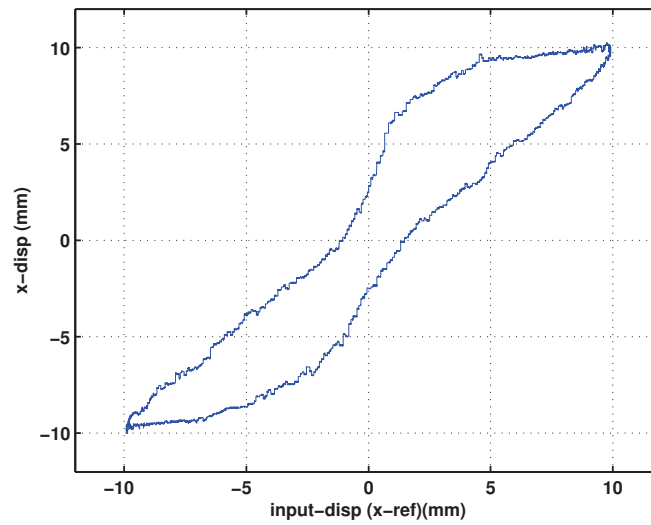
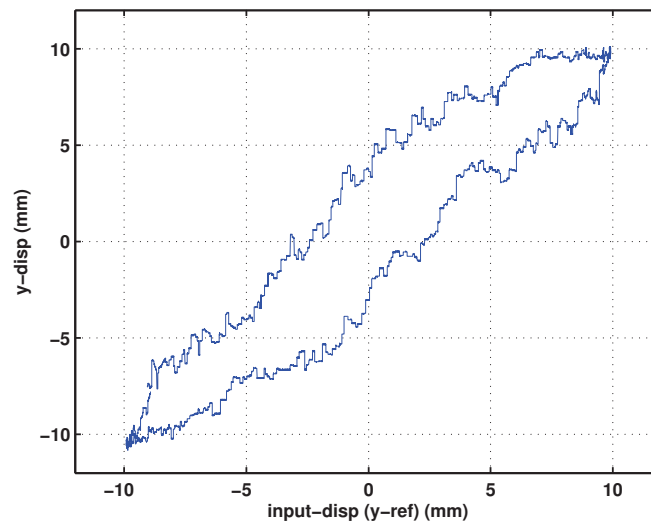
(a) Hysteresis of the controlled microrobot system for the  $x$ -axis.(b) Hysteresis of the controlled microrobot system for the  $y$ -axis.

FIGURE 5.6: Hysteresis of the controlled microrobot using visual servoing.

### 5.3 Feedforward compensation of vibrations and hysteresis

As expected, piezoelectric actuators offer many advantages, however they exhibit unwanted nonlinearities. The nonlinearities are mainly hysteresis and creep. They affect the final performances of the whole robotic system. Moreover, they can affect the stability and precision

whether they are not well accounted for or represented in the closed-loop. First, a brief description of these two nonlinearities is given below.

**Hysteresis:** This nonlinearity is defined in [116] as a path-dependent memory effect where the output relies not only on the current state but also on the past output history. Hysteresis is highly present in piezoelectric materials as was described in [143, 68]. The observation of the hysteresis is carried out by applying a sine voltage signal with a fixed frequency to the piezoelectric cantilever actuator, then the output displacement is recorded.  $\frac{h}{H}\%$  is the amplitude of the hysteresis, as shown in Figure 5.7.

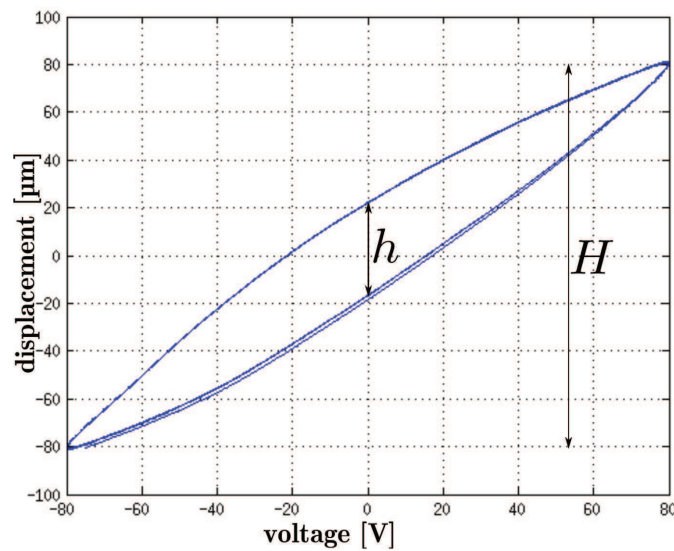


FIGURE 5.7: Hysteresis obtained from a piezoelectric cantilever actuator from [145].

**Creep:** This phenomenon is defined as the progressive time-dependent inelastic deformation of materials under constant load and temperature [123]. The observation of the creep is done by applying a step voltage to the piezoelectric cantilever actuator and recording the resulting output for a long period, as shown in Figure 5.8. In our system we did not take into account this nonlinearity because their slow effect is compensated by the visual feedback.

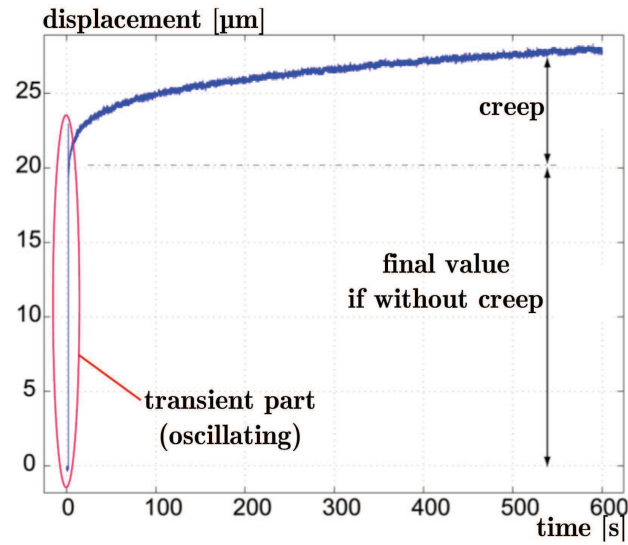


FIGURE 5.8: Creep obtained from a piezoelectric cantilever actuator from [145].

Another effect that decreases the high performance of our microrobot system is the unwanted vibrations caused by the badly damped oscillations which are found in the non-recessed part of piezoelectric cantilever actuator. Characteristic oscillation at the end of the piezoelectric cantilever actuators is shown in Figure 5.9. This oscillation is associated with high Q-factor (quality factor) and with poles with large imaginary parts. In consequence this oscillation extends the settling time (even if bandwidth is high) and strongly compromises the stability of the final task.

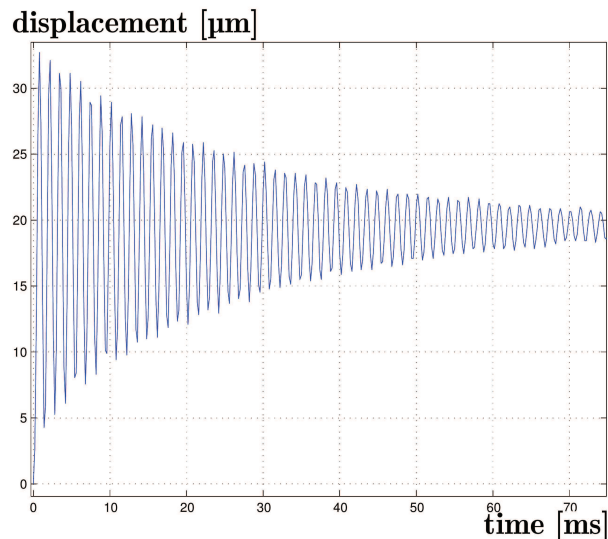


FIGURE 5.9: Oscillation obtained when applying a step excitation to a piezoelectric cantilever actuator from [145].

### 5.3.1 General principle of feedforward control

The objective of a feedforward control is to lead  $\delta$  equal to the reference  $\delta_r$  without using sensors. The controller, called compensator is in cascade with the system, as shown in Figure 5.10. The implementation of a feedforward control requires no additional hardware or sensors which decreases the costs of implementation. This point is interesting when installing sensors inside the structure can increase the uncertainty of the measure, increase the disturbance influence, or is even impossible. This latter is the case of microdevices. However this approach requires an accurate knowledge of the undesirable behaviors. Thereby, a full characterization of those behaviors should be done first.

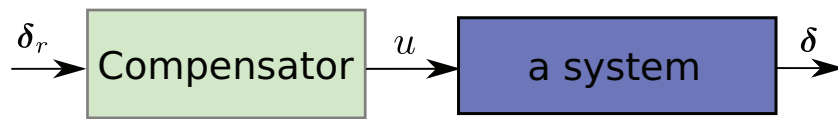


FIGURE 5.10: Feedforward control of one actuated leg of the micro-robot.

The microrobot has two legs which are directly linked to the orientation of the platform, and the orientation of the platform modifies the laser spot position. In our microrobot, we have identified two systems: i) the right leg which provides the displacement of the laser spot in the y-axis, ii) and the left leg which provides the displacement of the laser spot in the x-axis. Thus, we have decided to compensate first for the unwanted vibration and then to compensate for the hysteresis.

#### 5.3.1.1 Vibrations compensation

Many studies have been carried out regarding the compensation of badly damped vibrations. Figure 5.11 gives a synthesis of these methods [143].

Basic methods as rate limiter or low pass filter can efficiently decrease the vibrations but increase the rise time and decreasing the bandwidth of the controlled system. Methods based on inversion require conditions in the model before calculating the compensator (bi-causality, bi-stability). Most of these methods can maintain the rise time and the bandwidth but are not generally valuable for non minimum phase systems (systems with unstable zeros) that in case of complex structures using piezoelectric actuators could obtain unstable zeros. In Zero Magnitude Error Tracking Control (ZMETC), non-minimum phase (with unstable zeros) can be handled but the system should be discrete. Input-Shaping methods have been used in robotics for many years, the basic method being the Posicast [166, 75] which decomposes the command input amplitude into two steps. There are different kinds of input shaping methods, a panorama of the existing methods is given in [165]. Zero-Vibrations Input Shaping (ZVIS) is a generalization of the Posicast method and is described below.

**Zero-Vibrations Input Shaping** This is a technique to minimize the vibration in badly damped systems and it was presented by Singer in [164]. This method is based on the convolu-



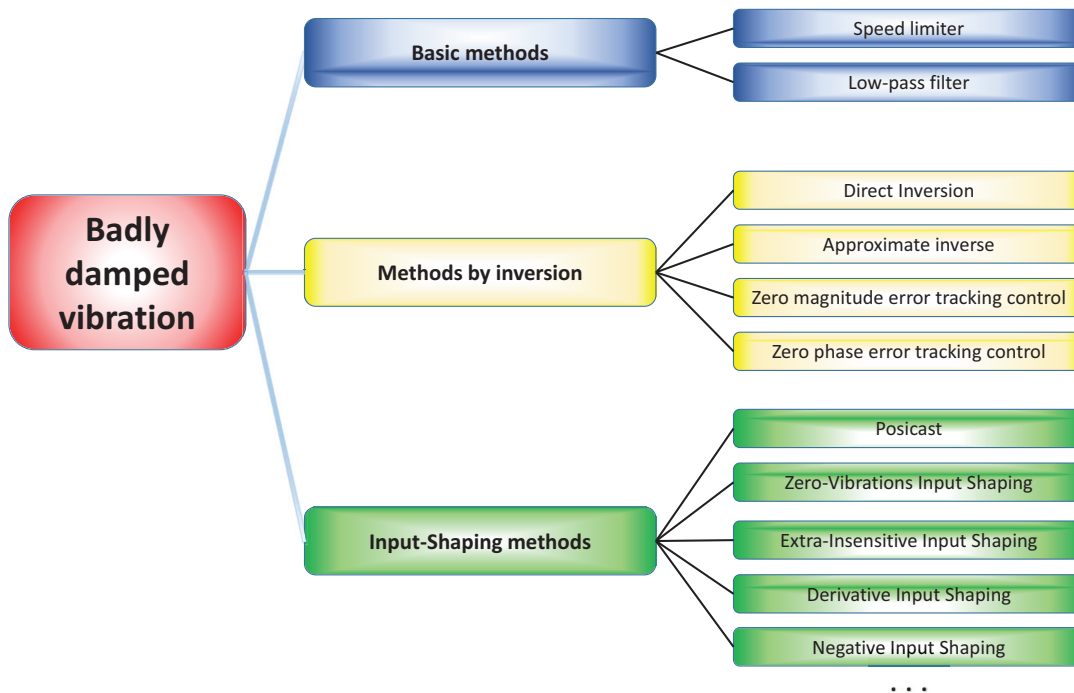


FIGURE 5.11: Vibration compensation methods.

tion of several impulses with the input reference signal. Recently [144, 145] it has been applied to compensate for vibrations in piezoelectric cantilever actuators. In our case, we will compensate for the undesirable vibrations generated by an array of piezoelectric cantilevers. The compensator in input shaping techniques is also called “*Shaper*”.

If a badly damped oscillating system is excited by an impulse input, a vibration appears with  $\omega_n$  as natural frequency and  $\xi$  as the damping ratio. Then if this system is excited by a second impulse input at time  $T_d = T/2$ , with  $T = \frac{2\pi}{\omega_n \sqrt{1-\xi^2}}$ , then the two vibrations (caused by the first and the second impulse input) can cancel each other out if the impulses amplitudes were conveniently chosen, as shown in Figure 5.12. For any reference input  $\delta_r$  is applied, this is convolved with the shaper, as shown in Figure 5.13.

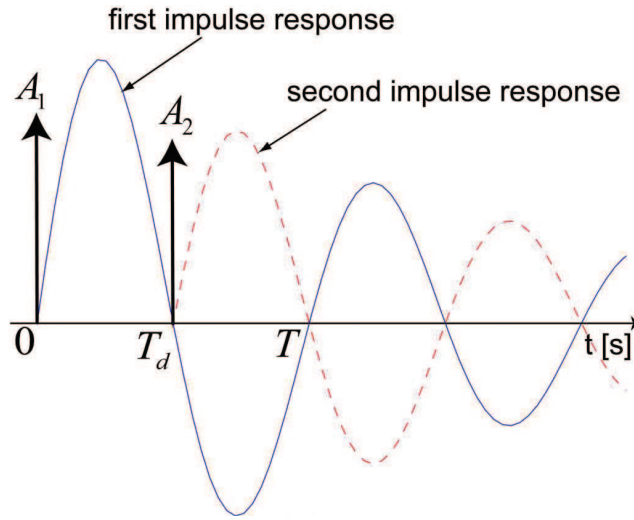


FIGURE 5.12: Two impulses applied to a badly damped system.

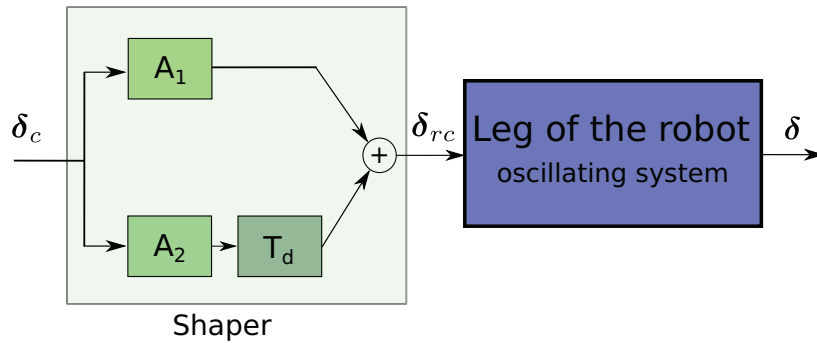


FIGURE 5.13: Block diagram of the Zero-Vibration-Input-Shaping technique.

The identification step (to get  $\omega_n$  and  $\xi$ ) should be precise enough to reach a zero residual vibrations after compensation. If there are uncertainties on the used  $\omega_n$  or  $\xi$ , a high number of impulses in the shaper should be used to minimize the residual vibrations.

The computation of the shaper is explained below.

Let the transfer function of the system:

$$\frac{\delta}{\delta_c} = \frac{K}{\left(\frac{1}{\omega_n}\right)^2 s^2 + \left(\frac{2\xi}{\omega_n}\right)s + 1} \quad (5.1)$$

where  $K$  is the static gain of the system.

Now, consider  $A_i$  the amplitudes of the impulses and  $t_i$  their applications times. Thus, each vibration caused by each impulse has the following time-domain equation:

$$\delta_i = KA_i \frac{\omega_n}{\sqrt{1-\xi^2}} e^{-[(t-t_i)\xi\omega_n]} \sin \omega_n \sqrt{1-\xi^2}(t-t_i) \quad (5.2)$$

The objective is to have:

$$\sum_{i=1}^m \delta_i(t) = 0 \quad (5.3)$$

where  $m$  is the number of impulses in the shaper block.

The calculation of the amplitude of each impulse must ensure the positivity and the normalization condition:

$$A_i > 0 \text{ and } \sum_{i=1}^m A_i = 1 \quad (5.4)$$

Thus, considering  $\beta = e^{-\frac{\xi\pi}{1-\xi^2}}$ , the solution of  $A_i$  and  $t_i$  is:

$$A_i : \begin{pmatrix} A_1 = \frac{a_1}{(1+\beta)^{m-1}} \\ A_2 = \frac{a_2}{(1+\beta)^{m-1}} \\ \dots \\ A_m = \frac{a_m}{(1+\beta)^{m-1}} \end{pmatrix} \text{ and } t_i : \begin{pmatrix} t_1 = 0 \\ t_2 = T_d \\ \dots \\ t_m = (m-1)T_d \end{pmatrix} \quad (5.5)$$

where  $m$  is the number of impulses in the shaper,  $a_i$  indicates the  $i^{\text{th}}$  monomial of the polynomial from  $(1+\beta)^{m-1}$ . We have  $a_1 = 1$  and  $a_m = \beta^{m-1}$

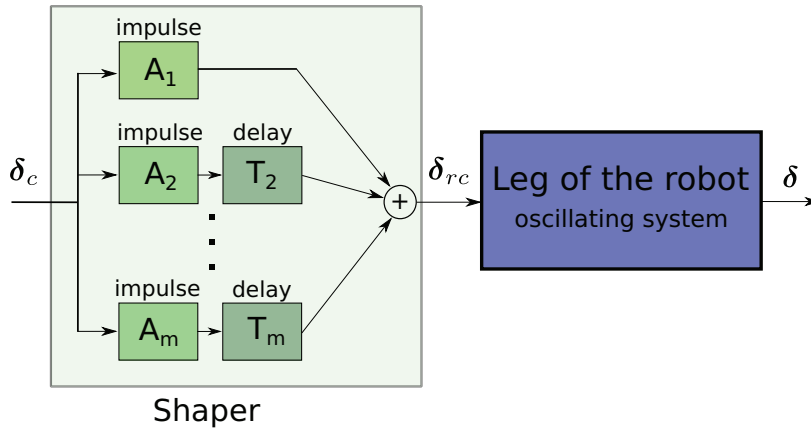


FIGURE 5.14: Complete block diagram of the Zero-Vibration-Input-Shaping with “ $m$ ” impulses.

### 5.3.1.2 Hysteresis compensation

To compensate for the hysteresis the first step is its identification and characterization. Many authors have modeled the hysteresis following different approaches [116, 82]. A synthesis of these methods is given in Figure 5.15.

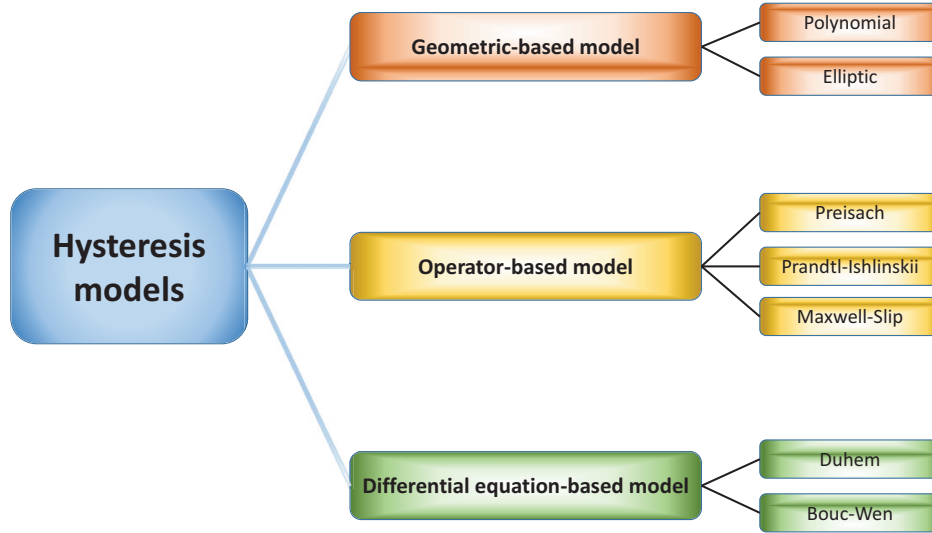


FIGURE 5.15: Hysteresis models.

Geometric models are simple in equation structures (polynomial, elliptical, quadrilateral). The principal limitation is their non validity when the input signal is changed in amplitude or in frequency. Operator-based models such as Preisach, Prandtl-Ishlinskii consist in approximating the complex hysteresis as the superposition of basic elements called hysterons. Differential-equations based models include Duhem and Bouc-Wen approaches. These methods are based on nonlinear differential equations. Recently Bouc-Wen model has been successfully used to model the hysteresis in piezoelectric materials [142, 168, 68]. The advantages of the Bouc-Wen method are: i) the simplicity of its few equations, ii) and the convenience to treat asymmetric hysteresis. Then, due to the asymmetry of the hysteresis in our microrobot (see Figure 5.6), we propose to use the generalized Bouc-Wen approach to model the hysteresis and then to calculate the compensator.

**Generalized Bouc-Wen:** The generalized Bouc-Wen model is a set of equations which relate force and material deformation, as follows [168]:

$$\begin{cases} f(x, \dot{x}, z) = \alpha k_0 x + (1 - \alpha) k_0 z \\ \dot{z} = \dot{x} [A - |z|^m \psi(x, \dot{x}, z)] \end{cases} \quad (5.6)$$

where  $f$  is the resisting force,  $x$  and  $\dot{x}$  are the deformation and the velocity of deformation respectively,  $\alpha$  is the stiffness ratio of the structure,  $k_0$  is one initial value of the stiffness, and  $z$

is a variable denoting the structure inelastic behavior.  $\psi$  is the hysteresis shape control function which for Bouc-Wen model is represented by (5.7).

$$\psi(x, \dot{x}, z) = \beta_1 \text{sgn}(\dot{x}) + \beta_2 \text{sgn}(x\dot{x}) + \beta_3 \text{sgn}(xz) + \beta_4 \text{sgn}(\dot{x}) + \beta_5 \text{sgn}(z) + \beta_6 \text{sgn}(x) \quad (5.7)$$

where  $\beta_i$  with  $i = 1..6$  are constants controlling the shape of the hysteresis.

To adapt equations (5.6) to the case of piezoelectric cantilever actuators: the driving signal  $x$  is replaced with the voltage  $U$  and the bending displacement  $f/k_0$  is  $\delta$ . Parameter  $m$  is assumed to be 1. Thus, equation (5.6) and (5.7) become:

$$\begin{cases} \delta = kU - z \\ \dot{z} = \dot{U}[A - |z|\psi] \end{cases} \quad (5.8)$$

with

$$\psi = \beta_1 \text{sgn}(\dot{U}z) + \beta_2 \text{sgn}(U\dot{U}) + \beta_3 \text{sgn}(Uz) + \beta_4 \text{sgn}(\dot{U}) + \beta_5 \text{sgn}(z) + \beta_6 \text{sgn}(U) \quad (5.9)$$

The identification of the Generalized Bouc-Wen model is as follows. First, one periodic sinusoidal signal input voltage  $U$  is applied. Then the output displacement  $\delta(k)^{exp}$  due to this voltage  $U(k)^{exp}$  is captured (the exponent “ext” denote that is a experimental data). Finally the system is identified offline by using the experimental data  $U(k)^{exp}$  and  $\delta(k)^{exp}$  and equation (5.8). The following least square optimization is proposed for that:

$$\begin{cases} \min \left( \sum_{k=1}^N (\delta(k) - \delta(k)^{exp})^2 \right) \\ \delta(k) = KU(k)^{exp} - z(k) \\ \dot{z} = \dot{U}(k)^{exp}[A - |z(k)|\psi] \end{cases} \quad (5.10)$$

where  $\dot{z} = \frac{z(k) - z(k-1)}{\Delta T}$ ,  $\dot{U}(k) = \frac{U(k) - U(k-1)}{\Delta T}$  and  $\Delta T$  is the sampling time.

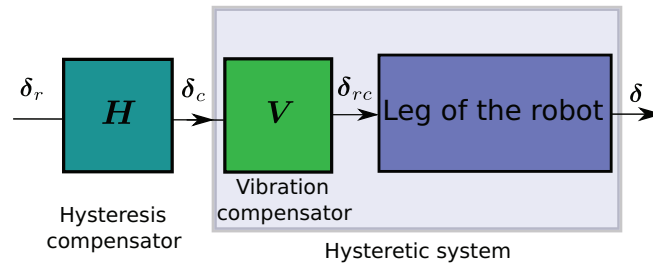


FIGURE 5.16: Block diagram of a feedforward control to cancel the hysteresis behavior.

Having identified the hysteresis model, a compensator to this identified hysteresis can be calculated. The compensator is built in such a way that the general feedforward controlled system, as depicted in Figure 5.16, satisfies the following condition:

$$\delta_r = \delta \tag{5.11}$$

where  $\delta_r$  is the desired reference. Introducing (5.11) in (5.8) yields:

$$\delta_r = K\delta_c - z \tag{5.12}$$

Thus, the compensator is obtained as:

$$\delta_c = K^{-1}(\delta_r + z) \tag{5.13}$$

with  $\dot{z} = \dot{U}(k)^{exp}[A - |z(k)|\psi]$

Figure 5.17 depicts the block diagram of the hysteresis compensator with the system and with the vibration compensator.

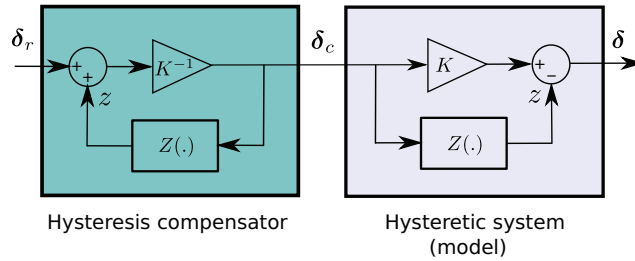


FIGURE 5.17: Generalized Bouc-Wen hysteresis compensator.

where  $Z(\cdot)$  denotes a nonlinear operator characterized by the second equation of (5.8). The control signal  $\delta_c$  is the output of the hysteresis compensator and the desired displacement  $\delta_r$  is its input.

To summarize, the feedforward compensation of each leg is done in cascade, as shown in Figure 5.18.

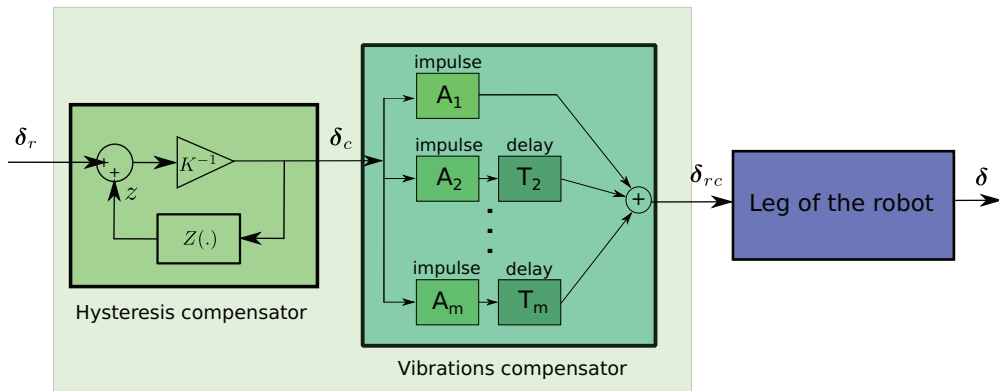


FIGURE 5.18: Compensation of vibration and hysteresis of a robot leg.

### 5.3.2 Experimental Setup: Interferometer

Using standard cameras, as was presented in Section 5.2, all the fast dynamics of the micro-robot are not observed (including nonlinear behaviors and badly damped oscillations). This is due to the low working frequency of the cameras. Unfortunately, due to the time/schedule constraints of the collaborative project ( $\mu$ RALP) our high-speed camera was not available. However, to develop a feedforward compensator, the fast dynamics of the microrobot system must be characterized and therefore must be measured. Thereby, to characterize the hysteresis and the badly damped oscillations of the microrobot, a 1DoF interferometer was installed near to the microrobot platform, as shown in Figure 5.19. Note that in this situation the presence of the interferometer impedes the use of the cameras at the same time.

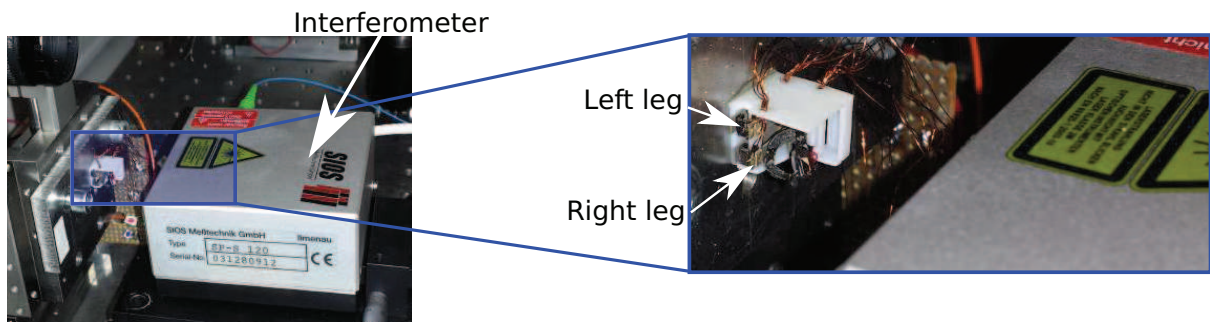


FIGURE 5.19: Interferometer for the measurement of the displacement of each leg of the micro-robot.

Figure 5.20 depicts the schematic principle of the experimental setup. The two legs of the microrobot (each leg formed by three piezoelectric cantilever actuators) are driven by a high-voltage amplifier (FLC Electronic model A400DI). A dSPACE module with 32 bits DAC and ADC channels is adapted to produce an analog voltage, which is then amplified by the high-voltage amplifier. The output displacement of each leg is measured by the interferometer (SIOS Mestechnik GmbH model: SP-S 120). This interferometer has the capability to measure displacements with high frequencies (10 kHz). The analog voltage output of the interferometer which is proportional to the displacement, is acquired by the computer through one ADC channel of the dSPACE module. Moreover, Matlab Simulink software is employed to implement the control scheme and then to embed it in the dSPACE microprocessor to perform realtime control.

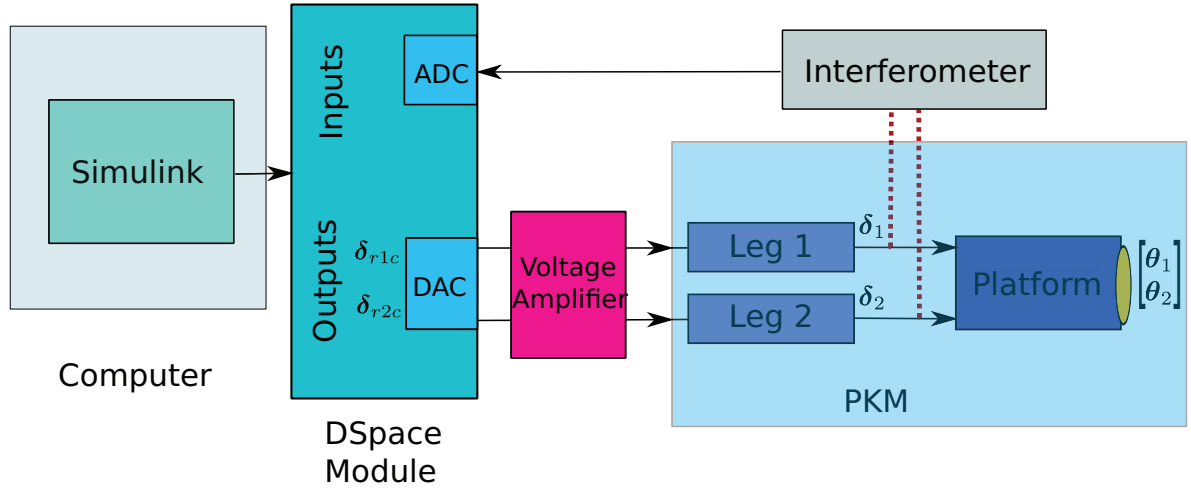


FIGURE 5.20: Diagram of the experimental setup for the characterization of fast dynamics of the microrobot legs.

### 5.3.3 Experimental results

First, the badly damped oscillations in each leg were modeled and then compensated. After that, the hysteresis of the new system composed by the vibrations compensator in series with the robotic structure (leg of the robot) was modeled and controlled. The sampling time of the whole system was set to 1 kHz. The different results are presented below.

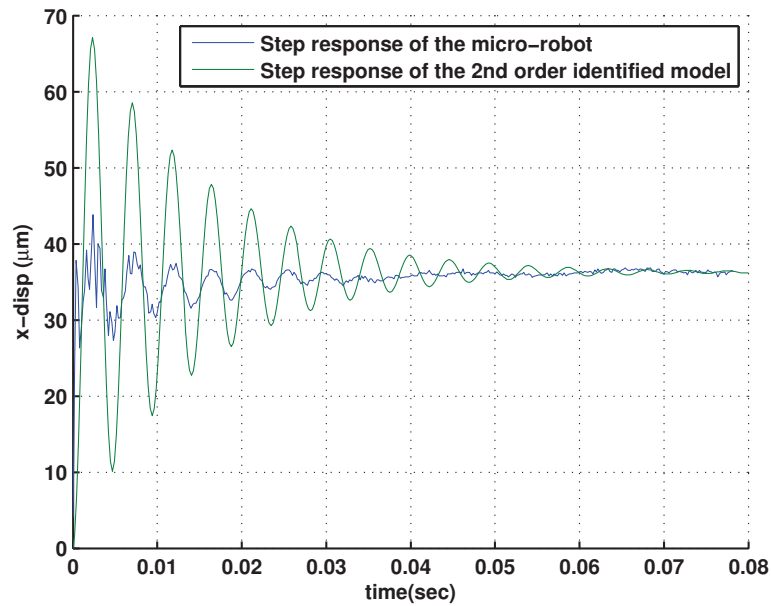
#### 5.3.3.1 Vibrations compensation results

To compensate for the badly damped oscillation of each leg, the Zero-Vibration Input Shaping method is used. A description of the procedure is given below.

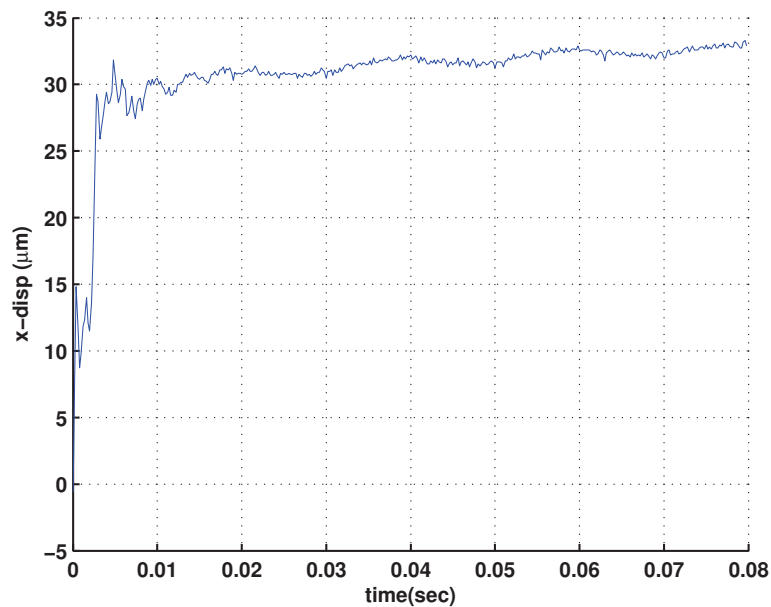
##### Control of the left leg

To characterize the oscillation presented at the tip of the left leg, a step input voltage is applied. Figure 5.21a shows the result. Then a 2nd-order model was identified. In fact, to exactly fit the real system, at least a 7th order should be used. However, the Zero-Vibration Input Shaping method is based on a 2nd-order model. In Figure 5.21a the identified system is also shown, which evidences a good fit in frequency but not in amplitude. Nevertheless this 2nd-order is used to synthesize the feedforward compensator. The compensated system is shown in Figure 5.21b. As we can see, the compensated system presents less amplitude of the oscillations than the system without compensation. In spite of this residual oscillation of 50 Hz depicted in Figure 5.21, the system performance is improved.





(a) Step responses of the real robotic system and of the 2nd-order approximate model (identified) corresponding to the left leg.

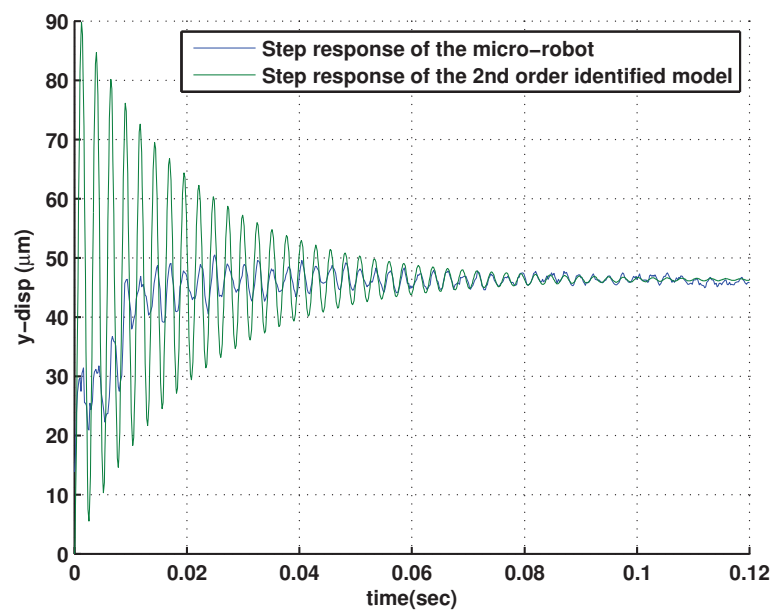


(b) Step responses of the real system after the feedforward compensation for the left leg.

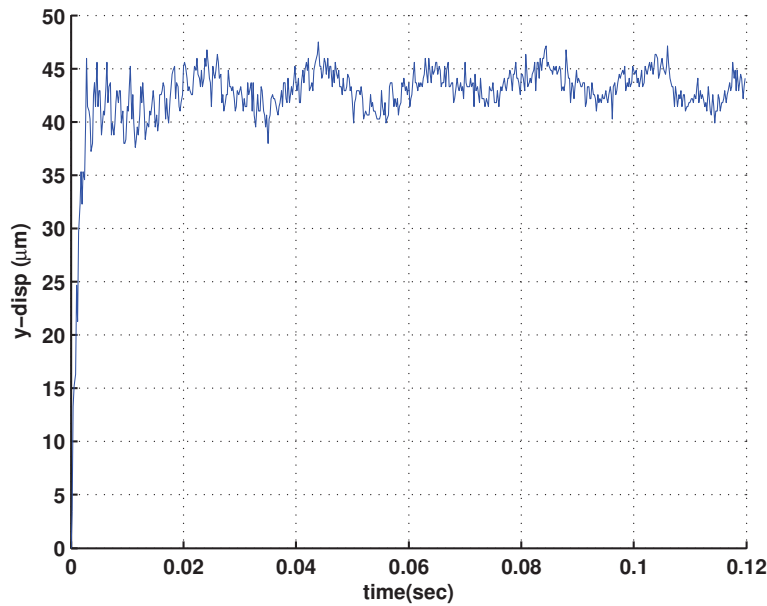
FIGURE 5.21: Feedforward compensation of badly damped oscillation in the left leg.

### Control of the right leg

The same procedure as for the left leg is applied here. Figure 5.22a depicts the step response of the leg, as well as the step response of the identified 2nd order model. The compensated system is shown in Figure 5.22b. Once again, the compensated system shows less amplitude of the oscillation than the system without compensator. However evidence a residual oscillation of amplitude  $5 \mu\text{m}$  and  $50 \text{ Hz}$  depicted in Figure 5.22. In practice the system was improved decreasing the response time from 0.02 second to 0.004 second.



(a) Step responses of the real robotic system and of the 2nd-order approximate model (identified) corresponding to the right leg.



(b) Step response of the real system after the feedforward compensation for the right leg.

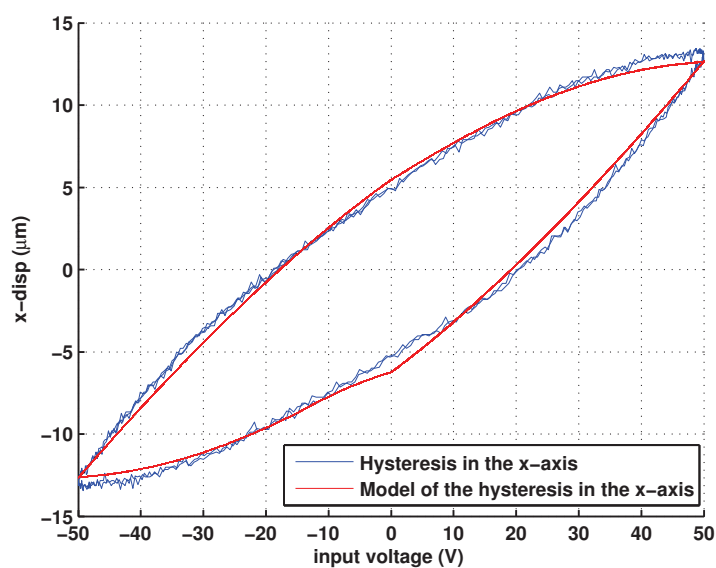
FIGURE 5.22: Feedforward compensation of badly damped oscillations in the right leg.

### 5.3.3.2 Hysteresis compensation results

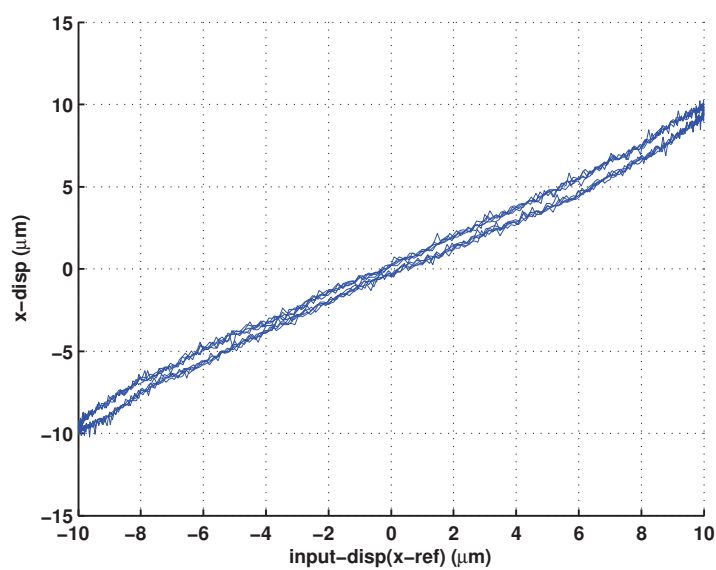
To compensate for the hysteresis of each leg, the generalized Bouc-Wen is used. A description of the procedure is presented below. Notice that the system to be compensated is a compound of the leg itself augmented with the vibrations feedforward compensator. To characterize the hysteresis, the interferometer is still used and the sampling frequencies still left at 1 kHz. The hysteresis is obtained by using a sine input with a frequency of 10 Hz.

#### Control of the left leg

Figure 5.23a depicts the hysteresis of the left leg. An identification procedure of the generalized Bouc-Wen model carried out with the hysteresis. The simulation of the identified model is also pictured in the same figure which shows a convenience of this model. After calculating the compensator for the model, it is implemented. Figure 5.23b shows the experimental results of the compensated system. As we can see, the hysteresis is highly reduced.



(a) Experimental hysteresis and model simulation for the left leg.

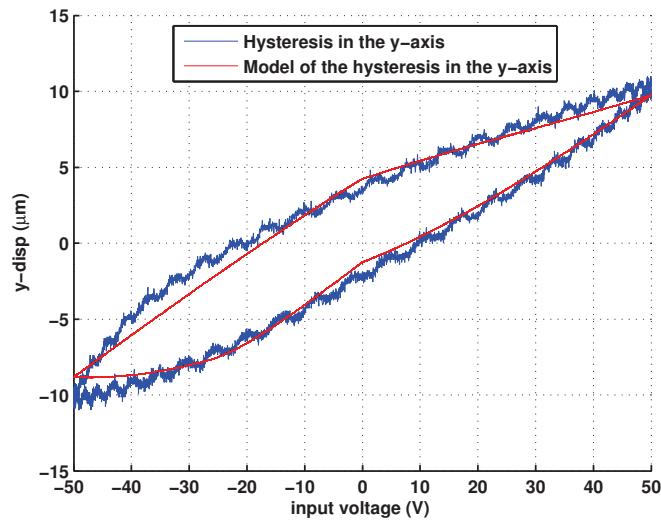


(b) Response when applying the hysteresis compensator.

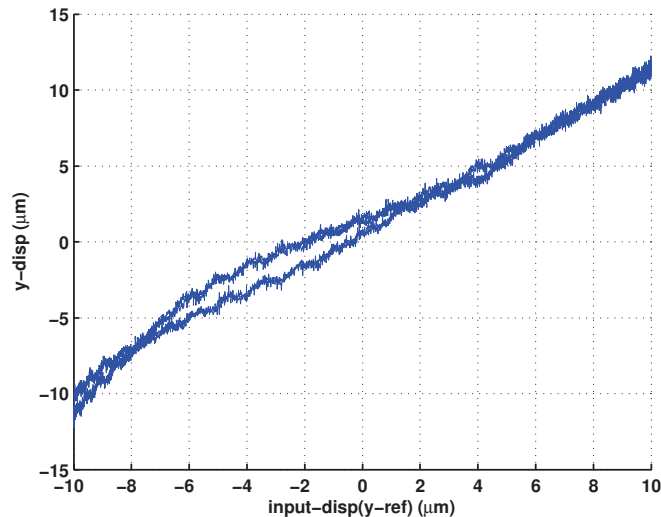
FIGURE 5.23: Feedforward compensation of the hysteresis of the system composed by the vibrations compensator and the left leg.

### Control of the right leg

The same procedure than for the left leg is carried out here. Figure 5.24a depicts the experimental hysteresis and the simulated identified generalized Bouc-Wen model, which shows a good adequacy. Then a compensator is calculated and implemented. The results are shown in Figure 5.24b which demonstrates a high reduction of the hysteresis. Nevertheless residual oscillations are evidenced in both figures (before and after compensation), showing that the hysteresis compensator has no affect on the remaining badly damped oscillations of the vibration compensator.



(a) Experimental hysteresis and model simulation for the right leg.



(b) Response when applying the hysteresis compensator.

FIGURE 5.24: Feedforward compensation of the hysteresis of the system composed by the vibrations compensator and the right leg.

## 5.4 Visual servoing and feedforward compensation combined

In this section, we combine the previous feedforward compensation with the classical visual servoing control. As far as we know this is the first time that visual servoing and feedforward compensation of piezoelectric actuators are combined to control a  $1 \text{ cm}^3$  microrobot. Figure 5.25 depicts the new diagram of the controlled microrobotic system. The unique difference with the classical visual servoing control is the feedforward compensation schemes. These feedforward compensators were synthesized in the precedent section and are now integrated in the whole closed loop: compare Figure 5.25 with Figure 5.1.

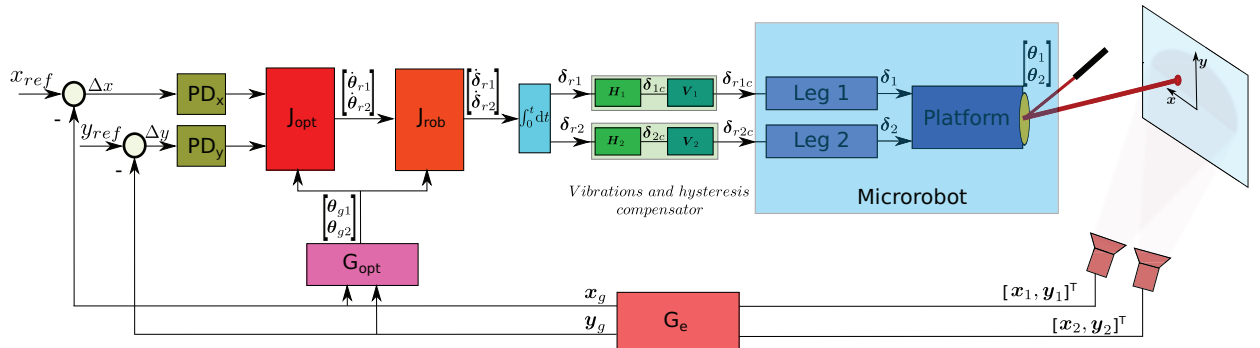


FIGURE 5.25: Diagram of the classical visual servoing and the feedforward control combined.

### 5.4.1 Experimental results

This section presents the experimental results which were obtained with the setup described above, i.e., the closed loop control using feedforward compensation with vision-based feedback. Using the individual axis feedforward compensation of vibration and hysteresis of the piezoelectric cantilever presented in previous section the microrobot is controlled to trace a more complex spatial trajectory: a circle, a spiral and a Lissajous trajectory. Finally the hysteresis of the closed loop system is evaluated. To perform these experiences, the setup is the same as the one described in Section 5.2.1: two cameras, a dSPACE card, a NI card, voltage amplifiers. Notice that the values of the controller gains decreased to  $K_{px} = 10$ ,  $K_{dx} = 3$  and  $K_{py} = 12$ ,  $K_{dy} = 2.5$  for the x-axis and y-axis respectively. This drop of the controllers gains values are due to the static gains which are contributed by the feedforward compensators. The sampling time was still limited by the cameras and kept to 10 Hz.

### 5.4.2 Step response

A step reference signal of 10 mm of amplitude (point-to-point displacement) is sent to the system, for the  $x$ -axis and for the  $y$ -axis independently. Then, the step response is captured thanks to the vision-based system, as depicted in Figure 5.26 and in Figure 5.27 for the  $x$ -axis and for the  $y$ -axis, respectively. Both figures do not show improvements relative to the control without the feedforward controllers. This is because the measurement (cameras) strongly limits the bandwidth of the system. In both figures the sampling time used by the cameras is of 0.1 seconds, i.e., 10 Hz of sampling frequency.

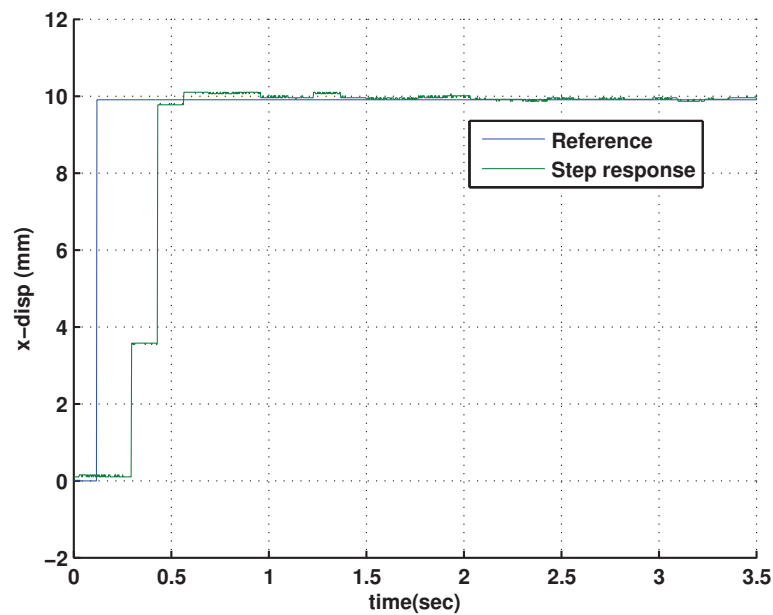


FIGURE 5.26: Step response along  $x$ -axis of the system controlled by visual servoing and feedforward techniques combined.

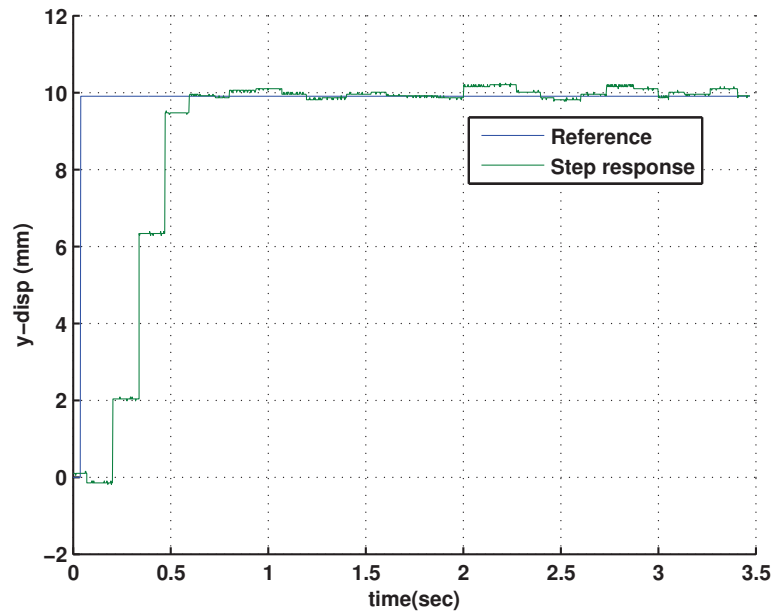


FIGURE 5.27: Step response along y-axis of the system controlled by visual servoing and feedforward techniques combined.

#### 5.4.2.1 Complex spatial trajectory tracking

The controlled microrobot is now tested with three complex spatial trajectories: i) a circle, ii) a spiral iii) and a Lissajous curves. Each of them is described below.

##### Circle tracking

A coordinated and independent reference input signal is now sent to the controlled microrobot system. For this experience, each axis is supplied with a sinusoidal input signal. Their equations are:  $x_n = \hat{X}\cos(2\pi ft)$  and  $y_n = \hat{Y}\cos(2\pi ft)$ , where  $\hat{X} = \hat{Y} = 10$  mm is the radius and  $f = 0.1$  Hz is the frequency. The result is depicted in Figure 5.28a.

In that figure we can note that the trajectory has a relative good fit compared with the system without feedforward compensator. Therefore, with the piezoelectric actuators free of hysteresis, the whole controlled microrobot system shows an improvement in the tracking of the circle.

##### Spiral tracking

For this experience, each axis is supplied by a sinusoidal signal with a variable amplitude. The amplitude is gradually increased from 5 mm to 10 mm. Thus, the trajectory generated is a spiral, as depicted in Figure 5.28b. The time to generate that spiral is 15 seconds. Similarly to the circle an improvement in the tracking of the spiral is evidenced thanks to the feedforward controllers.



### Lissajous curve tracking

Finally, each axis is supplied by a sinusoidal signal with different frequency. The frequency in the  $y$ -axis is twice the frequency of the signal supplied to the  $x$ -axis. Thus, the path generated is a Lissajous figure, as depicted in Figure 5.5c. The amplitude of each sinusoidal signal is 10 mm, while the frequencies are 0.24 Hz and 0.12 Hz in the  $y$ -axis and  $x$ -axis respectively which corresponds to a ratio of  $\frac{f_y}{f_x} = 2$ . In the figure, again we can note an improvement in the low part of the trajectory thanks to the feedforward compensation. Nevertheless a residual misfit still remains in this figure which could be compensated using other appropriated control strategies as for instance  $H_{inf}$ .

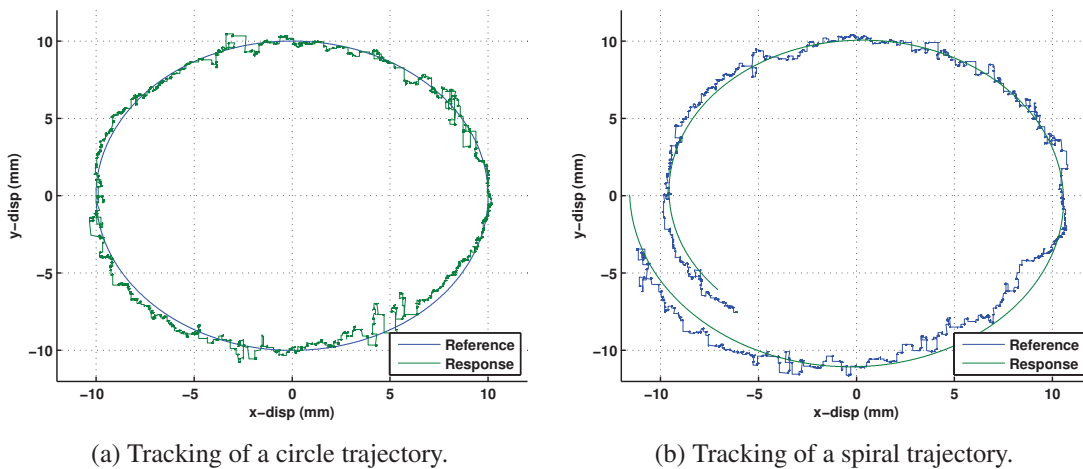


FIGURE 5.28: Complex trajectory tracking using visual servoing coupled with feedforward compensation.

A synthesis and quantification of the improvements is evidenced thanks to Table 5.4.2.1. It underlines that errors are in order of a millimeter for a screen placed at some 200 mm distance

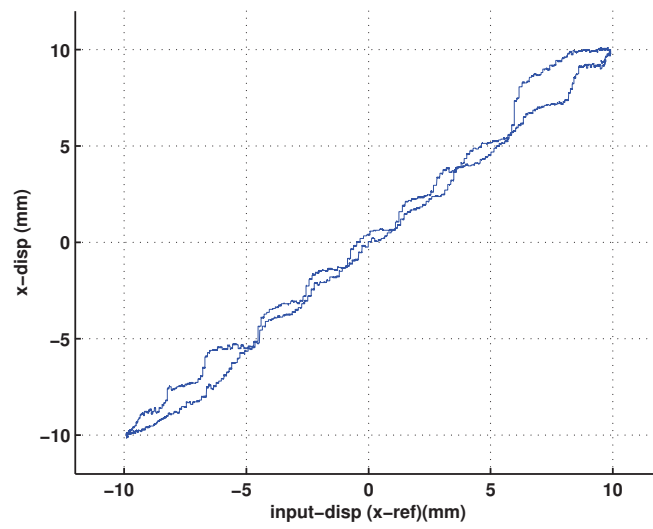
from the microrobot. This means that in the case of laryngeal operation, the errors should be in order of  $100 \mu\text{m}$  which is the expected accuracy. Note also that using a faster camera should improve the performances because fast dynamics will be rejected faster.

	<b>Visual servoing</b>			<b>Visual servoing + feedforward compensation</b>		
	<i>RMS</i> (mm)	<i>max</i> (mm)	<i>median</i> (mm)	<i>RMS</i> (mm)	<i>max</i> (mm)	<i>median</i> (mm)
<b><i>Circle</i></b>	3.4241	5.6422	3.3142	1.3001	2.501	1.1769
<b><i>Spiral</i></b>	1.3129	3.310	1.3234	1.0788	3.0393	0.8506
<b><i>Lisajjous</i></b>	1.9115	4.5643	1.4023	0.5245	1.1423	0.4075

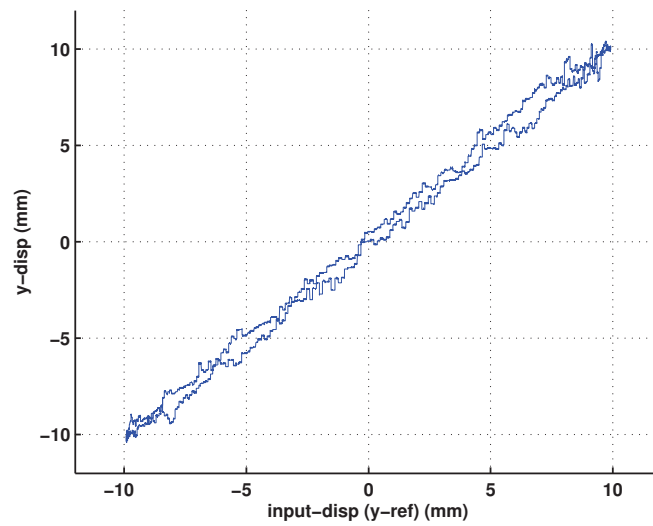
TABLE 5.1: Table of errors

#### 5.4.2.2 Hysteresis analysis

The hysteresis of the microrobot system in closed loop with feedforward compensation is depicted in Figure 5.29a and in Figure 5.29b for x-axis and y-axis respectively. The frequency used to generate the hysteresis cycle was 10 Hz and the amplitude was 10 mm. Those figures show that the hysteresis loop is also compensated in the closed loop control when using the feedforward compensation.



(a) Hysteresis of the controlled microrobot system for the  $x$ -axis.



(b) Hysteresis of the controlled microrobot system for the  $y$ -axis.

FIGURE 5.29: Hysteresis of the controlled microrobot using visual servoing coupled with feed-forward compensation.

## 5.5 Conclusion

This chapter presented the experimental results of the controlled microrobot. In the first section a control scheme based on visual servoing was used to control the position of the laser spot onto a screen. This is one of the rare cases of application of visual servoing to micro-PKMs. Then, in the second section, a feedforward compensator is synthesized for each leg, in order to decrease the hysteresis and badly damped oscillations effects that typify piezoelectric cantilever actuators. This is probably one of the first applications of piezoelectric compensation in complex kinematic structures. Finally, the third section presented the principal contribution of this chapter that consisted in coupling the visual servoing with the feedforward compensation to control the microrobot system.

The step response which was evaluated in the first and third section, could not be enhanced due to the low working frequencies of the cameras. Thus, the improvements of the system performance are not measurable with the current cameras. The test of complex tracking trajectories have shown considerable improvements after using the feedforward compensator and coupling that with the visual servoing.

However, although the robot allows high working frequencies (until about 200 Hz) the controlled microrobot system can not work at high frequencies. Those low frequencies are due to the fps using by cameras. For that, high speed cameras are expected to be used in a near future.



# Chapter 6

## Conclusions and perspectives

*This chapter gives the conclusions and perspectives of this thesis by reminding all contributions that have been carried out and by presenting some potential applications as well as future works in the medium and long terms.*

### Chapter contents

---

<b>6.1 Conclusions</b> . . . . .	<b>135</b>
<b>6.2 Perspectives</b> . . . . .	<b>136</b>

---

### 6.1 Conclusions

We have proposed the complete development, the kinematic analysis and the control of two parallel microrobots with the objective to perform laser surgery of the vocal folds. The works include the following stages:

- a) abstraction of the specifications,
- b) modeling,
- c) fabrication,
- d) evaluation of the precision,
- e) and control.

First, the abstraction of the medical specifications has been carried out taking into account medical/biological constraints and permissions. As result a list of specification parameters have been found which are listed below:

- a) 2-DoF (rotations about  $x$ -axis and  $y$ -axis),

- b) minimal scanning platform angle of  $\pm 12.5^\circ$ ,
- c) space assigned within a cube of  $10 \times 10 \times 10 \text{ mm}^3$ ,
- d) minimal bandwidth of 200 Hz,
- e) and scanning resolution better than  $100 \mu\text{m}$ .

Then, the state-of-the-art of topics related to different domains involved in the design and development of the microrobot was carried out. They included medical robotics, microdevices, microfabrication techniques, actuators compatible with microfabrication, parallel structures and laser technologies. Finally, our proposition based on the state-of-the-art and the specifications of the project was outlined.

After that, a proposition of two concepts to obtain microrobots with large amplitudes and high bandwidth was done. Thus, two kinematic structures were proposed. The microrobot Micro Agile-Eye which is based on a conventional kinematic structure that was scaled-down and the PiBot which is a new parallel kinematic mechanism. Their kinematic modeling was developed and screw theory was used for that.

The SCM fabrication process was selected. In fact, it is probably the first time it is used to fabricate microrobots with parallel structure. The materials used and the microfabrication procedures were presented for that. Fabrication outcome were shown for the two proposed microrobots. Then, by using interval analysis, the precision achieved with the structures were evaluated, for that the exponential representation of a homogeneous transformation using interval were used.

The last contribution of this thesis is the coupling of feedforward compensation of the nonlinearities and vibrations exhibited by the piezoelectric actuators with visual feedback of the parallel kinematic mechanisms. Two main control schemes were proposed: i) a control scheme for a parallel microrobot using visual servoing, ii) and a control scheme which combines classical visual servoing feedback with feedforward control of the nonlinearities and vibrations of the actuators. For that, a full characterization, modeling and compensation procedure of these phenomena was developed.

## 6.2 Perspectives

Indeed, this thesis opens a window for future studies on 3D parallel microrobotics. For that, this research has covered several areas. The improvement of these first versions are expected. For that, some areas must be treated in depth. They are:

- a) the mechanical optimization of the designed structures,
- b) the improvement of the fabrication techniques, in order to establish methods and design new tools to do repeatable processes,
- c) the obtention of the microrobot dynamic model, in order to develop a dynamic control,

- d) the control of the nonlinearities, to avoid the remaining of nonlinear behaviors that currently exist in the microrobot,
- e) the development of an optimal dimensioning of piezoelectric cantilevers actuators in order to calculate their optimal width and thickness.

On the other hand, as a robotic system these microrobots have the following perspectives:

- a) in short term- there is a need to strengthen the basis and their fixation in the base, as well as to perform better electrical connection that do not disturb the performances of the actuators,
- b) in medium term- the integration within the endoscope is a challenge that should be carried out after reinforcing the structure,
- c) in long term- clinical application in cadavers first and then in vivo tent are to be carried out.

From another point of view this microrobot is adaptable to other applications such as listed below:

- a) actuated micromirrors:
  - i) laser marking and etching,
  - ii) very fast laser steering,
  - iii) projector of images on a screen,
  - iv) vision by laser in robotics,
  - v) 3D scan.
- b) in telecommunications:
  - i) variable optical attenuators,
  - ii) optical switch: optical fiber to optical fiber.
- c) others medical applications:
  - i) all the other minimally invasive endoscopic surgery (using laser),
  - ii) biopsy based optical scanning (optical coherence tomography).

Finally, we foresee that the results in this thesis can be transferred to the market. To do so, the following stages are planned on the short term:

- a) develop a more robust prototype,
- b) file one or several patents and protect the software,
- c) contract out the market study,
- d) hopefully, create a company.



... and now, the real story will begin ...

## Piezoelectric beams

### A.1 Introduction

This appendix is based on [119, 13, 80, 143, 34] The proposed mechanical systems are based on a platform moved by actuators. The actuators are piezoelectric cantilever actuators. Piezoelectric cantilevers actuators have been chosen for this application because of their several advantages.

### A.2 Piezoelectric materials

Piezoelectric effect is also found in natural as well as artificial materials. The word piezoelectric is from the greek word *piezen* meaning pressure. The piezoelectricity is the foundation of the transduction process upon which all piezoelectric actuators and sensors are based.

Two characteristic effects of piezoelectricity are:

**Direct Piezoelectric Effect:** internal generation of electrical charge resulting from an applied mechanical force. This effect is mainly used for the development of sensor.

**Inverse Piezoelectric Effect:** internal generation of a mechanical strain resulting from an applied electrical field. This effect is mainly used for the development of actuators.

Among advantages of piezoelectric actuators are:

- sub-nanometer resolution,
- high bandwidth,
- large force generation,
- not affected by magnetic fields,
- extremely low steady state power consumption,

- low rate of wear,
- vacuum and clean room compatibility,

There are two forms to use piezoelectric materials as actuators: cantilever structures and stacks. Cantilever structures are advantageous because they yield larger displacements than stacks. Piezoelectric cantilevers are usually made of ceramic materials as PZT ( $Pb[Zr_xTi_{1-x}]O_3$ ) (Lead Zirconate Titanate). PZT materials are the most commercialized piezoelectric materials in the industry. However, PZT based actuators also have disadvantage as highly nonlinear input/output behavior. This disadvantage can be, nevertheless, alleviated with advanced with advanced modeling and control techniques [34].

### A.2.1 Modeling piezoelectric actuators

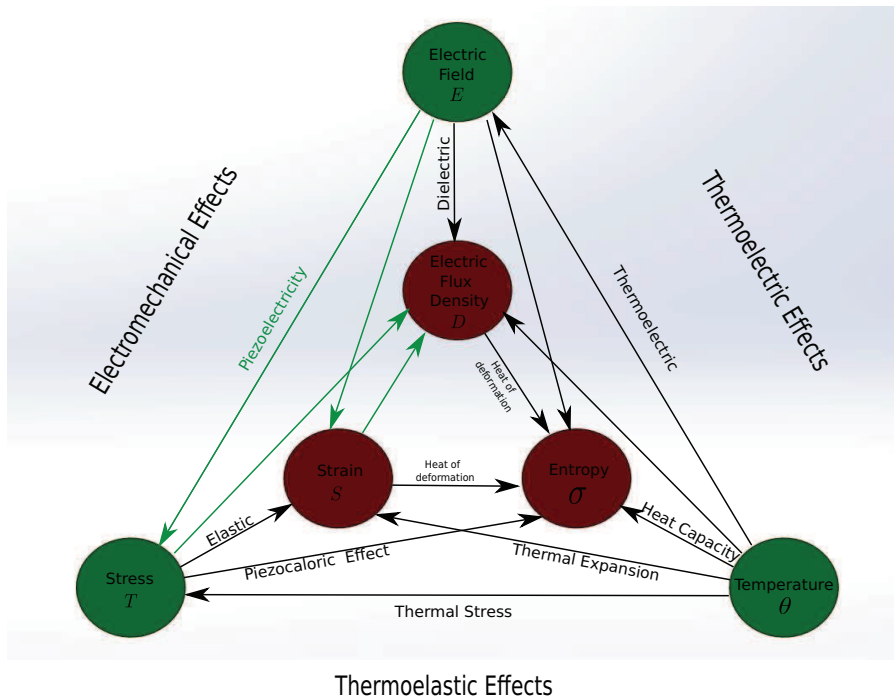


FIGURE A.1: Interaction processes between the electrical, mechanical and thermal systems [80].

Figure A.1 depicts the interaction between extensive variables (interior triangle) with intensive variables (exterior triangle). Though, in practice, thermo-mechanical and thermo-electric effects are almost disregarded in materials commonly employed like PZT ceramic. Hence, the variables involved in piezoelectricity are generally taken in an isothermal condition. Consequently the governing equations express the interaction between the electrical and the mechanical behavior of the material. This interaction has been approximated by static linear relations between two electrical and mechanical variables as is shown in equations (A.1) and (A.2) [119].

$$S = s^E T + dE \quad (\text{A.1})$$

$$D = dT + \epsilon^T E \quad (\text{A.2})$$

### A.2.2 Piezoelectric cantilever actuators

A piezoelectric cantilever actuator works in bending, based on the traverse piezoelectric effect and exploiting the bimetallic effect<sup>1</sup> to generate the deflection.

At least one of the layers that compose the piezoelectric cantilever actuator need to be active layer or piezoelectric material. Piezoelectric cantilever actuators can be classified according to the number of layers used and the number of piezoelectric layers. Usually the nomenclature to designate them consist in citing first the total number of layers followed by the word “-layer” and then the number of layers of active materials (piezoelectric) expressed as the corresponding latin prefix (uni, bi, tri, etc) followed by the word “-morph”.

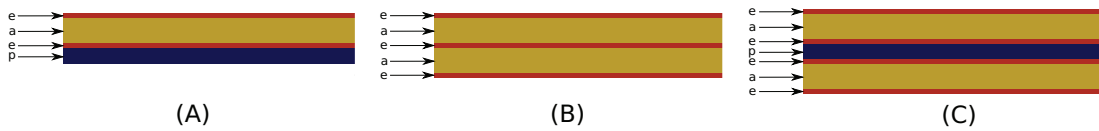


FIGURE A.2: Piezoelectric Structures: (A) two-layers unimorph, (B) two-layer bimorph, (C) three-layer bimorph.

Different structures of piezoelectric cantilever actuators are depicted in figure A.2. Active material is designed by 'a', passive material is designed by 'p', electrodes to excite the piezoelectric material are denominated by 'e'. Conductive adhesive layers can be considered as passive if their thickness is large.

A two-layer bimorph structure (see Figure A.2 (B)) has been chosen to use within the microrobot system as actuator. Bimorph structure shows that the actuator has two independently polarized piezoelectric layers (see Figure A.3 and Figure A.4). These piezoelectric layers must be driven in an opposite manner to generate a bend. The electric field can cause dilation or contractions on piezoelectric layers depending of the sens of the electric field and the polarization of the piezoelectric layer. Thus, the polarization of the active layers must be oriented to generate antagonist displacements in according with the sens of the electric field. Hence, a bend is generated while one active layer expands and the other active layer contracts.

Among the advantages of these kind of structure (see Figure A.2 (B)) with respect to unimorphs (see Figure A.2 (A)) is that the displacement deflection is increased and the blocking force is enhanced. In addition the structure is less sensitive to temperature disturbance.

There are two possibles two-layers bimorph structures. In the first case, the two piezoelectric layers have the same polarization direction, as shown in Figure A.3. This configuration is also called parallel bimorph. In the second case, depicted in Figure A.4, the two piezoelectric layers have opposite polarization directions. This configuration is called anti-parallel bimorph.

<sup>1</sup>Effect evidenced when different metals that expand differently are bonded one to one.

A structure two-layers bimorph have two possibilities of join the layers respecting the polarization orientations of the piezoelectric material. Two piezoelectric materials with the same polarization orientations is shown in figure A.3, this configuration is also called parallel bimorph. In figure A.4 also two piezoelectric materials with opposite polarization orientations is shown, this configuration is called serial bimorph.

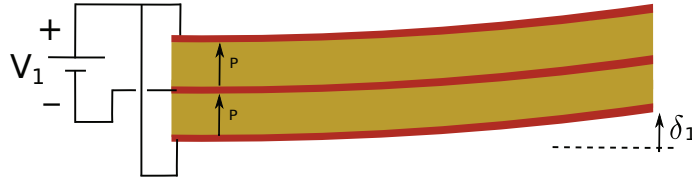


FIGURE A.3: A two-layers bimorph piezoelectric cantilever with parallel polarization.

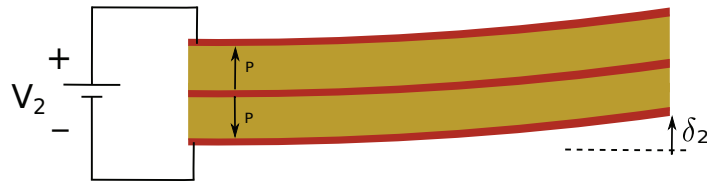


FIGURE A.4: A two-layers bimorph piezoelectric cantilever with anti-parallel polarization.

Each of the two above configurations has some advantages over the other. Voltages in anti-parallel configuration need to be twice the voltages in parallel configuration ( $V_2 = 2V_1$ ) to obtain the same displacement ( $\delta_1 = \delta_2$ ). We used therefore the parallel configuration.

The modeling of a piezoelectric bimorph cantilever in [13] and uses the following assumptions.

- The polarization is done only along the z-axis.
- The electric field is considered uniformly distributed along the z-axis.
- A perfect fixation or glue exists between the two piezoelectric layers.
- There is not exterior force applied.
- The width and thickness are negligible compared with the length.
- The beam Euler-Bernoulli assumptions are take into account.
- The transverse stress is negligible (thin).

### A.2.2.1 Static model

Let  $h_p$  and  $w$  be the thickness and width of each layer respectively. Applying the voltage  $U$ .

$$m_{piezo} = \frac{-wd_{31}h_p}{s_{11}^p} \quad (\text{A.3})$$

$$C = \frac{2wh_p^3}{3s_{11}^p} \quad (\text{A.4})$$

This leads to a deflection of the bi-morph cantilever described by the following equation (from [13]):

$$\delta_x = \frac{-m_{piezo}x^2}{2C}U \quad (\text{A.5})$$

$$\delta_x = \frac{-3d_{31}x^2}{4h_p^2}U \quad (\text{A.6})$$

where  $x \in [0, L]$ ,  $d_{31}$  is the transverse piezoelectric coefficient [119].

### A.2.2.2 Dynamic properties

The  $m^{th}$  resonant frequencies:

$$f_m = \frac{(k_m L)^2 h_p}{2\pi L^2} \sqrt{\frac{1}{3\rho s_{11}^p}} \quad (\text{A.7})$$

with  $k_m L$  is defined in the table A.1 for each mode.

mode	1	2	3	...	
$k_m L$	1.8751	4.6941	7.8548	...	

TABLE A.1: Solution for the characteristic equation of A.7









# Bibliography

- [1] Texas instruments.
- [2] 3DFACTORY. <http://3dfactory.co.il/>.
- [3] AGNUS, J., CHAILLET, N., CLÉVY, C., DEMBÉLÉ, S., GAUTHIER, M., HADDAB, Y., LAURENT, G., LUTZ, P., PIAT, N., RABENOROSOA, K., ET AL. Robotic microassembly and micromanipulation at femto-st. *Journal of Micro-Bio Robotics* 8, 2 (2013), 91–106.
- [4] ALEXIOU, C., SCHMID, R., JURGONS, R., BERGEMANN, C., ARNOLD, W., AND PARAK, F. Targeted tumor therapy with magnetic drug targeting: Therapeutic efficacy of ferrofluid bound mitoxantrone. In *Ferrofluids*, S. Odenbach, Ed., vol. 594 of *Lecture Notes in Physics*. Springer Berlin / Heidelberg, 2003, pp. 233–251.
- [5] ALI, M. Y., AND MOHAMMAD, A. S. Experimental study of conventional wire electrical discharge machining for microfabrication. *Materials and Manufacturing Processes* 23, 7 (2008), 641–645.
- [6] ANDREFF, N. Des droites et des robots. *Modélisation, identification et commande référencées vision des machines complexes. Habilitation à diriger des recherches, Université Blaise Pascal* (2006).
- [7] ANDREFF, N., TAMADAZTE, B., DEMBÉLÉ, S., AND HUSSNAIN, Z. E. Preliminary variation on multiview geometry for vision-guided laser surgery. In *Workshop on Multi-View Geometry in Robotics, MVIGRO'2013*. (2013), pp. 1–10.
- [8] ANGELES, J. *Spatial Kinematic Chains. Analysis, Synthesis, and Optimisation*. Springer-Verlag, Berlin, 1982.
- [9] ARDELEAN, E. V., COLE, D. G., AND CLARK, R. L. High performance v-stackpiezoelectric actuator. *Journal of intelligent material systems and structures* 15, 11 (2004), 879–889.
- [10] ARYA, S. P., AND PAN, T.-S. Piezoelectric microactuator for slider side actuation, may 2004. US Patent 6,738,231.

- [11] BACH, T., NETSCH, C., HAECKER, A., MICHEL, M.-S., HERRMANN, T. R., AND GROSS, A. J. Thulium: Yag laser enucleation (vapoenucleation) of the prostate: safety and durability during intermediate-term follow-up. *World journal of urology* 28, 1 (2010), 39–43.
- [12] BAFFOUN, B., LERCH, R., SUTOR, A., AND WEISTENHÖFER, C. Magnetostrictive microloudspeaker, Mar. 25 2014. US Patent 8,682,009.
- [13] BALLAS, R. *Piezoelectric Multilayer Beam Bending Actuators: Static and Dynamic Behavior and Aspects of Sensor Integration*. Microtechnology and Mems. Springer, 2007.
- [14] BARNES, S. M., BURG, M. S., JENSEN, B. D., MILLER, S. L., AND RODGERS, M. S. Compact electrostatic comb actuator, oct 2000. US Patent 6,133,670.
- [15] BELLAKEHAL, S., ANDREFF, N., MEZOUAR, Y., AND TADJINE, M. Force/position control of parallel robots using exteroceptive pose measurements. *Meccanica* 46 (2011), 195–205.
- [16] BELLAKEHAL, S., ANDREFF, N., MEZOUAR, Y., AND TADJINE, M. Vision/force control of parallel robots. *Mechanism and Machine Theory* 46 (2011), 1376–1395.
- [17] BEN-YAKAR, A., HOY, C., EVERETT, W. N., AND KOBLER, J. Toward endoscopic ultrafast laser microsurgery of vocal folds. *Head & Neck Oncology* 2 (2010).
- [18] BENARD, W. L., KAHN, H., HEUER, A. H., AND HUFF, M. A. Thin-film shape-memory alloy actuated micropumps. *Microelectromechanical Systems, Journal of* 7, 2 (1998), 245–251.
- [19] BERMAN, B. 3-d printing: The new industrial revolution. *Business horizons* 55, 2 (2012), 155–162.
- [20] BERNSTEIN, J., TAYLOR, W. P., BRAZZLE, J., KIRKOS, G., ODHNER, J., PAREEK, A., AND ZAI, M. Two axis-of-rotation mirror array using electromagnetic MEMS. In *IEEE International Conference on Micro Electro Mechanical Systems* (2003), pp. 275–278.
- [21] BHUYAN, M., COURVOISIER, F., PHING, H., JEDRKIEWICZ, O., RECCHIA, S., DI TRAPANI, P., AND DUDLEY, J. Laser micro-and nanostructuring using femtosecond bessel beams. *The European Physical Journal-Special Topics* 199, 1 (2011), 101–110.
- [22] BLANCO, R. G. F., HA, P. K., CALIFANO, J. A., AND SAUNDERS, J. M. Transoral robotic surgery of the vocal cord. *Journal of Laparoendoscopic & Advanced Surgical Techniques* 21, 2 (2011), 157–159.
- [23] BLOCK, B., JOHNSON, A. D., AND MAUGER, P. Shape memory alloy microactuator having an electrostatic force and heating means, april 1997. US Patent 5,619,177.
- [24] BONEV, I. A. *Geometric analysis of parallel mechanisms*. PhD thesis, Université Laval, 2003.

- [25] BÜTTGENBACH, S. Electromagnetic micromotors design, fabrication and applications. *Micromachines* 5, 4 (2014), 929–942.
- [26] CHANEY, H. K. Electric fluid valve, dec 1968. US Patent 3,416,549.
- [27] CHANEY, H. K., AND STRANDRUD, H. T. Electric fluid actuator, aug 1971. US Patent 3,599,428.
- [28] CHARLES, S. The preparation of magnetic fluids. In *Ferrofluids*, S. Odenbach, Ed., vol. 594 of *Lecture Notes in Physics*. Springer Berlin - Heidelberg, 2003, pp. 3–18.
- [29] CHAUMETTE, F., AND HUTCHINSON, S. Visual servo control. i. basic approaches. *Robotics & Automation Magazine, IEEE* 13, 4 (2006), 82–90.
- [30] CHO, I.-J., YUN, K.-S., KEW LEE, H., YOON, J.-B., AND YOON, E. A low-voltage two-axis electromagnetically actuated micromirror with bulk silicon mirror plates and torsion bars. In *IEEE International Conference on Micro Electro Mechanical Systems* (2002), pp. 540–543.
- [31] CHU, B. *Laser Light Scattering 2e: Basic Principles and Practice*. Elsevier Science, 2012.
- [32] CIOFANI, G., AND MENCIASSI, A. *Piezoelectric Nanomaterials for Biomedical Applications*. Nanomedicine and Nanotoxicology. Springer, 2012.
- [33] CLARK, S. L., AND HAMMOND, P. T. Engineering the microfabrication of layer-by-layer thin films. *Advanced Materials* 10, 18 (1998), 1515–1519.
- [34] CLÉVY, C., RAKOTONDRABE, M., AND CHAILLET, N. *Signal Measurement and Estimation Techniques for Micro and Nanotechnology*. Springer, 2011.
- [35] CONANT, R. A., NEE, J. T., LAU, K. Y., AND MULLER, R. S. A flat high-frequency scanning micromirror. In *Proc. Solid-State Sensor and Actuator Workshop* (2000), pp. 6–9.
- [36] CORKE, P. I. Visual control of robot manipulators—a review. *Visual servoing* 7 (1993), 1–31.
- [37] COURVOISIER, F., ZHANG, J., BHUYAN, M., JACQUOT, M., AND DUDLEY, J. M. Applications of femtosecond bessel beams to laser ablation. *Applied Physics A* 112, 1 (2013), 29–34.
- [38] DAHMOUCHE, R., ANDREFF, N., MEZOUAR, Y., AIT-AIDER, O., AND MARTINET, P. Dynamic visual servoing from sequential regions of interest acquisition. *International Journal of Robotic Research* 31 (2012), 520–537.
- [39] DANIELE, C. D. V. R. B., RICCARDIA, G. A., AND SPAIRANID, R. Actuating the deformable mirror: a multiphysics design approach. In *Proc. of SPIE Vol.*, vol. 7018, pp. 70181E–1.

- [40] DARIO, P., GUGLIELMELLI, E., ALLOTTA, B., AND CARROZZA, M. C. Robotics for medical applications. *Robotics & Automation Magazine, IEEE* 3, 3 (1996), 44–56.
- [41] DARIO, P., HANNAFORD, B., AND MENCIASSI, A. Smart surgical tools and augmenting devices. *Robotics and Automation, IEEE Transactions on* 19, 5 (2003), 782–792.
- [42] DOMBRE, E. Surgical robotics - summer school.
- [43] DUBOIS, M.-A., MURALT, P., TAYLOR, D. V., AND HIBOUX, S. Which pzt thin films for piezoelectric microactuator applications? *Integrated Ferroelectrics* 22, 1-4 (1998), 535–543.
- [44] EDMUNDOPTICS. <http://www.edmundoptics.com>.
- [45] EHRLICH, D. J., AND TSAO, J. Y. *Laser microfabrication: thin film processes and lithography*. Elsevier, 1989.
- [46] ESPIAU, B. Effect of camera calibration errors on visual servoing in robotics. In *Experimental Robotics III*. Springer, 1994, pp. 182–192.
- [47] ESPIAU, B., CHAUMETTE, F., AND RIVES, P. A new approach to visual servoing in robotics. *Robotics and Automation, IEEE Transactions on* 8, 3 (1992), 313–326.
- [48] FATIKOW, S., AND REMBOLD, U. *Microsystem Technology and Microrobotics*, 1st ed. Springer-Verlag New York, Inc., Secaucus, NJ, USA, 1997.
- [49] FERHANOGLU, O., YILDIRIM, M., SUBRAMANIAN, K., AND BEN-YAKAR, A. A 5-mm piezo-scanning fiber device for high speed ultrafast laser microsurgery. *Biomedical optics express* 5, 7 (2014), 2023–2036.
- [50] FORUM, M. D. <http://www.mechanicaldesignforum.com/>.
- [51] FOWLER, A., LASKOVSKI, A., HAMMOND, A., AND MOHEIMANI, S. A 2-dof electrostatically actuated mems nanopositioner for on-chip afm. *Microelectromechanical Systems, Journal of* 21, 4 (aug. 2012), 771–773.
- [52] FUKUTA, Y., CHAPUIS, Y.-A., MITA, Y., AND FUJITA, H. Design, fabrication, and control of mems-based actuator arrays for air-flow distributed micromanipulation. *Microelectromechanical Systems, Journal of* 15, 4 (2006), 912–926.
- [53] GARWIN, L., AND LINCOLN, T. *A century of Nature: twenty-one discoveries that changed science and the world*. University of Chicago Press, 2010.
- [54] GAUTHIER, J.-Y., HUBERT, A., ABADIE, J., CHAILLET, N., AND LEXCELLENT, C. Nonlinear hamiltonian modelling of magnetic shape memory alloy based actuators. *Sensors and Actuators A: Physical* 141, 2 (2008), 536–547.
- [55] GAUTHIER, J.-Y., HUBERT, A., ABADIE, J., CHAILLET, N., LEXCELLENT, C., ET AL. Magnetic shape memory alloy and actuator design. In *Proceedings of the 5th International Workshop on Microfactories, IWMMF'06*. (2006).

- [56] GAUTHIER, J.-Y., HUBERT, A., ABADIE, J., LEXCELLENT, C., CHAILLET, N., ET AL. Multistable actuator based on magnetic shape memory alloy.. *ACTUATOR'2006. 1* (2006), 787–790.
- [57] GIALLO, J. F. *A medical robotic system for laser phonomicrosurgery*. ProQuest, 2008.
- [58] GILBERTSON, R. G., AND BUSCH, J. D. A survey of micro-actuator technologies for future spacecraft missions.
- [59] GIURGIUTIU, V. Mechatronics aspects of smart materials induced strain actuation. In *7th Mechatronics Forum International Conference* (2000), pp. 6–8.
- [60] GLASSNER, A. *An Introduction to Ray Tracing*. Academic Press. Academic Press, 1989.
- [61] GOLDSZTEJN, A. On the exponentiation of interval matrices. *CoRR abs/0908.3954* (2009).
- [62] GOSSELIN, C., AND ANGELES, J. Singularity analysis of closed-loop kinematic chains. *Robotics and Automation, IEEE Transactions on* 6, 3 (jun 1990), 281 –290.
- [63] GOSSELIN, C., AND CARON, F. Two degree-of-freedom spherical orienting device, Oct. 19 1999. US Patent 5,966,991.
- [64] GROUP, H. R. <https://sites.google.com/site/hendersonresearchgroup/>.
- [65] GRUNWALD, A., AND OLABI, A. Design of a magnetostrictive (ms) actuator. *Sensors and Actuators A: Physical* 144, 1 (2008), 161 – 175.
- [66] GUO, S. X., AND BEN-YAKAR, A. Femtosecond laser nanoablation of glass in the near-field of single wall carbon nanotube bundles. *Journal of Physics D-applied Physics* 41 (2008).
- [67] HA, J.-L., FUNG, R.-F., AND HAN, C.-F. Optimization of an impact drive mechanism based on real-coded genetic algorithm. *Sensors and Actuators A: Physical* 121, 2 (2005), 488–493.
- [68] HABINEZA, D., RAKOTONDRABE, M., AND LE GORREC, Y. Multivariable generalized bouc-wen modeling, identification and feedforward control and its application to multi-dof piezoelectric actuators. In *World Congress* (2014), vol. 19, pp. 10952–10958.
- [69] HARTLEY, R., AND ZISSERMAN, A. *Multiple View Geometry in Computer Vision*. Cambridge books online. Cambridge University Press, 2003.
- [70] HASHIMOTO, K. *Visual servoing: real-time control of robot manipulators based on visual sensory feedback*, vol. 7. World scientific, 1993.
- [71] HIRANO, M. Phonosurgery: basic and clinical investigations. *Otologia (Fukuoka)* 21, suppl 1 (1975), 239–260.

- [72] HOOVER, A. M., AND FEARING, R. S. Fast scale prototyping for folded millirobots. In *International Conference on Robotics and Automation* (2008), pp. 1777–1778.
- [73] HOSODA, K., AND ASADA, M. Versatile visual servoing without knowledge of true jacobian. In *Intelligent Robots and Systems '94. Advanced Robotic Systems and the Real World', IROS'94. Proceedings of the IEEE/RSJ/GI International Conference on* (1994), vol. 1, IEEE, pp. 186–193.
- [74] HOUSEHOLDER, A., AND OF AMERICA, M. A. *Lectures on numerical algebra*. Mathematical Association of America, 1972.
- [75] HUNG, J. Y. Posicast control past and present. *IEEE Multidisciplinary engineering education magazine* 2, 1 (2007), 7–11.
- [76] HUNT, K. *Kinematic geometry of mechanisms*. Oxford engineering science series. Clarendon Press, 1978.
- [77] HUO, D., AND CHENG, K. Overview of micro cutting. *Micro-Cutting: Fundamentals and Applications* (2013), 1–17.
- [78] HÜTTENBRINK, K., AND AMBROSCH, P. *Lasers in Otorhinolaryngology*. Current topics in otolaryngology, head and neck surgery. New York, 2005.
- [79] IIVIINFRARED. <http://www.iiviinfrared.com>.
- [80] IKEDA, T. *Fundamentals of Piezoelectricity*. Oxford Science Publications. Clarendon Press, 1990.
- [81] IMAI, S., AND TSUKIOKA, T. A magnetic mems actuator using a permanent magnet and magnetic fluid enclosed in a cavity sandwiched by polymer diaphragms. *Precision Engineering* 38, 3 (2014), 548–554.
- [82] ISMAIL, M., IKHOUANE, F., AND RODELLAR, J. The hysteresis bouc-wen model, a survey. *Archives of Computational Methods in Engineering* 16, 2 (2009), 161–188.
- [83] JACKMAN, R. J., DUFFY, D. C., CHERNIAVSKAYA, O., AND WHITESIDES, G. M. Using elastomeric membranes as dry resists and for dry lift-off. *Langmuir* 15, 8 (1999), 2973–2984.
- [84] JAECKLIN, V., LINDER, C., DE ROOIJ, N., MORET, J., BISCHOF, R., AND RUDOLF, F. Novel polysilicon comb actuators for xy-stages. In *Micro Electro Mechanical Systems, 1992, MEMS'92, Proceedings. An Investigation of Micro Structures, Sensors, Actuators, Machines and Robot. IEEE* (1992), IEEE, pp. 147–149.
- [85] JAGERSAND, M., FUENTES, O., AND NELSON, R. Experimental evaluation of uncalibrated visual servoing for precision manipulation. In *Robotics and Automation, 1997. Proceedings., 1997 IEEE International Conference on* (1997), vol. 4, IEEE, pp. 2874–2880.

- [86] JAIN, A., KOPA, A., PAN, Y., FEDDER, G. K., AND XIE, H. A two-axis electrothermal micromirror for endoscopic optical coherence tomography. *IEEE Journal of Selected Topics in Quantum Electronics* 10 (2004), 636–642.
- [87] JAIN, A., QU, H., TODD, S., AND XIE, H. A thermal bimorph micromirror with large bi-directional and vertical actuation. *Sensors and Actuators A: Physical* 122, 1 (2005), 9 – 15. Special Section of the Micromechanics Section of Sensors and Actuators based on contributions revised from the Technical Digest of the 2004 Solid-State Sensor, Actuator and Microsystems Workshop.
- [88] JAIN, A., AND XIE, H. A single-crystal silicon micromirror for large bi-directional 2D scanning applications. *Sensors and Actuators A-physical* 130 (2006), 454–460.
- [89] JAIN, V., SIDPARA, A., BALASUBRAMANIAM, R., LODHA, G., DHAMGAYE, V., AND SHUKLA, R. Micromanufacturing: A reviewpart i. *Proceedings of the Institution of Mechanical Engineers, Part B: Journal of Engineering Manufacture* 228, 9 (2014), 973–994.
- [90] JAKO, D., AND STRONG, S. Laser surgery of vocal cords - experimental study with carbon-dioxide lasers on dogs. *Laryngoscope* 82 (1972), 2204–2216.
- [91] JAKO, D., AND STRONG, S. Use of co2-laser in microsurgery of larynx. *HNO* 22 (1974), 122.
- [92] JALILI, N. *Piezoelectric-Based Vibration Control: From Macro to Micro/Nano Scale Systems*. Springer, 2009.
- [93] JAULIN, L., AND WALTER, E. Set inversion via interval analysis for nonlinear bounded error estimation. *Automatica* 29, 4 (1993), 1053–1064.
- [94] KELLER, J. B. Rays, waves and asymptotics. *Bulletin of the American mathematical society* 84, 5 (1978), 727–750.
- [95] KOHL, M., DITTMANN, D., QUANDT, E., AND WINZEK, B. Thin film shape memory microvalves with adjustable operation temperature. *Sensors and Actuators A: Physical* 83, 1 (2000), 214–219.
- [96] KONG, X., AND GOSSELIN, C. *Type synthesis of parallel mechanisms*, vol. 33. Springer Heidelberg, 2007.
- [97] KONG XIANWEN. Forward Displacement Analysis and Singularity Analysis of a Special 2-DOF 5R Spherical Parallel Manipulator. *Journal of Mechanisms and Robotics* 3, 2 (mar 2011), 024501–024501. 10.1115/1.4003445.
- [98] KRULEVITCH, P., LEE, A. P., RAMSEY, P. B., TREVINO, J. C., HAMILTON, J., AND NORTHRUP, M. A. Thin film shape memory alloy microactuators. *Microelectromechanical Systems, Journal of* 5, 4 (1996), 270–282.



- [99] KUROZUKA, A., AND OBI, H. Actuator with symmetric positioning, jan 2011. US Patent 7,872,395.
- [100] KWON, S., MILANOVIC, V., AND LEE, L. P. A high aspect ratio 2D gimbaled microscanner with large static rotation. In *IEEE/LEOS International Conference on Optical* (2002).
- [101] KYRKI, V., KRAGIC, D., AND CHRISTENSEN, H. I. Measurement errors in visual servoing. *Robotics and Autonomous Systems* 54, 10 (2006), 815–827.
- [102] LASERCOMPONENTS. [www.lasercomponents.com](http://www.lasercomponents.com).
- [103] LEE, R. E. Microfabrication by ion-beam etching. *Journal of Vacuum Science and Technology* 16, 2 (1979), 164–170.
- [104] LI, S., AND CHEN, S. Analytical analysis of a circular pzt actuator for valveless micropumps. *Sensors and Actuators A: Physical* 104, 2 (2003), 151–161.
- [105] LIU, Y., LI, W., YANG, C., AND SONG, R. Design and test of small-scale rotary engine power system. In *2007 First International Conference on Integration and Commercialization of Micro and Nanosystems* (2007), American Society of Mechanical Engineers, pp. 47–51.
- [106] LOBONTIU, N. *Compliant Mechanisms: Design of Flexure Hinges*. Mechanical engineering. CRC Press, 2003.
- [107] LUMENIS. <http://www.lumenis.com/>.
- [108] MACK, C. *Fundamental principles of optical lithography: the science of microfabrication*. John Wiley & Sons, 2008.
- [109] MAEDA, S., ABE, K., YAMAMOTO, K., TOHYAMA, O., AND ITO, H. Active endoscope with sma (shape memory alloy) coil springs. In *Micro Electro Mechanical Systems, 1996, MEMS'96, Proceedings. An Investigation of Micro Structures, Sensors, Actuators, Machines and Systems. IEEE, The Ninth Annual International Workshop on* (1996), IEEE, pp. 290–295.
- [110] MALIS, E. Hybrid vision-based robot control robust to large calibration errors on both intrinsic and extrinsic camera parameters. In *European Control Conference* (2001), Cite-seer, pp. 2898–2903.
- [111] MARKOW, M., YANG, Y., WELCH, A., RYLANDER, H.G., I., AND WEINBERG, W. An automated laser system for eye surgery. *Engineering in Medicine and Biology Magazine, IEEE* 8, 4 (Dec 1989), 24–29.
- [112] MARTINEZ, F. C., KNOBLOCH, A. J., AND PISANO, A. P. Apex seal design for the mems rotary engine power system. In *ASME 2003 International Mechanical Engineering Congress and Exposition* (2003), American Society of Mechanical Engineers, pp. 157–162.

- [113] MASON, W. P. Piezoelectricity, its history and applications. *The Journal of the Acoustical Society of America* 70, 6 (1981), 1561–1566.
- [114] MASSIEU, J.-L. Frame grabbing with laser scanner with sweeping by silicon planar electrostatics actuator, 2002.
- [115] MATHIS, A., COURVOISIER, F., FROEHLI, L., FURFARO, L., JACQUOT, M., LA-COURT, P.-A., AND DUDLEY, J. M. Micromachining along a curve: Femtosecond laser micromachining of curved profiles in diamond and silicon using accelerating beams. *Applied Physics Letters* 101, 7 (2012), 071110.
- [116] MAYERGOYZ, I. D. *Mathematical models of hysteresis and their applications*. Academic Press, 2003.
- [117] MAZIZ, A., PLESSE, C., SOYER, C., CHEVROT, C., TEYSSIÉ, D., CATTAN, E., AND VIDAL, F. Demonstrating khz frequency actuation for conducting polymer microactuators. *Advanced Functional Materials* 24, 30 (2014), 4851–4859.
- [118] MEGNIN, C., AND KOHL, M. Shape memory alloy microvalves for a fluidic control system. *Journal of Micromechanics and Microengineering* 24, 2 (2014), 025001.
- [119] MEITZLER, A., TIERSTEN, H., WARNER, A., BERLINCOURT, D., COUQUIN, G., AND WELSH III, F. Ieee standard on piezoelectricity, 1988.
- [120] MERLET, J. *Parallel Robots*. Solid Mechanics and Its Applications. Springer, 2006.
- [121] MOHAMED, M. G., AND DUFFY, J. A Direct Determination of the Instantaneous Kinematics of Fully Parallel Robot Manipulators. *Journal of Mechanisms Transmissions and Automation in Design* 107 (1985).
- [122] MOORE, R. E. Interval analysis. *Prentice-Hall, NJ* (1966).
- [123] NAUMENKO, K., AND ALTENBACH, H. *Modeling of creep for structural analysis*. Springer Science & Business Media, 2007.
- [124] NEZHAT, C. *Operative Gynecologic Laparoscopy: Principles and Techniques*. McGraw-Hill, Incorporated, Health Professions Division, 1995.
- [125] NGUYEN, T. D., DESHMUKH, N., NAGARAH, J. M., KRAMER, T., PUROHIT, P. K., BERRY, M. J., AND MCALPINE, M. C. Piezoelectric nanoribbons for monitoring cellular deformations. *Nature nanotechnology* 7, 9 (2012), 587–593.
- [126] OLABI, A., AND GRUNWALD, A. Design and application of magnetostrictive materials. *Materials & Design* 29, 2 (2008), 469 – 483.
- [127] ONAL, C. D., WOOD, R. J., AND RUS, D. An origami-inspired approach to worm robots. *Mechatronics, IEEE/ASME Transactions on* 18, 2 (April 2013), 430–438.
- [128] OPHIROPT. <http://www.ophiropt.com/>.

- [129] OPSOMMER, E., WEISS, T., MILTNER, W., AND PLAGHKI, L. Scalp topography of ultralate (c-fibres) evoked potentials following thulium yag laser stimuli to tiny skin surface areas in humans. *Clinical neurophysiology* 112, 10 (2001), 1868–1874.
- [130] OTA, T., DEGANI, A., SCHWARTZMAN, D., ZUBIATE, B., MCGARVEY, J., CHOSSET, H., AND ZENATI, M. A. A highly articulated robotic surgical system for minimally invasive surgery. *The Annals of thoracic surgery* 87, 4 (2009), 1253–1256.
- [131] OZGUR, E., BOUTON, N., ANDREFF, N., AND MARTINET, P. Dynamic control of the Quattro robot by the leg edges. In *International Conference on Robotics and Automation* (2011), pp. 2731–2736.
- [132] PAC, M., AND POPA, D. Interval analysis for robot precision evaluation. In *IEEE International Conference on Robotics and Automation (ICRA) 2012* (2012), IEEE, pp. 1087–1092.
- [133] PATEL, S., RAJADHYAKSHA, M., KIROV, S., LI, Y., AND TOLEDO-CROW, R. Endoscopic laser scalpel for head and neck cancer surgery. In *SPIE BiOS* (2012), International Society for Optics and Photonics, pp. 82071S–82071S.
- [134] PENG, J., AND CHEN, X. Modeling of piezoelectric-driven stick–slip actuators. *Mechanics, IEEE/ASME Transactions on* 16, 2 (2011), 394–399.
- [135] PHENIXSYSTEMS. <http://www.phenix-systems.com/>.
- [136] PIMICOS. <http://www.pimicos.com/>.
- [137] PIYAWATTANAMETHA, W., PATTERSON, P. R., HAH, D., TOSHIYOSHI, H., AND WU, M. C. A 2D Scanner by Surface and Bulk Micromachined Angular Vertical Comb Actuators.
- [138] PONS, J. *Emerging Actuator Technologies: A Micromechatronic Approach*. John Wiley & Sons, 2005.
- [139] POWELL, J. *CO2 laser cutting*, vol. 214. Cambridge Univ Press, 1993.
- [140] RAHMAN, M. A., RAHMAN, M., KUMAR, A. S., AND LIM, H. Cnc microturning: an application to miniaturization. *International Journal of Machine Tools and Manufacture* 45, 6 (2005), 631–639.
- [141] RAKOTONDRABE, M. *Développement et Commande Modulaire d’une Station de Microassemblage*. PhD thesis, Thesis presenteds to Franche-Comté University, 2006.
- [142] RAKOTONDRABE, M. Bouc-wen modeling and inverse multiplicative structure to compensate hysteresis nonlinearity in piezoelectric actuators. *IEEE Transactions on Automation Science and Engineering* 8, 2 (2011), 428–431.
- [143] RAKOTONDRABE, M. *Piezoelectric Cantilevered Structures: Modeling, Control and Estimation Aspects*. Microtechnology and MemS. Springer-Verlag GmbH, 2012.

- [144] RAKOTONDRABE, M., CLÉVY, C., AND LUTZ, P. Hysteresis and vibration compensation in a nonlinear unimorph piezocantilever. In *Intelligent Robots and Systems, 2008. IROS 2008. IEEE/RSJ International Conference on* (2008), IEEE, pp. 558–563.
- [145] RAKOTONDRABE, M., CLÉVY, C., AND LUTZ, P. Complete open loop control of hysteretic, creeped, and oscillating piezoelectric cantilevers. *Automation Science and Engineering, IEEE Transactions on* 7, 3 (2010), 440–450.
- [146] RAKOTONDRABE, M., FOWLER, A. G., AND MOHEIMANI, S. O. R. Characterization of a 2-dof mems nanopositioner with integrated electrothermal actuation and sensing. In *Sensors, 2012 IEEE* (oct. 2012), pp. 1–4.
- [147] RAKOTONDRABE, M., AND IVAN, I. A. Development and dynamic modeling of a new hybrid thermopiezoelectric microactuator. *Robotics, IEEE Transactions on* 26, 6 (2010), 1077–1085.
- [148] RENAUD, P. *Apport de la vision pour l'identification géométrique de mécanismes parallèles*. PhD thesis, 2003.
- [149] RIVERA-SERRANO, C. M., JOHNSON, P., ZUBIATE, B., KUENZLER, R., CHOSET, H., ZENATI, M., TULLY, S., AND DUVVURI, U. A transoral highly flexible robot. *The Laryngoscope* 122, 5 (2012), 1067–1071.
- [150] ROCH, I., BIDAUD, P., COLLARD, D., AND BUCHAILLOT, L. Fabrication and characterization of an su-8 gripper actuated by a shape memory alloy thin film. *Journal of Micromechanics and Microengineering* 13, 2 (2003), 330.
- [151] ROCKYMOUNTAINGROUP. <http://rockymountainentgroup.com/>.
- [152] RONALDO, R., PAPASTATHIS, T., YANG, H., TIETJE, C., TURITTO, M., AND RATCHEV, S. In situ microassembly. In *Micro-Assembly Technologies and Applications*. Springer, 2008, pp. 177–185.
- [153] ROSA, B., HERMAN, B., SZEWCZYK, J., GAYET, B., AND MOREL, G. Laparoscopic optical biopsies: In vivo robotized mosaicing with probe-based confocal endomicroscopy. In *IEEE/RSJ International Conference on Intelligent Robots and Systems (IROS)* (2011), pp. 1339–1345.
- [154] ROSENBLUH, M., ANTONOV, I., IANETZ, D., KAGANOVSKII, Y., AND LIPOVSKII, A. Microfabrication of structures by laser light in metal-doped glasses. *Optical Materials* 24, 1 (2003), 401–410.
- [155] RUMP, S. Intlab interval laboratory. In *Developments in Reliable Computing*, T. Csendes, Ed. Springer Netherlands, 1999, pp. 77–104.
- [156] RZAEV, Z. M., DINCER, S., AND PIŞKIN, E. Functional copolymers of n-isopropylacrylamide for bioengineering applications. *Progress in Polymer Science* 32, 5 (2007), 534–595.

- [157] SAHAI, R., STELTZ, E., AND FEARING, R. S. Carbon fiber components with integrated wiring for millirobot prototyping. In *International Conference on Robotics and Automation* (2005), pp. 1258–1263.
- [158] SCHENK, H., DURR, P., KUNZE, D., LAKNER, H., AND KUCK, H. An electrostatically excited 2D-micro-scanning-mirror with an in-plane configuration of the driving electrodes. In *IEEE International Conference on Micro Electro Mechanical Systems* (2000), pp. 473–478.
- [159] SCHLOTT, K., KOINZER, S., PTASZYNSKI, L., BEVER, M., BAADE, A., ROIDER, J., BIRNGRUBER, R., AND BRINKMANN, R. Automatic temperature controlled retinal photocoagulation. *Journal of biomedical optics* 17, 6 (2012), 0612231–0612238.
- [160] SCHNEIDER, O., AND TROCCAZ, J. A six-degree-of-freedom passive arm with dynamic constraints (padyc) for cardiac surgery application: Preliminary experiments. *Computer aided surgery* 6, 6 (2001), 340–351.
- [161] SELIG, J. *Geometric Fundamentals of Robotics*. Monographs in Computer Science. Springer, 2010.
- [162] SERES, J., SERES, E., VERHOEF, A. J., TEMPEA, G., STRELI, C., WOBRAUSCHEK, P., YAKOVLEV, V., SCRINZI, A., SPIELMANN, C., AND KRAUSZ, F. Laser technology: Source of coherent kiloelectronvolt x-rays. *Nature* 433, 7026 (2005), 596–596.
- [163] SIAUVE, N., SCORRETTI, R., BURAI, N., NICOLAS, L., AND NICOLAS, A. Electromagnetic fields and human body: a new challenge for the electromagnetic field computation. *Compel-the International Journal for Computation and Mathematics in Electrical and Electronic Engineering* 22 (2003), 457–469.
- [164] SINGER, N. C., SEERING, W. P., AND PASCH, K. A. Shaping command inputs to minimize unwanted dynamics, apr. 10 1990.
- [165] SINGH, T., AND SINGHOSE, W. Input shaping/time delay control of maneuvering flexible structures. In *American Control Conference, 2002. Proceedings of the 2002* (2002), vol. 3, IEEE, pp. 1717–1731.
- [166] SMITH, O. J. Posicast control of damped oscillatory systems. *Proceedings of the IRE* 45, 9 (1957), 1249–1255.
- [167] SOLARES, C. A., AND STROME, M. Transoral robot-assisted co2 laser supraglottic laryngectomy: Experimental and clinical data. *The Laryngoscope* 117, 5 (2007), 817–820.
- [168] SONG, J., AND DER KIUREGHIAN, A. Generalized bouc–wen model for highly asymmetric hysteresis. *Journal of engineering mechanics* 132, 6 (2006), 610–618.
- [169] SREETHARAN, P. S., WHITNEY, J. P., STRAUSS, M. D., AND WOOD, R. J. Monolithic fabrication of millimeter-scale machines. *Journal of Micromechanics and Microengineering* 22, 5 (2012), 055027.

- [170] SU, G.-D. J., TOSHIYOSHI, H., AND WU, M. C. Surface-micromachined 2-D optical scanners with high-performance single-crystalline silicon micromirrors. *IEEE Photonics Technology Letters* 13 (2001), 606–608.
- [171] SUERGERYENCYCLOPEDIA. <http://www.surgeryencyclopedia.com/La-Pa/Microsurgery.html>.
- [172] TALAMO, J. H., GOODING, P., ANGELEY, D., CULBERTSON, W. W., SCHUELE, G., ANDERSEN, D., MARCELLINO, G., ESSOCK-BURNS, E., BATLLE, J., FELIZ, R., ET AL. Optical patient interface in femtosecond laser-assisted cataract surgery: contact corneal applanation versus liquid immersion. *Journal of Cataract & Refractive Surgery* 39, 4 (2013), 501–510.
- [173] TAMADAZTE, B., AND ANDREFF, N. Weakly calibrated stereoscopic visual servoing for laser steering: Application to phonomicrosurgery. In *Intelligent Robots and Systems (IROS 2014), 2014 IEEE/RSJ International Conference on* (Sept 2014), pp. 743–748.
- [174] TAN, X., AND BARAS, J. S. Modeling and control of hysteresis in magnetostrictive actuators. *Automatica* 40, 9 (2004), 1469 – 1480.
- [175] TANZI, E. L., LUPTON, J. R., AND ALSTER, T. S. Lasers in dermatology: four decades of progress. *Journal of the American Academy of Dermatology* 49, 1 (2003), 1–34.
- [176] TENZER, P. E., AND MRAD, R. B. A systematic procedure for the design of piezoelectric inchworm precision positioners. *Mechatronics, IEEE/ASME Transactions on* 9, 2 (2004), 427–435.
- [177] TEXAS-VOICE-CENTER. <http://www.texasvoicecenter.com/>.
- [178] THORLABS. <http://www.thorlabs.de/>.
- [179] TROCCAZ, J. *Robotique médicale*. Collection Systèmes automatisés. Hermes Science Publications, 2012.
- [180] TSAI, L. *Robot Analysis: The Mechanics of Serial and Parallel Manipulators*. Wiley-Interscience publication. Wiley, 1999.
- [181] UNGER, M. A., CHOU, H.-P., THORSEN, T., SCHERER, A., AND QUAKE, S. R. Monolithic microfabricated valves and pumps by multilayer soft lithography. *Science* 288, 5463 (2000), 113–116.
- [182] VAN ABEL, K. M., MOORE, E. J., CARLSON, M. L., DAVIDSON, J. A., GARCIA, J. J., OLSEN, S. M., AND OLSEN, K. D. Transoral robotic surgery using the thulium: Yag laser: a prospective study. *Archives of Otolaryngology–Head & Neck Surgery* 138, 2 (2012), 158–166.
- [183] WEINBERGER, S., CHERIGUEN, Y., AND HOFFMANN, M. Static large-angle micromirror with aluminum nitride springs. In *Proceedings of the 23rd Micromechanics Europe Workshop, Ilmenau, Germany* (2012).



- [184] WEINER, A. *Ultrafast Optics*. Wiley Series in Pure and Applied Optics. Wiley, 2011.
- [185] WOOD, R., AVADHANULA, S., MENON, M., AND FEARING, R. Microrobotics using composite materials: the micromechanical flying insect thorax. In *IEEE International Conference on Robotics and Automation* (sept. 2003), vol. 2, pp. 1842–1849.
- [186] WOOD, R. J., AVADHANULA, S., SAHAI, R., STELTZ, E., AND FEARING, R. S. Micro-robot design using fiber reinforced composites. *Journal of Mechanical Design* 130, 5 (2008), 052304+.
- [187] WU CHAO, LIU XIN-JUN, WANG LIPING, AND WANG JINSONG. Optimal Design of Spherical 5R Parallel Manipulators Considering the Motion/Force Transmissibility. *Journal of Mechanical Design* 132, 3 (mar 2010), 031002–031002. 10.1115/1.4001129.
- [188] XIE, H., SUN, J., AND WU, L. Optical micro-endoscopes for 3D in-vivo imaging. *Spie Newsroom* (2010).
- [189] YAMAHATA, C. *Magnetically actuated micropumps*. PhD thesis, Lausanne, 2005.
- [190] YAN, Y., OLSZEWSKI, A. E., HOFFMAN, M. R., ZHUANG, P., FORD, C. N., DAILEY, S. H., AND JIANG, J. J. Use of lasers in laryngeal surgery. *Journal of Voice* 24, 1 (2010), 102–109.
- [191] YEO, S., CHOO, J., AND SIM, K. On the effects of ultrasonic vibrations on localized electrochemical deposition. *Journal of micromechanics and microengineering* 12, 3 (2002), 271.
- [192] YOU, Z. Folding structures out of flat materials. *Science* 345, 6197 (2014), 623–624.
- [193] ZHU, Y., LIU, W., JIA, K., LIAO, W., AND XIE, H. A piezoelectric unimorph actuator based tip-tilt-piston micromirror with high fill factor and small tilt and lateral shift. *Sensors and Actuators A-physical* 167 (2011), 495–501.
- [194] ZLATANOV, D., BENHABIB, B., AND FENTON, R. Analysis of the instantaneous kinematics and singular configurations of hybrid-chain manipulators. *Proceedings of the ASME 23rd Biennial Mechanisms Conference* 72 (1994), 467 – 476.
- [195] ZLATANOV, D., FENTON, R., AND BENHABIB, B. Identification and classification of the singular configurations of mechanisms. *Mechanism and Machine Theory* 33, 6 (1998), 743 – 760.
- [196] ZOPPI, M., ZLATANOV, D., AND MOLFINO, R. On the velocity analysis of interconnected chains mechanisms. *Mechanism and Machine Theory* 41, 11 (2006), 1346 – 1358.





## Résumé :

Cette thèse présente la conception, la fabrication et la commande d'un microrobot parallèle à deux degrés de liberté (rotations  $\theta_1$  et  $\theta_2$ ) qui est dédié pour la microchirurgie laser des cordes vocales. Ce travail a été développé dans le cadre du projet européen "Micro-Technologies and Systems for Robot-Assisted Laser Phonomicrosurgery" intitulé  $\mu$ RALP.

D'une part, les aspects médicaux et biologiques ont permis d'extraire un cahier des charges pour le microrobot. D'autre part, l'état de l'art a permis d'identifier et d'apporter une solution aux verrous technologiques pour satisfaire toutes les requêtes. Ce travail a proposé le développement de deux microrobots indépendants avec des structures parallèles. Bien qu'ayant le même objectif qui consiste à guider deux faisceaux lasers de manière précise vers les cordes vocales, chaque microrobot a une structure cinématique différente. Un miroir placé sur la plateforme de chacun des microrobots permet le guidage des faisceaux, en effectuant la réflexion et le changement de direction. La technique "Smart Composite Microstructures" a été utilisée pour microfabriquer les deux microrobots. En outre, les mouvements ont été réalisés grâce à l'utilisation d'actionneurs piézoélectriques. Enfin, la précision attendue par la chirurgie des cordes vocales a été atteinte en associant la commande par asservissement visuel et la pré-compensation des non linéarités et des oscillations mal amorties.

## Abstract:

This thesis reports the design, fabrication and control of a parallel microrobot with two degrees of freedom in rotation, that is destined to perform laser microsurgery on vocal folds. This work has been developed in the frame and in the context of the European project Micro-Technologies and Systems for Robot-Assisted Laser Phonomicrosurgery entitled  $\mu$ RALP.

On the one hand, needs and limits of medical aspects have been abstracted to create the microrobot specifications. On the other hand, the state-of-the-art has identified the technological stumbling blocks and has allowed to led to our proposition to satisfy the specifications. This work has envisaged the fabrication of two independent parallel microrobotic structures. Each proposed microrobot has a different kinematic structure, however they have the same objective that is to guide a laser beam onto the vocal folds. To this purpose, a mirror is placed on the end-effector of both microrobots in order to reflect and guide the laser beam. Smart Composite Microstructures fabrication technique was used to fabricate the two microrobots. Moreover, piezoelectric cantilever actuators have been used to generate the required rotations. Finally, the expected precision for laser microsurgery of the vocal folds was reached by coupling the feedforward compensation of nonlinearities and vibrations of the actuators with visual feedback control of the parallel kinematic mechanism.

The logo for SPIM (École doctorale SPIM) features the letters 'S', 'P', 'I', and 'M' in a large, white, sans-serif font. A horizontal yellow bar is positioned to the left of the 'S'.

■ École doctorale SPIM 16 route de Gray F - 25030 Besançon cedex

■ tél. +33 (0)3 81 66 66 02 ■ [ed-spim@univ-fcomte.fr](mailto:ed-spim@univ-fcomte.fr) ■ [www.ed-spim.univ-fcomte.fr](http://www.ed-spim.univ-fcomte.fr)

The logo for the University of Franche-Comté (UFC) features the letters 'U' and 'FC' in a large, bold, black font. A vertical yellow bar is positioned to the left of the 'U'. Below the letters, the text 'UNIVERSITÉ DE FRANCHE-COMTÉ' is written in a smaller, black, sans-serif font.

